

# Accelerated Magnetization Encoding for Reversibly Bound, Hyperpolarized Xenon in Molecular Host-Guest Systems

## **Dissertation**

zur Erlangung des Grades eines  
Doktors der Naturwissenschaft (Dr. rer. nat.)

am Fachbereich Physik  
der Freien Universität Berlin

vorgelegt von  
Hen-Amit Morik

Berlin 2022

Erstgutachter: Dr. Leif Schröder  
Zweitgutachter: Prof. Dr. Joachim Heberle  
Tag der Disputation: 8. Juli 2022

# Abstract

Measuring the magnetization of atomic nuclei as in magnetic resonance imaging (MRI) allows studying molecular systems under chemical exchange. The MRI signal of the water-soluble gas xenon provides a high specificity to its local molecular environment. To increase the sensitivity, hyperpolarization techniques can be applied and also a method called chemical exchange saturation transfer (CEST). Through CEST, molecular hosts that enclose Xe are detected and features of their Xe exchange are revealed. However, the CEST method is slow since multiple acquisitions along a spectral dimension are needed to characterize the exchange.

How to accelerate the CEST experiment is a main question of this work which was addressed by introducing a novel method called CAVKA (combined approach of variable flip angle, keyhole, and averaging). It divides the signal domain into two parts, performs time-consuming signal averaging only for the nearly constant part while rapidly updating the second part that encodes image contrast along the spectral dimension. The two are then computationally merged with consideration of the magnetization's physical properties for MRI scans. CAVKA encodes the magnetization-limited information from multiple samples as an image. Main benefit is a fast scan of host systems with relative fast exchange that otherwise causes signal loss.

After introducing CAVKA, its application to different host systems is described. The synthetic host cryptophane-A and biogenic gas vesicles were used as a proof of concept to study the method performance and adjust its parameters. Later on, cucurbit[ $n$ ]urils (CB6 and CB7) were extensively investigated with competitive guests to reveal differences in the host accessibility for Xe. It became clear that the observed CEST signal from commercially available CB7 samples is actually from CB6, an impurity from the synthesis of CB7. This impurity was also quantitatively estimated to be ca. 8.5%.

Finally, data denoising by principal component analysis (PCA) and wavelets was explored. Insights from their tailoring to MRI data of hyperpolarized Xe are reported. The two data domains of MRI (k-space and image space) were denoised and the performance was evaluated in terms of the SNR increase.

# Kurzzusammenfassung

Mit der Magnetresonanztomographie (MRT) lassen sich die Magnetisierung von Atomkernen messen und molekulare Systeme unter chemischem Austausch untersuchen. Das wasserlösliche Gas Xenon hat den Vorteil, dass sein MRT-Signal sehr empfindlich auf die lokale molekulare Umgebung reagiert. Zur Steigerung der Sensitivität können Techniken der Hyperpolarisation angewendet werden und auch das Verfahren CEST (chemical exchange saturation transfer). Mit CEST werden molekulare Wirte, die Xe einschließen, untersucht und die Merkmale ihres Xenon-Austauschs vermessen. Das reguläre CEST-Experiment ist jedoch langsam, da mehrere Aufnahmen entlang der spektralen Dimension notwendig sind, um den Austausch zu charakterisieren.

Eine Hauptfrage dieser Dissertation ist, wie man das CEST-Experiment beschleunigen kann. Hierzu wurde die neue Methode CAVKA (combined approach of variable flip angle, keyhole and averaging) entwickelt. Sie teilt die Signaldomäne in zwei Teile, führt eine zeitaufwendige Signalermittlung nur für den fast konstanten Teil durch, während der zweite Teil, der den Bildkontrast entlang der spektralen Dimension kodiert, schnell aktualisiert wird. Beide Teile werden unter Beachtung der physikalischen Eigenschaften der Magnetisierung bei der MRT anschließend wieder rechnergestützt zusammengefügt. CAVKA kodiert die Informationen mehrerer Proben als Bild. Der Hauptvorteil ist der schnelle Scan von Wirtssystemen mit relativ schnellem Austausch, der einen schnellen Signal-Abfall verursacht.

CAVKA wurde für verschiedenen Wirtssysteme eingesetzt. Der synthetische Wirt Cryptophan-A und biogene Gasvesikel wurden im Machbarkeitsnachweis verwendet. Später wurden Cucurbit[ $n$ ]urile (CB6 und CB7) mit kompetitiven Gästen untersucht, um Unterschiede in der Wirtszugänglichkeit für Xe aufzudecken. Es wurde deutlich, dass das beobachtete CEST-Signal von kommerziellen CB7-Proben tatsächlich vom CB6 stammt, und zwar als Verunreinigung, die ein Nebenprodukt bei der CB7-Synthese ist. Diese Verunreinigung wurde auf ca. 8,5% quantifiziert.

Schließlich wurden Xe MRT-Daten durch die Techniken Principal Component Analysis (PCA) und Wavelets entauscht. Die beiden Datendomänen der MRT (k-space und Bildraum) wurden untersucht und die SNR-Steigerung bewertet.

## Acknowledgments

I would like to thank Dr. Leif Schröder the head of the molecular imaging group at the FMP (Leibniz research institute for molecular pharmacology) in Berlin for his help, guidance and support throughout my PhD time.

I would also like to thank my colleagues at the molecular imaging group, our research was highly interdisciplinary and each provided help in his field of expertise.

Last but definitely not least, i would like to dedicate this work to Carsti.



# Contents

	Abstract . . . . .	i
	Kurzzusammenfassung . . . . .	ii
	Acknowledgments . . . . .	iii
	List of Figures . . . . .	v
	List of Tables . . . . .	vi
	List of Abbreviations . . . . .	vii
1	Background . . . . .	1
	1.1 Physics of MRI . . . . .	1
	1.2 MRI principles . . . . .	4
	1.3 Flip angle calibration for $^{129}\text{Xe}$ acquisitions . . . . .	6
	1.4 The $^{129}\text{Xe}$ polarizer . . . . .	10
	1.5 Chemical exchange saturation transfer . . . . .	12
	1.6 Objectives of this thesis . . . . .	15
2	Keyhole view sharing . . . . .	16
	2.1 The keyhole method . . . . .	17
	2.2 Results and Discussion . . . . .	18
	2.2.1 $^1\text{H}$ implementation . . . . .	19
	2.2.2 $^{129}\text{Xe}$ implementation . . . . .	25
3	CAVKA- Combined approach of VFA, keyhole and averaging . . . . .	31
	3.1 Components of the CAVKA method . . . . .	33
	3.1.1 VFA aspects . . . . .	33
	3.1.2 Averaging aspects . . . . .	34
	3.1.3 Substitution factor aspects . . . . .	35
	3.1.4 Assembling the required steps for CAVKA . . . . .	37

3.2	Acceleration and xenon saving provided by CAVKA . . . . .	39
3.2.1	Acceleration factor for HyperCEST . . . . .	39
3.2.2	Xenon deliveries saving . . . . .	40
3.2.3	Acceleration factor for other types of imaging series .	41
3.3	CAVKA simulations in digital phantom . . . . .	41
3.4	Results and discussion . . . . .	45
3.4.1	Experimental support to the analytically derived substitution factor . . . . .	45
3.4.2	Impact of keyhole size and number of averages on SNR	46
3.4.3	Acceleration in acquisition time by the CAVKA method	49
3.4.4	CAVKA simulations for identifying limitations . . . .	51
4	Imaging of hosts with fast Xe exchange . . . . .	62
4.1	Challenges of multivalent xenon hosts . . . . .	62
4.2	Results and discussion . . . . .	64
4.2.1	Signal averaging for the reference image . . . . .	64
4.2.2	Analysis of magnitude data averaging . . . . .	66
4.2.3	CAVKA imaging - Proof of principle . . . . .	68
5	Spectroscopy of host-guest system with competitive binding . . . . .	72
5.1	Introduction . . . . .	72
5.2	Results and discussion . . . . .	75
5.2.1	Synergistic benefits from the CAVKA acquisition . .	77
5.2.2	HyperCEST spectroscopy of accelerated exchange with competitive guest binding . . . . .	79
5.2.3	Further investigations regarding the hypothesis that the CB6 impurity in CB7 is the only source of the CEST response . . . . .	82
5.2.4	Labile exchange manifestation in the FID . . . . .	92
5.2.5	Chirality of the "blocker" . . . . .	95
5.3	CAVKA vs. UFZ . . . . .	95
5.3.1	Limits of echo summation . . . . .	98
5.3.2	Further segmentation considerations . . . . .	100

6	Denoising of hyperpolarized $^{129}\text{Xe}$ MR images . . . . .	102
6.1	Introduction . . . . .	102
6.2	Principal component analysis (PCA) . . . . .	103
6.3	The discrete Wavelet transform . . . . .	105
6.4	Results and discussion . . . . .	109
6.4.1	PCA denoising of k-space data . . . . .	111
6.4.2	Wavelet denoising of image space data . . . . .	116
	Bibliography . . . . .	123
	Declaration . . . . .	137
	Publications . . . . .	138

# List of Figures

1.1	90° pulse calibration for $^{129}\text{Xe}$ acquisitions I . . . . .	7
1.2	90° pulse calibration for $^{129}\text{Xe}$ acquisitions II . . . . .	8
1.3	90° pulse calibration for $^{129}\text{Xe}$ acquisitions III . . . . .	9
1.4	Chemical exchange saturation transfer (CEST) . . . . .	13
2.1	The keyhole domain . . . . .	17
2.2	CEST contrast in double phantom experiment . . . . .	19
2.3	Undersampling and SS reconstruction of $^1\text{H}$ images . . . . .	21
2.4	Error analysis of keyhole reconstructions . . . . .	22
2.5	Z-spectra from $^1\text{H}$ keyhole reconstructions . . . . .	24
2.6	Undersampling and WS reconstruction of $^{129}\text{Xe}$ images . . . . .	26
2.7	Z-spectra from $^{129}\text{Xe}$ keyhole reconstructions . . . . .	28
3.1	Optimizing the use of the magnetization by VFA excitation . . . . .	34
3.2	Averaging effect in MRI . . . . .	35
3.3	Importance of the substitution factor . . . . .	37
3.4	Illustration of the CAVKA method . . . . .	38
3.5	HyperCEST acceleration by CAVKA . . . . .	40
3.6	The digital phantom . . . . .	43
3.7	Noise properties under FT . . . . .	44
3.8	Experimental validation of the analytically derived substitution factor	46
3.9	Signal and SNR dependencies in the CAVKA method . . . . .	48
3.10	Z-spectra from $^{129}\text{Xe}$ CAVKA acquisition . . . . .	51
3.11	CAVKA reconstructions in digital phantom . . . . .	53
3.12	Error maps in digital phantom . . . . .	54
3.13	Z-spectra from CAVKA reconstructions in digital phantom . . . . .	55

3.14	CAVKA hybrid k-spaces . . . . .	56
3.15	Error analysis of CAVKA reconstructions in digital phantom . . . . .	59
4.1	Testing for the number of averages with a GVs sample . . . . .	65
4.2	Magnitude data averaging failure analysis . . . . .	67
4.3	CAVKA images of a GVs sample . . . . .	69
5.1	Chemical structures of hosts and guests . . . . .	73
5.2	CAVKA benefits in CB7 acquisitions . . . . .	78
5.3	Comparative HyperCEST z-spectra of CB7, <b>1</b> and cadaverine . . . . .	80
5.4	Tests with CB6, CB7 and <b>1</b> to identify the source of the of CEST response from CB7 samples . . . . .	84
5.5	Estimating the concentration of the CB6 impurity in a CB7 sample . . . . .	87
5.6	FID manifestation of the CB7 labile interaction . . . . .	93
5.7	FID manifestation of the labile interaction validates the presence of CB7 . . . . .	94
5.8	Testing the impact of the chirality of 1,4-bis(aminomethyl)cyclohexane on CEST suppression . . . . .	96
5.9	Host guest interactions revealed by CEST spectroscopy and related encoding techniques with acceleration through spatial parallelization . . . . .	97
5.10	Signal improvement by summation of echoes . . . . .	99
6.1	$\phi_{j,m}(x)$ - the scaling functions (wavelet decomposition) . . . . .	106
6.2	$\psi_{j,m}(x)$ - the Haar wavelet functions . . . . .	108
6.3	PCA denoising of an averaging series . . . . .	112
6.4	Optimal number of principal components . . . . .	114
6.5	Single level wavelet denoising . . . . .	118
6.6	Multilevel wavelet denoising . . . . .	122

# List of Tables

2.1	Weights value in keyhole WS reconstruction . . . . .	30
3.1	Parameters value used in BMC equations . . . . .	42
4.1	SNR comparison GVs and CrA . . . . .	70
5.1	Parameters extracted from Lorentzian curve fitting . . . . .	89
6.1	SNR comparison PCA . . . . .	116
6.2	SNR comparison wavelets . . . . .	119

## List of Abbreviations

<b>1</b>	<i>cis</i> -1,4-bis(aminomethyl)cyclohexane
<b>2</b>	cadaverine
<b>3</b>	putrescine
BMC	Bloch-McConnell
CAVKA	combined approach of VFA keyhole and averaging
CB5	cucurbit[5]uril
CB6	cucurbit[6]uril
CB7	cucurbit[7]uril
CB8	cucurbit[8]uril
CEST	chemical exchange saturation transfer
CFA	constant flip angle
CrA	cryptophane-A monoacid
DFT	discrete Fourier transform
DMSO	dimethyl sulfoxide
dPBS	Dulbecco's phosphate-buffered saline
FID	free induction decay
FLASH	fast low angle shot
FOV	field of view
FT	Fourier transform
GAG	glycosaminoglycans
GVs	gas vesicles
<sup>1</sup> H	hydrogen element
He	helium
HP	hyperpolarized
HyperCEST	CEST with hyperpolarized <sup>129</sup> Xe as the exchanging nuclei
iCB7	inverted CB7
MAE	mean absolute error
MR	magnetic resonance
MRI	magnetic resonance imaging
MT	magnetization transfer
NMR	nuclear magnetic resonance
pc	principal components
PCA	principal component analysis
PE	phase encoding
ppm	part per million
PV	ParaVision
RARE	rapid acquisition with relaxation enhancement
ROI	region of interest
Rb	rubidium
RF	radio frequency

SD	standard deviation
SEOP	spin exchange optical pumping
SNR	signal to noise ratio
SS	scaled substitution
SURE	Stein unbiased risk estimate
SVD	singular value decomposition
UFZ	ultra fast z-spectroscopy
VFA	variable flip angle
WS	weighted substitution
Xe	xenon
$^{129}\text{Xe}$	xenon isotope with a mass number of 129

# 1 Background

## 1.1 Physics of MRI

A description of the time evolution of a nucleus spin system, like the one measured in an MRI experiment, can be obtained using the laws of classical physics [1,2]. However, to correctly describe the energy pattern (like in Stern and Gerlach experiment [3]), a quantum mechanical description is needed. At first, this description is briefly given and the classical description will follow.

The experimental energy pattern from atomic nuclei in an external magnetic field is quantized and has levels according to

$$E = -m\gamma\hbar B_0, \quad m = -l, -l + 1, \dots, l - 1, l$$

where  $\gamma$  is the gyromagnetic ratio,  $\hbar$  is the Planck constant divided by  $2\pi$ ,  $B_0$  is the external magnetic field (assumed, without loss of generality, to be in the direction of the positive z-axis) and  $l$  is the spin quantum number.  $^{129}\text{Xe}$  and  $^1\text{H}$  have  $l = 1/2$ . Generally, however,  $l$  value depends on the number of protons and neutrons in the nucleus and on their pairing and it is not straight forward to calculate. The two possible energy levels when  $l = 1/2$  are  $E_{\downarrow} = 1/2\gamma\hbar B_0$  and  $E_{\uparrow} = -1/2\gamma\hbar B_0$  that correspond to spins in the "down" and "up" states, respectively.

For a large ensemble of individual spins  $\mu_i$  in a closed volume (a voxel) the net macroscopic magnetization vector  $\vec{M}$  is defined as  $\vec{M} = \sum_{i=1}^{N_s} \vec{\mu}_i$ , where  $N_s$  is the number of spins in the voxel. When an external magnetic field  $\vec{B}_0$  is applied, one can show that the time evolution of the net magnetization is according to the Bloch equations [1] (at the moment without relaxation terms)

$$\begin{aligned} \frac{d\vec{M}(t)}{dt} &= \vec{M}(t) \times \gamma\vec{B}_0, \\ \vec{M}_{(t=0)} &= \vec{M}_0. \end{aligned} \tag{1.1}$$

This is a classical description that would also fit to describe a tiny rotating magnet that experiences an external magnetic field. The solution of Eq. 1.1 is

$$\begin{aligned}
M_x(t) &= M_x(0) \cos(\omega_0 t) + M_y(0) \sin(\omega_0 t), \\
M_y(t) &= -M_x(0) \sin(\omega_0 t) + M_y(0) \cos(\omega_0 t), \\
M_z(t) &= M_z(0),
\end{aligned}
\tag{1.2}$$

where  $\omega_0 = \gamma |\vec{B}_0|$  is the Larmor frequency of rotation. Let  $M_{xy} = M_x + iM_y$  be defined as the transverse component of the magnetization, then the solution takes the form

$$\begin{aligned}
M_{xy}(t) &= M_{xy}(0) e^{-i\omega_0 t}, \\
M_z(t) &= M_z(0).
\end{aligned}
\tag{1.3}$$

This means that  $\vec{M}$  rotates with a constant velocity  $\omega_0$  around the z-axis (clockwise rotation) and has a constant component in the z direction; that is the time evolution of the magnetization vector.

In practice, only the transverse magnetization can be measured as inducible signal, the  $M_z$  component remains static and thus does not cause an inducible signal. The initial magnetization in equilibrium is only in the z direction, that is according to Eq. 1.3 when considering that the net macroscopic magnetization vector has transverse components ( $M_{xy}(0)$ ) in all directions that are averaged to zero. In the z direction, the net magnetization is non-zero since the external magnetic field in this direction makes one of the two energy levels more populated than the other, creating a net polarization.

Starting from equilibrium, the magnetization must be tilted from the z direction (or longitudinal direction) toward the direction of the xy plane (or the transverse plane). This is done by applying additional oscillating field  $\vec{B}_1$  in the form of a radio frequency (RF) pulse (called excitation pulse) in the direction of the x- or y-axis. If  $\vec{B}_1$  is applied in the x-axis direction oscillating at the Larmor frequency it tilts  $\vec{M}$  to the transverse plane by rotating it around the x-axis and the same holds for the y-axis. The tilting can be done in a controlled way called the flip angle  $\alpha$ .  $\vec{B}_1$  (or the excitation pulse) is applied for a short time and then is switched off, its duration is adjusted to provide the desired  $\alpha$  which depends also on the  $\vec{B}_1$  amplitude (see section

1.3). With the additional excitation pulse, the initial condition of the magnetization in Eq. 1.1 becomes  $M_{xy}(0) = M_0 \sin \alpha$ ,  $M_z(0) = M_0 \cos \alpha$  (where  $M_0$  is  $M_z(0)$  without an excitation pulse). After tilting the magnetization, it returns to its initial state in a process called relaxation.

Relaxation can be divided into two contributions: spin-spin interactions and spin-lattice interactions. Spin-spin interactions are the reason for the decay of transverse magnetization. The rotating spins go out of phase (their rotations become unsynchronized) which effectively decreases the measured signal. The spins go out of phase due to differences in their local chemical environments, which lead to small variations in the magnetic field they experience. The decay is generally considered to be exponential and its time constant is affected by different experimental conditions (for example the temperature). To model spin-spin interactions, the parameter  $T_2$  is used in an exponential decay term of the form

$$M_{xy}(t) = M_0 \sin \alpha \cdot e^{-t/T_2}.$$

Free spins in a fluid have a long  $T_2$ , whereas bound spins (for example in large molecules) have a shorter  $T_2$ .

Spin-lattice interactions are the reason for the regeneration of the longitudinal magnetization to its equilibrium level. The excitation pulse turns some of the initial longitudinal magnetization to transverse magnetization; it reduces the longitudinal magnetization from  $M_0$  to  $M_0 \cos \alpha$ . The RF pulse transfers energy to the medium that contains the spins (the "lattice"). Eventually, the deposited RF energy is released from the spins and increases the energy of the lattice and produces heat. As some of the spins go back to the lower energy state, the longitudinal magnetization recovers back to the thermal equilibrium level. The recovery rate, as in spin-spin interactions, is modeled by an exponential term with a parameter  $T_1$  and has the form

$$M_z(t) = (M_0 \cos \alpha - M_0)e^{-t/T_1} + M_0.$$

$T_1$  depends on the strength of  $\vec{B}_0$  and it is shorter when the tumbling rate of the molecular system is closer to the Larmor frequency (which is given by  $\gamma|\vec{B}_0|$ ) [4]. When hyperpolarization is performed (see section 1.4), the magnetization level exceeds the

thermal equilibrium value and the starting longitudinal magnetization cannot regenerate. Including the relaxation terms in Eq. 1.1 gives the full Bloch equations:

$$\begin{aligned}
\frac{dM_x(t)}{dt} &= \left( \vec{M}(t) \times \gamma \vec{B}_0 \right)_x - \frac{M_x(t)}{T_2}, \\
\frac{dM_y(t)}{dt} &= \left( \vec{M}(t) \times \gamma \vec{B}_0 \right)_y - \frac{M_y(t)}{T_2}, \\
\frac{dM_z(t)}{dt} &= \left( \vec{M}(t) \times \gamma \vec{B}_0 \right)_z + \frac{M_0 - M_z(t)}{T_1}, \\
\vec{M}_{(t=0)} &= \vec{M}_0.
\end{aligned} \tag{1.4}$$

The solution of Eq. 1.4 is

$$\begin{aligned}
M_{xy}(t) &= M_0 \sin \alpha \cdot e^{-i\omega_0 t} e^{-t/T_2} \\
M_z(t) &= M_0 + (M_0 \cos \alpha - M_0) e^{-t/T_1}.
\end{aligned} \tag{1.5}$$

The time evolution of the magnetization vector is rotation with a constant velocity  $\omega_0$  around the z-axis.

## 1.2 MRI principles

Magnetic resonance imaging is based on the spin property of the atomic nuclei. Most commonly, the nuclei of  $^1\text{H}$  are used for medical imaging, but other nuclei like  $^{19}\text{F}$ ,  $^{23}\text{Na}$ ,  $^{13}\text{C}$  and of course  $^{129}\text{Xe}$  can also be measured. In order to obtain an image, a spatially resolved signal is desired. This is achieved by applying a combination of magnetic field gradients and radio frequency (RF) pulses.

The following is true for the acquisition of a 2D image by Cartesian data sampling since only this type of MRI acquisition is used within this thesis. The spatial encoding comprises three steps:

- 1) Slice selection - This step confines the measurement to one slice with a given thickness perpendicular to the z-axis (or any arbitrary axis). First, a magnetic field gradient along the z-axis is applied (additionally to the static magnetic field). The gradient is linear with respect to the position:  $B_z(z) = G_z \cdot z$ , where  $G_z$  is constant (the amplitude of the magnetic field gradient). As a result, spins in different z lo-

cations start to rotate (precess) around the z-axis in different rotation rates. This behavior follows the Larmor equation ( $\omega = \gamma|\vec{B}|$ ) and the fact that a magnetic field gradient was applied ( $\vec{B} = B_0 + B_z$ ). Next, an RF pulse is applied with a specific frequency bandwidth that matches the Larmor condition for the locations within the desired slice. With that, a 2D slice perpendicular to the z-axis is selected to produce transverse magnetization.

2) Frequency encoding - This step uses a magnetic field gradient in one of the two transverse directions (let it be assumed as the x-axis direction) that is denoted  $G_x$  to make the rotation rates along this direction spatially dependent (similarly to the slice selection). This is done in order to be able to map rotation rates to spatial locations and to achieve spatial separation in the x direction.  $G_x$  stays on during the encoding of this sampling direction and inactive during signal acquisition. Upon completion of this step, one line of sampling points along the x direction is obtained.

3) Phase encoding - This step uses a magnetic field gradient  $G_y$  before each frequency encoding step (line of sampling points) to give the rotating spins in different y locations a phase (different starting positions of their rotations). This gradient is turned on and off before frequency encoding starts and will allow signal separation along this axis.

The steps of slice selection, frequency encoding and phase encoding make the spatial separation of the nuclear magnetic resonance signal possible. However, the sampled signal during the acquisition is superimposed and forms the so called k-space data.

The k-space data represent the MR image in the Fourier domain. Thus, only after applying the inverse Fourier transform to the k-space data the MR images are obtained (informally the direct Fourier transform can also be applied as it obtains the images). The k-space data is the collection of sampling points of the transverse magnetization in different spatial locations within the slice. However, the signal detector is not moving, the magnetization is manipulated during frequency and phase encoding to rotate differently along the x and y directions. This rotation is modeled into the transverse magnetization expression (Eq. 1.5) by adding the term  $e^{-i\gamma(G_x\Delta t_x \cdot x + G_y\Delta t_y \cdot y)}$ , where  $\Delta t_x$ ,  $\Delta t_y$  are the durations that the gradients are switched

on. Since the detected signal is the sum of all spins within the slice it has the form:

$$\iint_A M_0(x, y) e^{-i\omega_0 t} e^{-t/T_2} e^{-i\gamma(G_x \Delta t_x \cdot x + G_y \Delta t_y \cdot y)} dx dy, \quad (1.6)$$

where  $A$  is the area of the slice. The 2D Fourier transform of a function  $f(x, y)$  is

$$\iint_{-\infty}^{\infty} f(x, y) e^{-2\pi i(k_1 \cdot x + k_2 \cdot y)} dx dy. \quad (1.7)$$

It can be identified from Eq. 1.6 and 1.7 that the detected signal is the Fourier transform of the function  $M_0(x, y) e^{-i\omega_0 t} e^{-t/T_2}$  if one defines:

$$\begin{aligned} k_1 &= \frac{\gamma}{2\pi} G_x \Delta t_x, \\ k_2 &= \frac{\gamma}{2\pi} G_y \Delta t_y. \end{aligned} \quad (1.8)$$

These are the definitions of the k-space coordinates (or spatial frequencies) for the case where  $G_x$  and  $G_y$  have constant amplitudes in time (like when sampling in a Cartesian trajectory), otherwise the integral definitions should be used:  $k_1 = \frac{\gamma}{2\pi} \int_0^t G_x(\tau) d\tau$ ,  $k_2 = \frac{\gamma}{2\pi} \int_0^t G_y(\tau) d\tau$ . The shapes in time,  $G_x(t)$ ,  $G_y(t)$ , and the duration that these gradients are switched on determine the sampling trajectory in k-space. Additionally, Eq. 1.6 and 1.7 are equivalent only if the terms  $e^{-i\omega_0 t}$ ,  $e^{-t/T_2}$  are time independent. This is resolved by moving to the rotating frame of reference which makes the term  $e^{-i\omega_0 t}$  vanish. The signals are usually not acquired as simply decaying magnetization but as spin echoes or gradient echos of which the amplitude at the center of the echo is given by the echo time  $TE$ . Thus, by setting  $t = TE$  (TE is the effective echo time of one k-space line) we obtain  $e^{-TE/T_2}$  as a counter factor which assigns the same  $T_2$  relaxation for all sampled points within one line.

### 1.3 Flip angle calibration for $^{129}\text{Xe}$ acquisitions

In the following section the calibration of a  $90^\circ$  RF pulse with a block shape (constant amplitude) is described. This calibration enables the use of RF pulses with angles other than  $90^\circ$  and is especially important when the variable flip angle (VFA) scheme is used (see section 3.1.1). For  $^1\text{H}$  acquisitions, an automate procedure in ParaVision (PV) exists to calibrate the  $90^\circ$  block pulse. However, for  $^{129}\text{Xe}$  the procedure has to

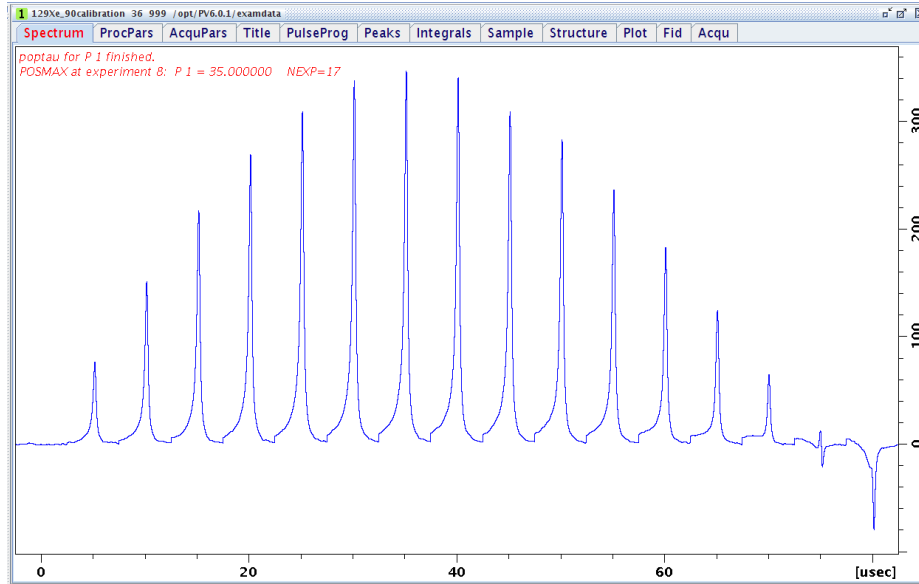


Figure 1.1: TopSpin automatic procedure to determine the duration of a block pulse that achieves a flip angle of  $90^\circ$ . The duration is taken from the maximal peak (of transverse magnetization) here with value of  $35.8 \mu\text{s}$ .

be done manually. In VFA acquisition, equal levels of transverse magnetization along the frequency encoding lines are desired and this creates the need for a precise flip angle calibration.

As a first step of the calibration procedure, a measurement in Topspin for the duration of a block pulse that achieves  $90^\circ$  is performed. The  $90^\circ$  flip angle is achieved as the pulse that yields maximum signal. The power of the block pulse is given as 32 W and the determined duration was  $35.8 \mu\text{s}$  (Fig. 1.1). This measurement should ideally provide all the necessary information for the calibration. However, additional tests (as will be explained in the next steps) show it needs to be further adjusted.

The Topspin result is entered in PV under the "Setup" tab in the "Reference power" field. In PV, the power should be entered for 1 ms block pulse. Since the pulse is rectangular, increasing its duration (from  $35.8 \mu\text{s}$  to 1 ms, a factor of 27.933) should be compensated by reducing its amplitude by the same factor in order to maintain the flip angle unchanged. The flip angle  $\alpha$  is given by  $\alpha = t_p \gamma |\vec{B}_1|$  where  $\gamma |\vec{B}_1|$  is proportional to  $\gamma \sqrt{P}$  when using the pulse power  $P$  in W and  $t_p$  as the pulse duration. The factor 27.933 for  $t_p$  thus needs to be compensated by  $27.933^2 = 780.252$ . Thus,

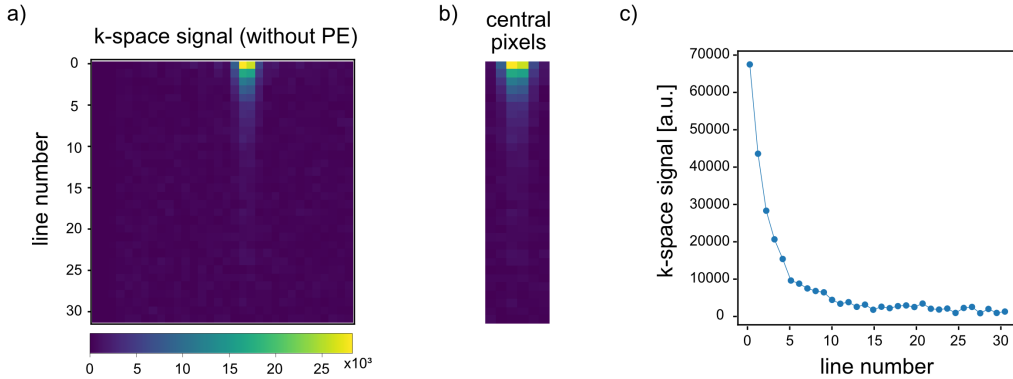


Figure 1.2: Processing of k-space data in order to plot the curve of k-space signal vs. the line number (transverse magnetization vs. the number of excitations). a) k-space data of the imaging acquisition without phase encoding and with constant flip angle of  $60^\circ$  (echoes are shifted to the right due to a delay of the digital filter which cannot be fully compensated in acquisitions with low number ( $\leq 32$ ) of frequency encoding steps because of the short sequence timing). b) Extraction of the six central pixel from each k-space line. c) Summation of the central pixels in each line (shown in b) and plotting this sum against the line number.

the amplitude is 41 mW. For the 1 ms reference pulse this is entered to the "Reference power" field.

Next, the reference power value is tested by acquiring an image using a modified FLASH (fast low angle shot) sequence that does not apply phase encoding and uses a constant flip angle (CFA) of  $60^\circ$ . This nominal flip angle is obtained by using the 1 ms reference pulse data. From the k-space data (Fig. 1.2a) the central six pixels in each line are extracted (Fig. 1.2b) and summed up, this sum is assigned to the signal value of each line i.e., the echo amplitude. Then, the graph of signal amplitude vs. line number is plotted (Fig. 1.2c).

The theoretical equation for the signal vs. line number curve is:

$$S(n) = M_0 \sin \alpha (\cos \alpha)^n, \quad n = 0, 1, \dots, N - 1, \quad (1.9)$$

where  $S(n)$  is signal intensity in the  $n$ -th line,  $M_0$  is the initial longitudinal magnetization,  $\alpha$  is the measured flip angle (with expected value of  $60^\circ$ ) and  $N$  is the total number of lines (the number of phase encoding steps). Eq. 1.9 follows Eq. 1.5 with the following assumptions: since  $^{129}\text{Xe}$  is hyperpolarized, the longitudinal magnetiza-

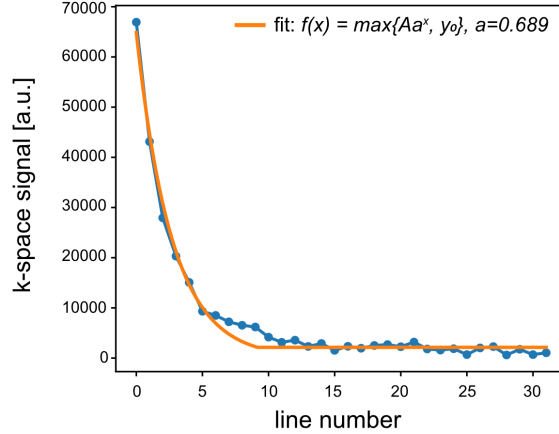


Figure 1.3: Determination of the measured flip angle by fitting of an exponential model with noise to the curve of the k-space signal against the line number. Fitting assigns the value of the exponent base  $a = 0.689$  from which the measured flip angle of  $46.45^\circ$  is calculated.

tion decays rather slowly and the regeneration term  $M_0 (1 - e^{-t/T_1})$  is obsolete. With  $TE/T_2 \ll 1$  ( $TE \sim 10$  ms,  $T_2 \sim 3$  s),  $TR/T_1 \ll 1$  ( $TR \sim 50$  ms,  $T_1 \sim 100$  s) the problem simplifies and the calculation is also done in the rotating frame of reference.

Fitting an exponential model with noise to this plot (Fig. 1.2c) of the form:

$$f(x) = \max\{A \cdot a^x, y_0\},$$

where  $y_0$  respects the noise level, and extracting the value of the exponent base  $a$  provides the measured flip angle,  $\alpha = \arccos(a)$ . The result was  $\alpha = 46.45^\circ$ , where Fig. 1.3 displays this fitting.

One can see that a smaller angle was actually determined than the one that had been selected as nominal value. Thus, this is compensated by increasing the value of the "Reference power" from 41 to 68 mW (a factor of  $(60/46.45)^2 = 1.668$ ). As a final step, the image acquisition and fitting routine are repeated to make sure  $\alpha = 60^\circ$  is measured. The monotonic decreasing trend of the transverse magnetization along the lines in Fig. 1.3 is achieved by adjusting the spoiling gradient after each acquisition for a sufficient duration. Otherwise deviations from this trend can occur as residual magnetization impacts the following signal.

## 1.4 The $^{129}\text{Xe}$ polarizer

Spin polarization determines the detectable magnetization and is defined using the amounts of spins in each of the energy states (see section 1.1). Denoting the number of spin in the up state as  $n_{\uparrow}$  and the number of spins in the down state as  $n_{\downarrow}$ , the polarization  $P$  is given by

$$P = \frac{n_{\uparrow} - n_{\downarrow}}{n_{\uparrow} + n_{\downarrow}}. \quad (1.10)$$

The polarization is temperature dependent and for a given temperature it is defined as the thermal equilibrium polarization level. Using the Boltzmann distribution for the two energy levels  $E_{\downarrow} = 1/2\gamma\hbar B_0$ ,  $E_{\uparrow} = -1/2\gamma\hbar B_0$  and substituting them in Eq. 1.10 provides a term for the thermal equilibrium polarization of  $^{129}\text{Xe}$ :

$$P_{\text{therm}} = \tanh\left(\frac{\hbar\gamma B_0}{2kT}\right), \quad (1.11)$$

where  $k$  is the Boltzmann constant and  $T$  is the temperature (in Kelvin). At room temperature,  $P_{\text{therm}}$  is less than 0.001%. The NMR signal is proportional to the polarization and thus it is quite low at room temperature. To increase it, one can consider changing one of the parameters in Eq. 1.11 within the known limitation for the range of temperatures and external magnetic field strengths for some applications (e.g., medical imaging). Another option is to increase the difference between the two spin populations (according to Eq. 1.10) outside the thermal equilibrium level. This is known as hyperpolarization.

In our lab  $^{129}\text{Xe}$  hyperpolarization is done by spin-exchange optical pumping (SEOP) [5]. To apply SEOP, a glass cell (the "optical cell") is used where an alkali metal is placed inside (rubidium). The optical cell is subjected to an external magnetic field by being placed inside a pair of Helmholtz coils and is illuminated by infrared laser light.

In the first step, optical pumping is executed. This includes shining a laser light with a wave length of 794.8 nm through Rb vapor enclosed within the optical cell to excite the  $D_1$  transition. The external B-field causes an electron spin flip in this transition according to the selection rules. Collisions cause both spin states to equilibrate and relax radiation free in the presence of  $\text{N}_2$  as quench gas. However, the

ongoing depolarization of one of the spin states in the ground level causes eventually an overpopulation of the other spin state. Rb is solid when the (optical) cell is cold at the beginning of the process and about 1 g of Rb is used. As the cell is heated up by an external heater and reaches 40°C, Rb melts and vapor start to form. Eventually the cell is heated up to 130°C. Other alkali metals can be used for optical pumping, but the advantage of Rb is its high vapor pressure that allows to keep the process at relative low temperatures.

In the second step, spin exchange takes place. The electron spin polarization is transferred through atomic interactions from Rb onto the nuclei of the Xe atoms. This step is dominated by the hyperfine interactions between the nucleus and the magnetic field that is generated by the Rb electron spin [6].

Xe flows into the optical cell as a gas mixture of N<sub>2</sub>, He and Xe. N<sub>2</sub> is used as a quenching gas to prevent the emission of radiation from relaxing atoms that would make the laser light polarization work less efficiently. Helium is used to adjust the pressure that affects the Rb absorption. Pressure adjustment by an excess of the other two gases is not optimal for the hyperpolarization process. The flow rate into the optical cell is 300 ml/min.

The gas mixture with hyperpolarized Xe, flows out of the optical cell in a rate of 100 ml/min unless stated otherwise (reduced rates are used sometimes to prevent foaming of the sample). It is led by a tubing all the way to phantom in the bore of the scanner. Delivery of hyperpolarized xenon into the solution within the phantom is done by capillaries that touch the liquid of the sample. This makes bubbles appear as the gas flows through and thus it is said that hyperpolarized Xe is bubbled into the solution. In CEST acquisitions, hyperpolarized Xe is redelivered to the sample before each of the saturation pulses. This is enabled by the continuous mode of operation of the polarizer. By using valves to open/close the gas flow, hyperpolarized Xe is bubbled into the sample at the beginning of each measurement, then the flow is stopped during the measurement (for the steps of magnetization manipulation and data recording) and this is repeated as many times as necessary. While the flow to the sample (or the flow out of the optical cell) is stopped, the flow in to the optical cell is redirected to an alternative path (a bypass of the optical cell). This is to prevent

a longer resident time of the gas mixture within the optical cell that would result with different degree of hyperpolarization which is of course undesired in a correctly functioned continuous mode.

## 1.5 Chemical exchange saturation transfer

Chemical exchange saturation transfer (CEST) involves more than one chemical environment (pool) for the atomic nuclei that provide the MR signal. For example,  $^1\text{H}$  within molecules of  $\text{H}_2\text{O}$  (one pool) and within (the hydroxyl groups of) molecules of glycogen (second pool), or  $^{129}\text{Xe}$  in an aqueous solution (free Xe pool) and inside a molecular host (caged Xe pool). The nuclei go through an exchange between the two chemical environments, where in each environment the Larmor frequency differs. This allows to selectively saturate (destroy) the magnetization of the nuclei in one pool by using an RF pulse with a specific frequency that matches the resonance frequency of the pool. This is illustrated by the first step (arrow) in Fig. 1.4a. Next, saturated nuclei leave the host and enter back into the free Xe pool where a decrease in the magnetization of this pool can then be detected. This is illustrated by the second step in Fig. 1.4a. When the nuclei involved in the exchange are hyperpolarized  $^{129}\text{Xe}$ , the method is named HyperCEST [7].

The reduced magnetization that occurs in the presence of the host molecule is the basis for the host detection through CEST. This reduction in magnetization levels also provides a contrast mechanism between compartments that include/exclude the host molecule. One of the advantages of CEST is an amplified sensitivity. Whereas the direct NMR detection of  $^{129}\text{Xe}$  inside a host molecule is not feasible, for sub micro molar concentrations, the detection using CEST is easily possible. The amplified sensitivity is due to the fact that during the saturation time, hundreds to thousands (depending on the host's exchange rate and on the saturation time) of exchanging Xe atoms are depolarized and the accumulated effect is measurable.

The typical graph from a CEST experiment is a z-spectrum which is shown in Fig. 1.4b. Along the x-axis is the frequency of the saturation pulses and along the y-axis is the normalized detected signal. At most frequencies, the signal level is unchanged, however in two frequencies ranges a decrease in the magnetization appears. At the

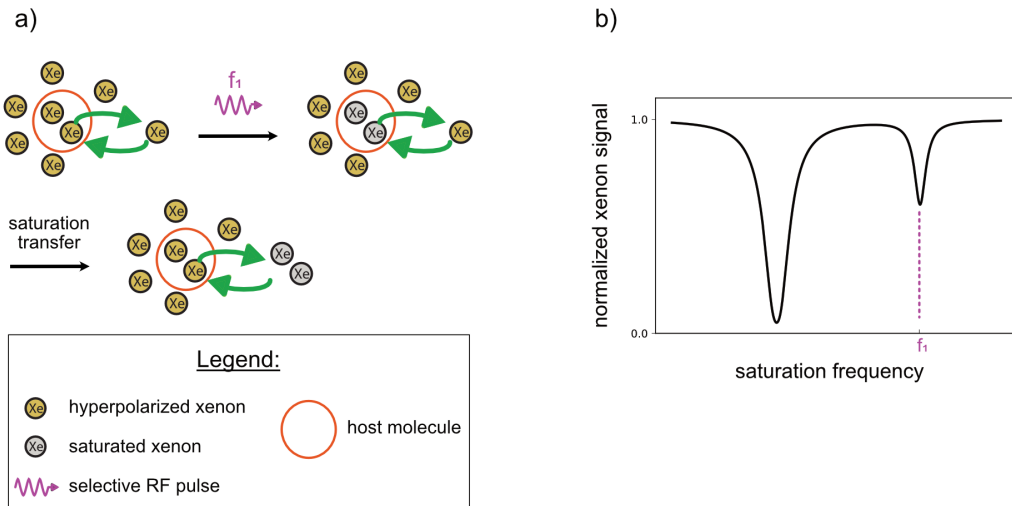


Figure 1.4: Chemical exchange saturation transfer (CEST) phenomenon and measurable output (z-spectrum). a) The two-step CEST mechanism of selective saturation of one pool ( $^{129}\text{Xe}@host$ ) and transfer of the saturation to the second pool ( $^{129}\text{Xe}@solution$ ). b) A z-spectrum plot which shows the magnetization level (of the  $^{129}\text{Xe}@solution$  pool) against the saturation frequency. Sensing the host molecule is enabled by the appearance of the peak at the saturation frequency  $f_1$ .

frequency to the left (often referred to as the water frequency for  $^1\text{H}$  and the solution pool frequency for  $^{129}\text{Xe}$ ), a full saturation appears, and corresponds to direct saturation of the detected magnetization (direct in the sense that no exchange and saturation transfer are involved). At the frequency  $f_1$  (often referred to as CEST pool or  $^{129}\text{Xe}@host$ ) a partial saturation appears, and corresponds to the CEST phenomenon. The CEST saturation is usually incomplete since only nuclei that have been inside the host during the saturation time are depolarized. CEST is an indirect method as the saturation is done for nuclei inside the host but the detection is from the nuclei when they are in the free Xe pool. Quantification of the CEST effect is typically done by the difference between the signals at the CEST position ( $f_1$  frequency at Fig. 1.4b) and at a position without magnetization decrease (off-resonance position). The distance between the two peaks in the z-spectrum is known as the chemical shift of the CEST pool.  $^{129}\text{Xe}$  has a relative large chemical shift range (host dependent) which serves as an advantage of the HyperCEST method. When the chemical shift is small, overlapping of the two peaks can interfere with a clear host

detection.

Mathematical modeling of the magnetization under chemical exchange was suggested by McConnell [8] as a modified version of the Bloch equations and therefore they are known as the Bloch-McConnell (BMC) equations. BMC equations describe, as the Bloch equations, the time evolution of the 3D magnetization. However, they describe two magnetization pools instead of just one, with an ongoing spins exchange between the two pools. Accordingly, two exchange rate constants (from one pool into the second and vice versa) were introduced to the Bloch equations by McConnell. The BMC equations are:

$$\begin{aligned}
\frac{dM_x^A}{dt} &= -\Delta\omega_A M_y^A - \frac{M_x^A}{T_2^A} - k_{AB}M_x^A + k_{BA}M_x^B, \\
\frac{dM_y^A}{dt} &= \Delta\omega_A M_x^A - \frac{M_y^A}{T_2^A} - \omega_1 M_z^A - k_{AB}M_y^A + k_{BA}M_y^B, \\
\frac{dM_z^A}{dt} &= \frac{M_0^A - M_z^A}{T_1^A} + \omega_1 M_y^A - k_{AB}M_z^A + k_{BA}M_z^B, \\
\\
\frac{dM_x^B}{dt} &= -\Delta\omega_B M_y^B - \frac{M_x^B}{T_2^B} + k_{AB}M_x^A - k_{BA}M_x^B, \\
\frac{dM_y^B}{dt} &= \Delta\omega_B M_x^B - \frac{M_y^B}{T_2^B} - \omega_1 M_z^B + k_{AB}M_y^A - k_{BA}M_y^B, \\
\frac{dM_z^B}{dt} &= \frac{M_0^B - M_z^B}{T_1^B} + \omega_1 M_y^B + k_{AB}M_z^A - k_{BA}M_z^B, \\
\\
\vec{M}_{(t=0)}^A &= \vec{M}_0^A, \\
\vec{M}_{(t=0)}^B &= \vec{M}_0^B.
\end{aligned} \tag{1.12}$$

A, B denote the free and caged  $^{129}\text{Xe}$  pools (or the abundant and diluted pools in the case of  $^1\text{H}$ ), respectively.  $k_{AB}$  denotes the exchange rate constant (of spins) from pool A to pool B and  $k_{BA}$  from pool B to pool A. The saturation pulse is applied along the x-axis with amplitude  $B_{\text{sat}}$  ( $\omega_1 = \gamma B_{\text{sat}}$ ) and frequency offset  $\omega_{\text{sat}}$ .  $\Delta\omega_{A,B} = \omega_{\text{sat}} - \omega_{A,B}$  is the difference between the saturation pulse frequency and the Larmor frequency of pools A and B.

Solution of Eq. 1.12 can be done numerically [9–11]. An analytical solution under

certain assumptions was also suggested [12]. These solutions allow to extract additional information from the z-spectrum (additional to the sensing of the host molecule), in the form of the exchange rate constants and other exchange kinetics parameters (e.g., fraction of the occupied host molecule). Curve fitting of the BMC solutions (analytical or numerical) to the experimental z-spectra enables the extraction of the above mentioned parameters. However, to obtain unambiguous results for all parameters multiple z-spectra are required, e.g., with different saturation powers [13].

## 1.6 Objectives of this thesis

The acquisition of CEST data is done stepwise along the  $\omega_{\text{sat}}$  dimension and is therefore time consuming. Moreover, imaging is a spatially resolved technique that deploys the available magnetization upon several locations within the field of view. Thus, it often faces the challenge of low SNR despite hyperpolarization and requires additional averaging which prolongs the CEST acquisition even more. Broader application of HyperCEST adds another dimension of challenges that relate to the molecular aspects. Hosts that exchange Xe in a high rate or have other types of labile interactions with xenon quickly dephase the spin ensemble and also decrease the SNR. Facing these challenges then requires improved acquisition strategies that would allow to capture high quality images and z-spectra while keeping the acquisition times reasonable and practical. Accordingly, these are the thesis main objectives:

- Development of a method that allows fast spatial and spectral encoding in MRI of spin-hyperpolarized  $^{129}\text{Xe}$  that goes through a reversible exchange with a host molecule (HyperCEST MRI).
- Tests and applications of the developed method in systems that suffer from fast decay of the magnetization due to enhanced spin-spin interactions (short  $T_2$  systems).
- Applying computational methods to the  $^{129}\text{Xe}$  MRI signal with the goal of improving the SNR.

## 2 Keyhole view sharing

The keyhole concept is an undersampling (or view sharing) approach [14, 15]. Such approaches [16–21] have demonstrated reliable extraction of information from a fewer number of sampled data points. Thus, they provide under certain circumstances an acceleration in the acquisition time and support an optimization to the use of the hyperpolarization. The latter is achieved by spreading the entire available magnetization upon a fewer number of sampling points.

Applying undersampling methods is usually accompanied by error analysis that provides an evaluation for the impact of omitting some of the data on the extracted parameters, graphs and images. Error metrics comprise absolute and relative error and they might need to be chosen wisely, in case they differ. Moreover, if the extracted graphs are based on averaged values (like from ROIs), the error term for these averaged values doesn't always coincide with the error terms of the individual instances used for averaging. However, the latter does not reduce the reliability of averaged values, if these are the ones with experimental importance.

Reliability tests therefore accompany the implementation of undersampling methods and check for capturing the desired features of the data under the chosen undersampling strategy. In MRI, contrast is one of the important features of the data [22–24] and its preservation while applying undersampling is desired. Contrast capturing in sub-sampled MRI can be challenging since contrast is a feature of the image domain whereas sub-sampling is done in the Fourier domain (k-space). Rules of thumbs acknowledge some connections between the Fourier and the image domains. For example, low modes (of the Fourier domain) affect the coarse structure or overall shape of the image and high modes affect the fine details and edges in the image [25]. While these rules of thumb provide some kind of general frame to design sub-sampling trajectories, it is still hard to predict *a priori* how a given k-space trajectory would affect the resulted image and its features. Individual tests for MR images are needed.

The keyhole approach concentrate on data sampling in the center of k-space (which corresponds to the low modes of the two spatial directions of the Fourier domain).

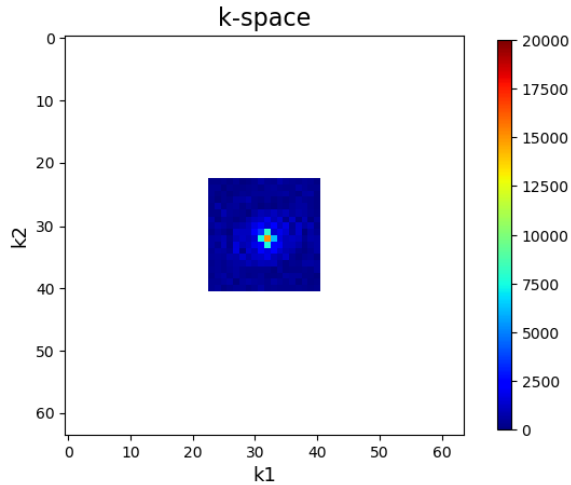


Figure 2.1: The keyhole domain. Experimental k-space data of size  $64 \times 64$  pixels was cropped for this illustration

In the following chapter, the keyhole approach is discussed for  $^1\text{H}$  and  $^{129}\text{Xe}$  MR images. For each type of MRI, two methods of data completion, namely scaled substitution and weighted substitution, were tested for three undersampling factors and along dynamic contrast imaging series. The visual quality of the images was inspected, an error analysis was performed and the z-spectra derived from the keyhole reconstructed images were compared to the spectra derived from the fully-sampled images. Finally, as part of discussing the results, the drawbacks of this approach when it comes to xenon application with more noisy data are described and provide a natural motivation to the later presented CAVKA method.

## 2.1 The keyhole method

This type of implementation to accelerate MRI acquisitions was first described by Hu and Parrish [15]. It involves the acquisition of a fully sampled reference image and a series of subsampled images where only a square in the center of k-space (referred to as "keyhole") is acquired. Missing data in the periphery of k-space is retrieved by computations on the reference image. Following subsequent studies [14], two types of computations are explored to generate the hybrid k-space:

1. Scaled substitution (SS).

2. Weighted substitution (WS).

In SS, reconstruction of a full resolution (complex-valued) 2D k-space  $S(k_1, k_2)$  is done according to:

$$S(k_1, k_2) = \begin{cases} S_{\text{key}}, & \forall(k_1, k_2) \in \text{keyhole} \\ \beta S_{\text{ref}}, & \forall(k_1, k_2) \in \text{periphery} \end{cases}. \quad (2.1)$$

$S_{\text{key}}$  denotes the k-space of the keyhole image,  $S_{\text{ref}}$  denotes the k-space data of an unsaturated reference image,  $k_1$  and  $k_2$  are the two k-space coordinates and  $\beta$  is the substitution factor defined as

$$\beta = \max\{|S_{\text{key}}|\} / \max\{|S_{\text{ref}}|\}.$$

In WS, reconstruction is achieved according to:

$$S(k_1, k_2) = \begin{cases} S_{\text{key}}, & \forall(k_1, k_2) \in \text{keyhole} \\ w_1 S_{\text{ref}} + w_2 S_{\text{saturated ref}}, & \forall(k_1, k_2) \in \text{periphery} \end{cases}. \quad (2.2)$$

Here, k-space data of two reference images is needed: unsaturated and saturated (at 0 Hz saturation offset).  $w_1$  and  $w_2$  are weights (scalars) used to complete missing data in the periphery and they are obtained by an optimization procedure (squared error minimization) on the keyhole data:

$$w_1, w_2 = \arg \min_{w_1, w_2} \| |S| - (w_1 |S_{\text{ref}}| + w_2 |S_{\text{saturated ref}}|) \|_2^2,$$

where  $\|\cdot\|_2$  is the "l<sup>2</sup>- norm".

## 2.2 Results and Discussion

The keyhole approach was first implemented for <sup>1</sup>H and then for <sup>129</sup>Xe as demonstrated in the next sections.

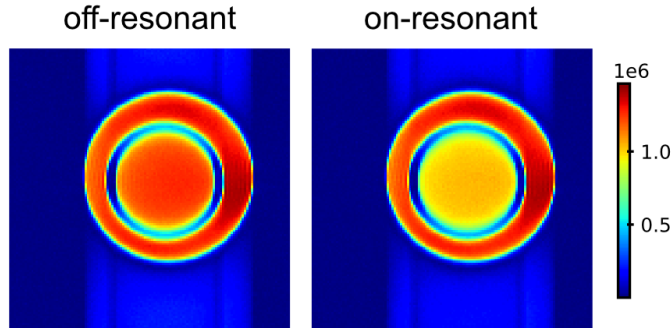


Figure 2.2: CEST contrast in double phantom experiment. Left: Applying saturation pulse off-resonant results with full magnetization. Right: Applying saturation pulse on-resonant with the frequency of  $^1\text{H}$ @heparin results with a decreased magnetization in the inner compartment. Images are fully sampled (size of  $128 \times 128$ ).

### 2.2.1 $^1\text{H}$ implementation

Experiments were done in "double phantom": two NMR tubes of 5 and 10 mm that are placed one inside the other. They form two separated compartments where two different solutions are loaded. In this section a sample of heparin with concentration of 250,000 EIU was loaded in the inner compartment and water in the outer compartment. Heparin belongs to the glycosaminoglycans (GAGs) family and can be used as a CEST agent due to the exchanging protons at its hydroxyl groups. Scans were done using a modified RARE sequence with a CEST preparation block. Matrix size was  $128 \times 128$ . Saturation pulses of 5 s and  $0.5 \mu\text{T}$  were applied with frequencies of  $-1.87 \text{ ppm}$  ( $-750 \text{ Hz}$ ) for the off-resonant case and  $0.96 \text{ ppm}$  ( $384.2 \text{ Hz}$ ) for the on-resonant case.  $TE$  and  $TR$  were 7 ms and 15 s, respectively. The RARE factor was 128. The repetition time here is the encoding time of one full image (unlike in the FLASH sequence that will be used later and for the most part of this dissertation) and its duration was set to be long enough to allow full recovery of the longitudinal magnetization between sequential images.

To implement the keyhole method, fully sampled k-spaces were acquired and then the keyhole domain was cut out of them. For the  $^1\text{H}$  MRI implementation, undersampling was done only along the phase encoding direction since the motivation for using the keyhole method was an acceleration of the acquisition-time. The phase encoding

step is the slower step (relative to frequency encoding) and by reducing the number of encoding steps a more meaningful acceleration could be achieved. The keyholes had sizes of  $128 \times 32$ ,  $128 \times 16$ , and  $128 \times 8$  which correspond to undersampling factors of  $R = 4$ , 8, and 16. The effect of undersampling on image reconstruction is shown in Fig. 2.3.

When only using the keyhole without the periphery, information on edges gets lost and this leads to a reduced sharpness of the image. This comes with a relative minor decrease in the visual quality for  $R = 4$ . Whereas for  $R = 8$  one can still recognize each of the phantom compartments and the difference between their signal intensities (contrast), for  $R = 16$  that is no longer the case. In SS reconstructions, the keyhole domain of each offset (on- and off- resonant) was then placed in the center of a reference scan (with off-resonant saturation), followed by scaling of the periphery of the reference scan according to Eq. 2.1. The results of this data composition are also shown in Fig. 2.3. The method yields full resolution images ( $128 \times 128$ ) without the artefacts associated with undersampling. Importantly, the contrast between the compartments in the on-resonant offset was preserved, although only the keyhole domain contained this information and was integrated into a reference data that had no such information. The preservation of image contrast using SS for the hybrid data is in line with the known aspects of the Fourier transform: low frequency information (located in the center of k-space) determines the coarse features of the image while high frequency information (located in the periphery of k-space) determines the fine details. [25]

In WS reconstructions, keyholes from the two offsets (off-resonant and on  $^1\text{H}$ @heparin resonant frequency) were represented as a linear combination of the keyhole data of two images: an off-resonant and a data set with on resonance saturation on water (at 0 Hz), following Eq. 2.2. The weights in this representation were obtained by using the function "curve fit" of the "optimization" module of the package "scipy" in Python 3.8. The same pulse sequence and acquisition parameters were used as for SS reconstructions. WS reconstructions showed equal visual quality as SS reconstructions for the three undersampling factors ( $R = 4, 8, 16$ ) and a quantified comparison of the two methods will follow next.

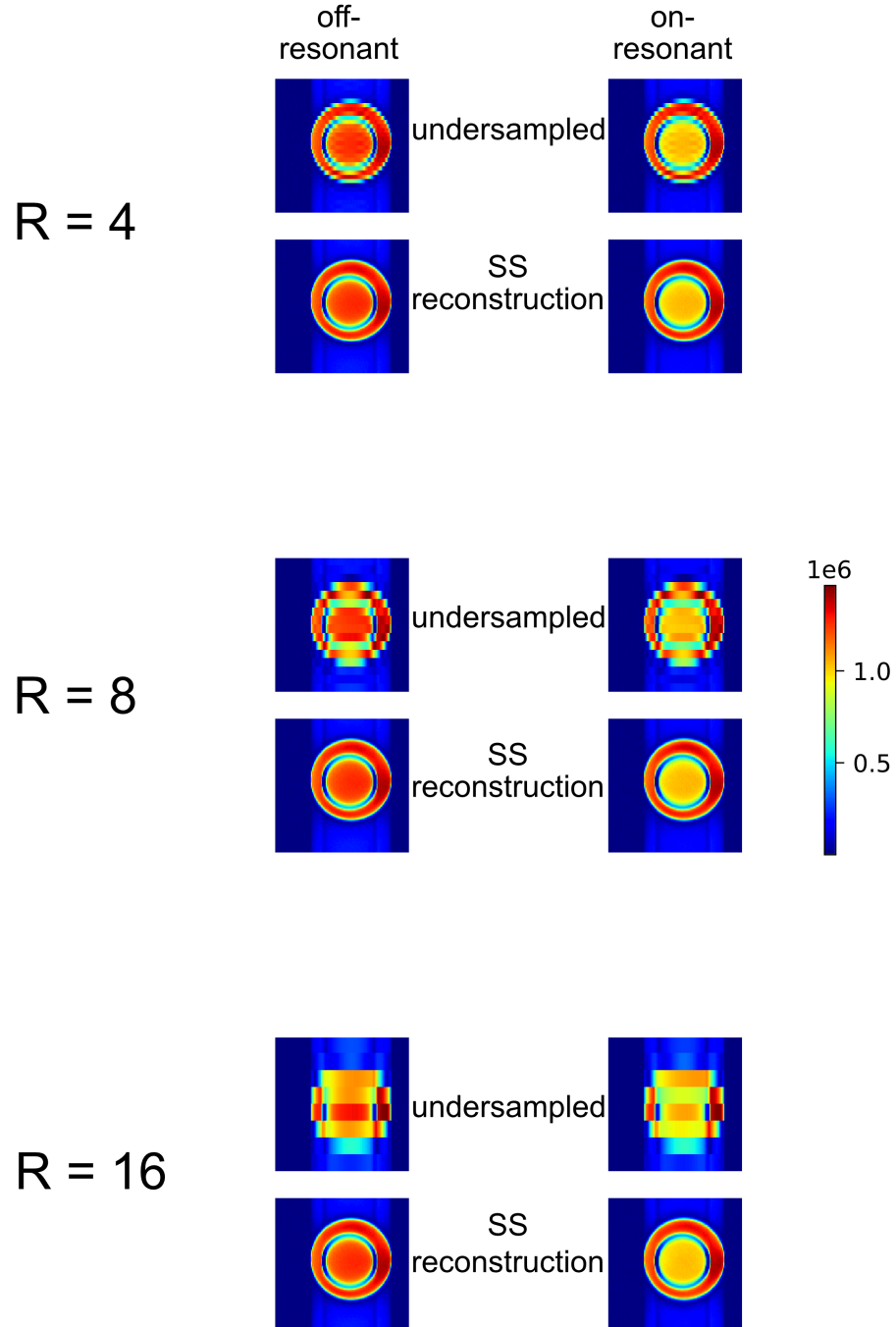


Figure 2.3: Undersampling and SS reconstruction of  $^1\text{H}$  images. Undersampled images lose their sharpness as the undersampling factor increases (top to bottom  $R = 4, 8, 16$ ). SS reconstruction retrieves the sharpness and preserves the on-resonant contrast (right column) between the phantom compartments.

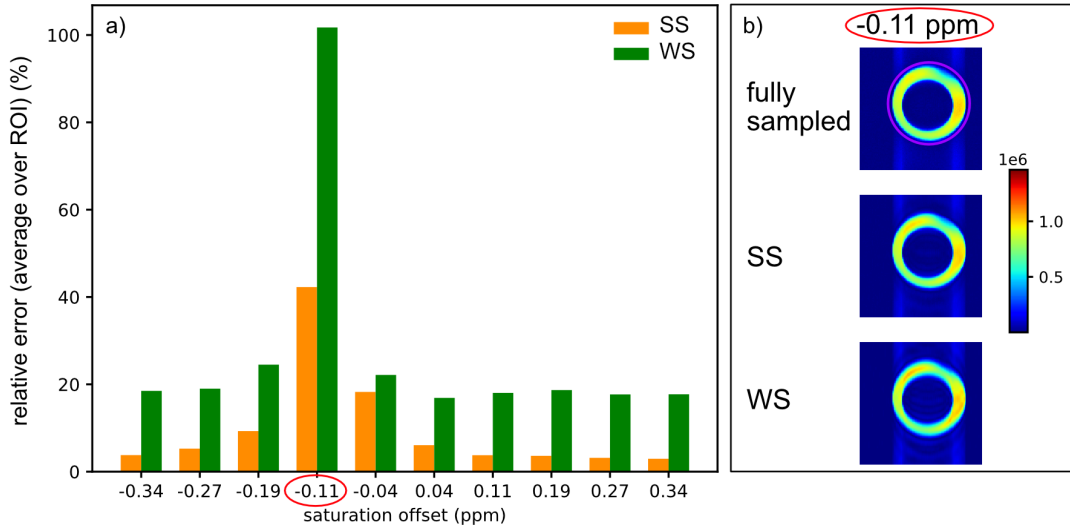


Figure 2.4: Error analysis of keyhole reconstructions. a) Relative error of SS/WS from fully sampling. SS error (orange) is lower than WS error (green) at each offset and they both peak at  $-0.11$  ppm. b) Image comparison: fully-sampled, SS and WS at the offset  $-0.11$  ppm reveals that the high error occurs at the offset with a strong contrast between the compartments. Purple circle at the top image shows the ROI used for the relative error average.

For comparing SS and WS reconstructions a full imaging series was acquired comprised of 50 offsets between  $-1.87-1.87$  ppm ( $-750-750$  Hz) in  $0.0765$  ppm ( $30.6$  Hz) steps with the same acquisition parameters as before. Undersampling factor  $R = 8$  was chosen for this comparison according to a visual inspection of the reconstruction quality for all images in the series, which showed that  $R = 16$  might include too severe artefacts relative to fully sampling for some of the offsets. In each SS/WS image the relative error (percentage deviation) from the fully-sampled image at the same offset was calculated pixel-wise. Next, a ROI was defined around the double phantom and the average value of the relative errors (without considering their signs) from all the pixels inside the ROI was calculated.

Fig. 2.4a shows these errors as a function of the offset. It focus on the ten central offsets after observing that the error outside this frequencies range stays constant at levels of 3% and 18% for SS and WS, respectively. For all offsets in Fig. 2.4, WS shows higher error levels than SS. The highest error for both SS and WS occurs at

-0.11 ppm. In order to explain the cause of the high error in this offset, the images from each reconstruction method and the fully-sampled one are shown in Fig. 2.4b.

This figure reveals that this offset has a very strong contrast between the compartments which is characterized by complete saturation of the inner compartment and depletion of more than half of the full magnetization in the outer one. This draws a clear limitation on the accuracy of the keyhole reconstructions for this kind of strong image contrast. However, for the rest of the offsets without such a strong contrast (all but -0.11 and -0.19 ppm), including the  $^1\text{H@heparin}$  resonance frequency (0.96 ppm), the errors level are much lower and especially for SS are quite reasonable.

An alternative explanation for the high error between SS/WS and fully-sampled at -0.11 ppm was suggested: the error is high for this offset since the complete saturation in the inner compartment creates close-to-zero values such when a relative error is calculated for them, it yields high errors. This argument in fact suggests that it is not the geometry of the imaged object that affects the error levels rather the metric of the error calculation. However changing the error metric to be absolute (i.e., pixel-wise subtraction) indeed dismissed this argument by showing that an offset with a strong contrast also had the highest absolute error.

At -0.04 ppm the second largest error for SS appears. This offset is the closest to complete saturation (null signal) in this imaging series. The source of the error in this offset is the use of an off-resonant (full magnetization) reference image to reconstruct an image with complete saturation. As will be discussed later (in section 3.4.4), reconstructing strong contrast in a hybrid image, where the keyhole holds this kind of contrast information but the reference image has no contrast at all, leads to high errors.

Another important aspect of comparing SS and WS reconstructions is with regards to their imaging-based z-spectra. These spectra are created by taking the averaged signal value over a defined ROI in the image at each offset and plotting this signal intensity against the frequency offset. The same imaging series that was used in the previous section (error analysis of WS/SS) was also used here. However, for the plotting of the z-spectra the full range of frequencies (50 offsets) was used.

Spectra were plotted from SS, WS and fully-sampled images for  $R = 4, 8, 16$

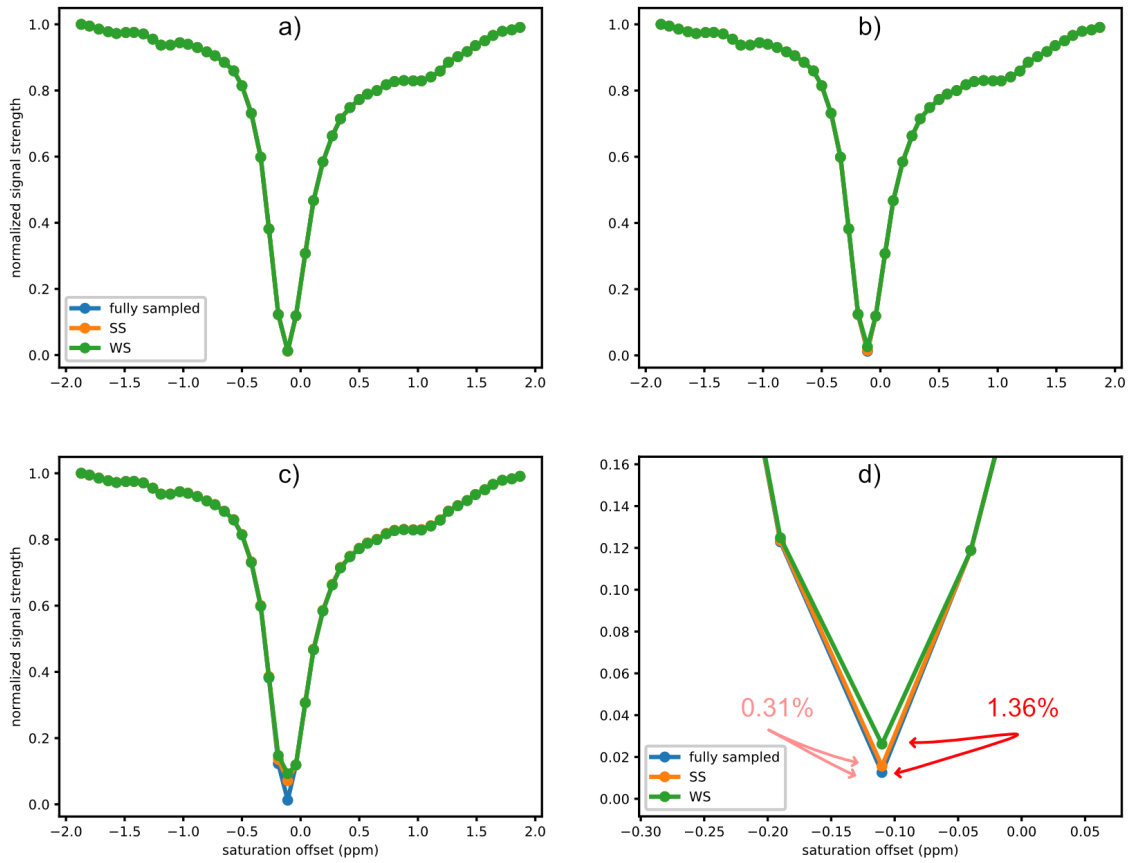


Figure 2.5: Z-spectra from keyhole reconstructions with different undersampling factors of: a)  $R = 4$ , b)  $R = 8$  and c)  $R = 16$ . d) Zoom in on b, shows the signal deviations between SS/WS (orange/green) and fully sampled (blue) at  $-0.11$  ppm. A good agreement between the spectra is observed.

and appear in Fig. 2.5. For  $R = 4$  (Fig. 2.5a) the three spectra display complete overlap, for  $R = 8$  (Fig. 2.5b) a deviation appears at one offset of  $-0.11$  ppm and for  $R = 16$  (Fig. 2.5c) deviations appear at two offsets of  $-0.11$  and  $-0.19$  ppm, with a larger deviation at  $-0.11$  ppm than with  $R = 8$ . For all undersampling factors, the important (qualitative) information of the spectrum is retained: the direct water saturation (at 0 ppm) and the CEST saturation (at 0.96 ppm), appeared to be in a good agreement with fully sampling. However, quantitatively at  $-0.11$  ppm and  $R = 8$  there are errors of 0.31% and 1.36% for SS and WS, respectively. This is shown in Fig. 2.5d. Importantly, here one can see that although high (pixel-wise) averaged error values for SS/WS were seen (Fig. 2.4), the error between the signal averages of SS/WS and the signal average of fully sampled is actually much lower. This is due to calculating the averaged errors with absolute values. However, by calculating the signal averages first and then the error between them, positive and negative error contributions cancel out each other and the error between the signal averages turns out lower. This means that even if the keyhole-reconstructed imaging series shows serious visual deviations from the conventional (fully-sampled) imaging series (this is the case for  $R = 16$ ), the two z-spectra are still in good agreement under these experimental conditions.

### 2.2.2 $^{129}\text{Xe}$ implementation

Experiments were done in a double phantom with  $\text{H}_2\text{O}$  in the outer compartment and CrA ( $10 \mu\text{M}$  in  $\text{H}_2\text{O}$  + 0.2% DMSO) in the inner compartment. Xenon imaging is limited in resolution relative to proton imaging mainly because of the lower spin density and available magnetization. Typically, in our setup, the  $^{129}\text{Xe}$  isotope concentration in water is  $\sim 260 \mu\text{M}$  while  $^1\text{H}$  concentration in water is 110 M ( $4.3 \times 10^5$ -fold higher). This enables typical resolution of  $32 \times 32$  in  $^{129}\text{Xe}$  images which in turn also limits the undersampling factors. Fig. 2.6 shows undersampled images with resolutions  $32 \times 16$ ,  $32 \times 8$  and  $32 \times 4$  that corresponds to undersampling factors  $R = 2, 4$  and 8 along the phase encoding direction. Setting the resolution to be under 16 (in phase encoding or frequency direction) is restricted at the Bruker scanner. To achieve lower resolutions, the "interpolation" option (within the "resolution" tab) was used. It is originally

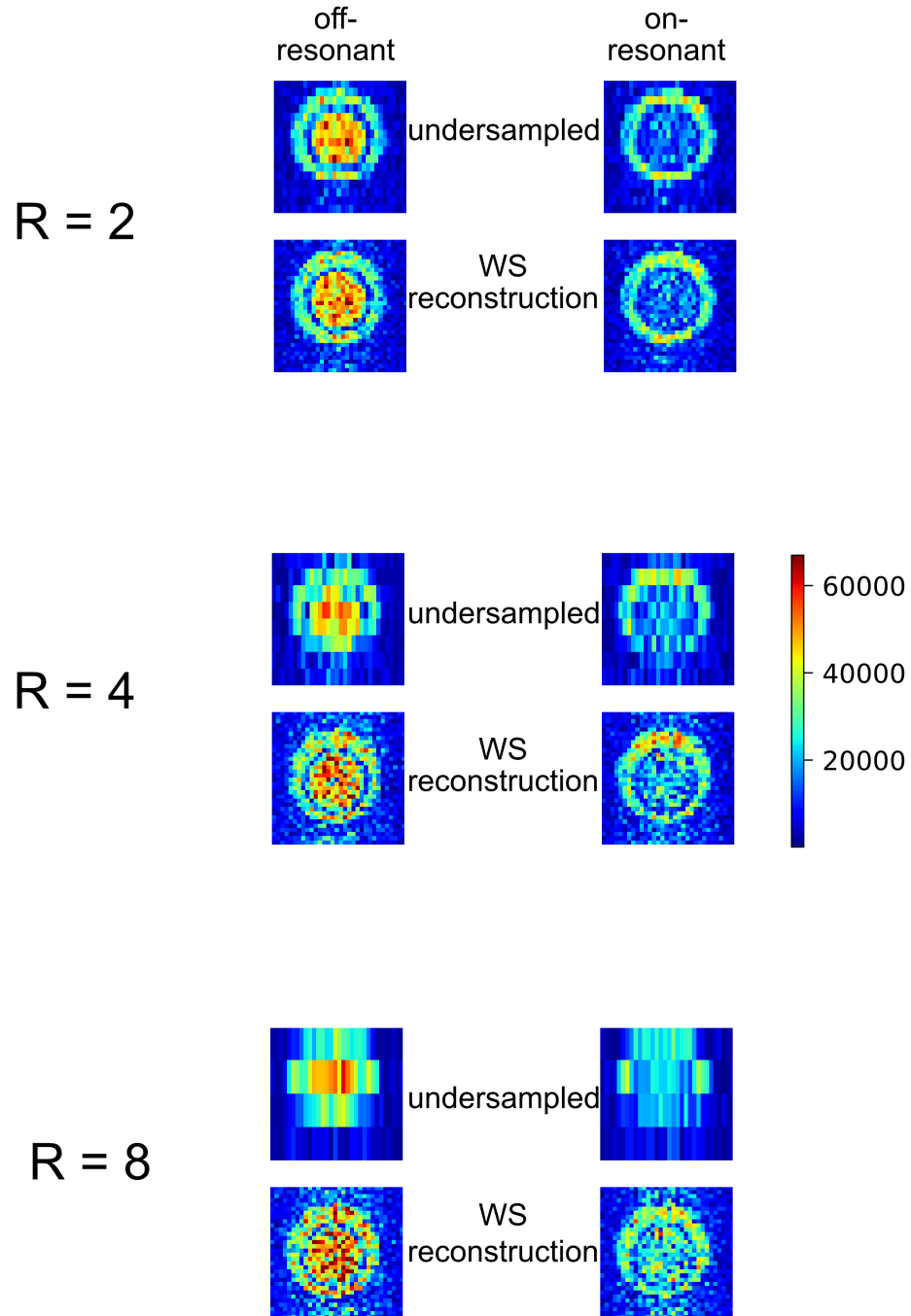


Figure 2.6: Undersampling and WS reconstruction of  $^{129}\text{Xe}$  images. Undersampled images lose their sharpness as the undersampling factor increases (top to bottom  $R = 2, 4, 8$ ). WS reconstruction retrieves the sharpness and preserves the contrast between the phantom compartments, however with reduced (visual) accuracy for  $R = 8$ .

designed to artificially increase the resolution by introducing lines of zeros after each line of true signal sampling. However, the addition of empty lines is only done at the stage of image reconstruction and the raw k-space data includes only the true signal lines, which can be as low as 4.

Scans were done using a modified RARE sequence with a CEST preparation block. To saturate the magnetization in the inner compartment, a RF pulse of 10 s and 6  $\mu$ T was applied on-resonant with the frequency of  $^{129}\text{Xe@CrA}$  of  $-132$  ppm (14604 Hz). WS-reconstructed images from the on- and off- resonant cases are shown in Fig. 2.6. They were created using the same procedure described in the  $^1\text{H}$  implementation. Notably, the phantom geometry is retrieved in WS images compared with the under-sampled images. WS also preserves the contrast between the compartments, albeit with some reduced quality for the maximal undersampling factor of  $R = 8$ . Additional acquisition parameters are:  $TE = 10.7$  ms and  $TR = 10.35$  s for the fully-sampled images, for the undersampled data (from all undersampling factors)  $TE = 10.5$  ms and  $TR = 10.18$  s. The RARE factor was set to the number of phase encoding steps. The gas mixture bubbled into the sample comprised 5% xenon (natural abundance of 26.4% of the isotope  $^{129}\text{Xe}$ ), 10% nitrogen and 85% helium. Bubbling time was 10 s, followed by a delay of 4 s to let bubbles to collapse.

SS reconstructions for the two offsets (off-resonant and on  $^{129}\text{Xe@CrA}$  resonant frequency) were also created following Eq. 2.1. The same pulse sequence and acquisition parameters were used as for WS reconstructions. SS reconstructions showed equal visual quality as WS reconstructions for the three undersampling factors ( $R = 2, 4, 8$ ) and a quantified comparison for the imaging-based z-spectra derived from SS/WW images is discussed below.

Undersampling with  $^{129}\text{Xe}$  was done by acquiring images with a reduced number of phase encoding steps, unlike in the  $^1\text{H}$  implementation where undersampled images were cut out of the fully-sampled k-space followed by FT. In the  $^{129}\text{Xe}$  implementation, by keeping the FOV equal in the reference and the keyhole images, the steps size in k-space  $\Delta k_1, \Delta k_2$  is also kept equal ( $FOV = 1/\Delta k_i$  in each direction) and then acquiring a reduced number of phase encoding in the keyhole images provides the right range of low frequencies that will be complemented by the high frequencies

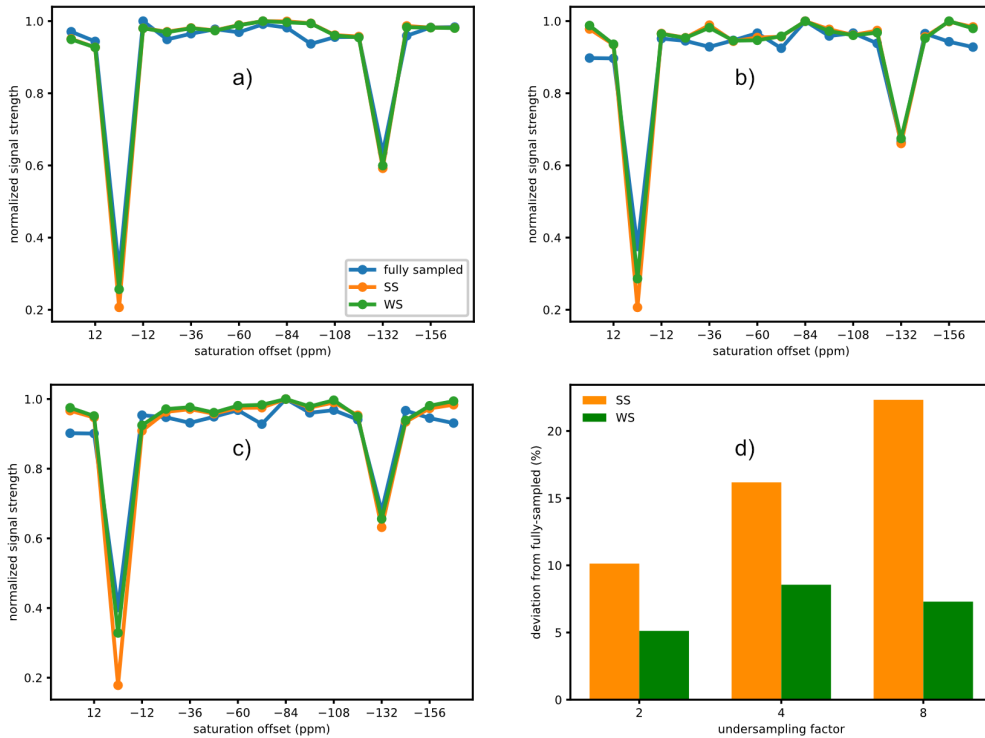


Figure 2.7: Z-spectra from keyhole reconstructions with different undersampling factors of: a)  $R = 2$ , b)  $R = 4$  and c)  $R = 8$ . d) Comparison of SS/WS (orange/green) signal deviations from fully sampling at 0 ppm for the three undersampling factors in a-c. A good agreement between the spectra is displayed.

from the reference images in the process of their merging. A comparison between undersampled proton data that was acquired in the two ways (reduced number of phase encoding steps and cutting out from fully-sampled) was done by calculating the pixel-wise relative error in image space and k-space and showed a good agreement between the two.

To compare the z-spectra derived from fully-sampled  $^{129}\text{Xe}$  images and from SS-/WS- reconstructed images, an imaging series of 17 offsets between  $-168 - 24$  ppm ( $-18587 - 2655$  Hz) in 12 ppm (1328 Hz) steps was acquired. This range is designed to cover the the Xe@H<sub>2</sub>O (at 0 ppm) and Xe@CrA (at  $-132$  ppm) resonance frequencies, additional three offsets were acquired at the beginning of each spectrum and served as dummy scans to stabilize the gas flow. The signal level at each offset is derived from the images by taking the averaged pixel value over a defined ROI around the

phantom (see Fig. 2.4).

Fig. 2.7 displays these spectra for undersampling factors  $R = 2, 4$  and  $8$ . A good agreement between the shapes of the fully-sampled spectra (blue) and the SS/WS spectra (orange/green) can be seen. This is consistent with the observation in Fig. 2.6 that SS/WS methods preserve the contrast and thus the two peaks at  $0$  and  $-132$  ppm appear in their spectra. Overlapping of the orange/green baselines in between the two peaks with the blue baseline in each sub figure a-c are also quite reasonable, considering that: *i*)  $^{129}\text{Xe}$  images are more noisy (relative to  $^1\text{H}$ ) where this noise generates a variation from image to image and *ii*) the signal level in  $^{129}\text{Xe}$  images depends on the stability of the xenon delivery between the images. These two aspects create the fluctuations that appear along the baseline. However, the stability is reasonable considering that each spectrum (blue/orange/green) is based on a separate image series which can be acquired on different days with different performance level of the polarizer. The averaged errors (over each spectrum points) of SS from fully-sampled are 2.2%, 3.4% and 4.2% and of WS from fully-sampled are 1.9%, 3% and 3.4% for the spectra appear in sub figures a,b and c, respectively. The higher averaged error for both SS and WS with  $R = 8$  is consistent with the visual quality of their images appeared in Fig. 2.6.

In Fig. 2.7d, the signal level deviation between fully sampled and SS/WS at  $0$  ppm are shown. First, it is noticed that these deviations are larger than seen for  $^1\text{H}$  (see Fig. 2.5). A reason for that is the lower SNR in  $^{129}\text{Xe}$  images, i.e.,  $\sim 10\%$  of  $^1\text{H}$ , the relative noisy images make the quantification of signal level (ROI analysis) less robust. At  $0$  ppm the deviation of WS from fully sampled (green bars) is lower than the deviation of SS from fully sampled (orange bars) for each tested undersampling factor. This is because in WS data completion in the periphery is done from a linear combination of the data with direct saturation (at  $0$  ppm) and without saturation (at an off-resonant offset), thus it is expected that the WS reconstruction in these two offsets to be quite accurate. However, in SS reconstruction the  $0$  ppm offset involves data completion in the periphery from the off-resonant offset only, thus it has a larger dissimilarity to the fully sampled data at this offset. To support this argument the values assigned to the two weights in the WS reconstructions are listed in table 2.1.

Table 2.1: WS weights at 0 ppm.  $w_1$  multiplies the data at the off-resonant saturation frequency (without saturation) and  $w_2$  multiplies the data at the 0 ppm saturation frequency (with direct saturation).

$R$	$w_1$	$w_2$
2	0.02	0.731
4	0.091	0.577
8	0.035	0.706

The higher  $w_2$  value relative to  $w_1$  points that in the representation of information a higher emphasis was given to the data from the direct saturation and that is for all tested  $R$  values.

Finally, whereas WS deviations remains more or less the same for all tested undersampling factors, Fig. 2.7d also illustrates the trend of increasing deviations of SS as the undersampling factor increases. The explanation for this trend relates to the larger size of the periphery domain for higher undersampling factors. This domain is multiplied by  $\beta$  which has a near zero value at 0 ppm (due to the direct saturation), this means that as  $R$  increases, a larger proportion of k-space is assigned to low values. The values in the periphery of k-space are associated with the image noise levels [26]; the lower these values, the lower the image noise. Thus increasing  $R$  leads to less noise in the SS images and since saturation of the signal is down to the noise level, we get lower signal values for higher undersampling factors at 0 ppm (and higher deviations from fully sampled). The deviations of SS/WS for the CEST offset ( $-132$  ppm) are minor with less than 5% for all tested  $R$  values.

$^1\text{H}$  and  $^{129}\text{Xe}$  keyhole experiments were done only as proof of concept since the acceleration in acquisition time and the increase of signal that have been achieved were minor. The main reasons for that are related to the pulse sequence used (RARE) and to the pre-encoding steps of magnetization preparation involved in HP  $^{129}\text{Xe}$  imaging. They will be described in more details in the next chapter. By combining the keyhole approach with VFA excitation and with averaging (which will be termed CAVKA), more substantial acceleration and signal increase will be provided.

### 3 CAVKA- Combined approach of VFA, keyhole and averaging

CAVKA is a novel method based on keyhole view sharing. It was tailored to provide more substantial acceleration and signal amplification in HyperCEST acquisition than the original keyhole approach. When implementing keyhole encoding, acquiring a sub domain of k-space (the keyhole domain) with the RARE sequence doesn't provide meaningful signal amplification: in the RARE sequence, an initial  $90^\circ$  excitation pulse is applied followed by a  $180^\circ$  refocusing pulse before the encoding of each echo (line in k-space). The signal decay along the echos is a  $T_2$  decay and truncating the number of echoes does not change the signal level in the first echoes regardless how many echoes were truncated. However, the aim was to control the use of the available magnetization to achieve higher signal level in the echoes, when fewer of them are acquired. To that end, VFA was employed: it enables adjusting the signal level of the echoes according to their total number and to achieve, among other advantages, the desired aim. VFA was initially introduced [27] as a way to achieve equal levels of magnetization along the echoes, and using it within CAVKA benefits also from this feature.

As for the acceleration of the acquisition, the keyhole encoding does not change that the slowest steps in HyperCEST imaging are the bubbling time of xenon into the sample and the duration of the CEST saturation pulse. The keyhole-based reduction in the number of echoes does not provide meaningful time saving. The central challenge is to achieve acceleration when the bubbling time is more or less fixed and exist in every image acquisition. This is where selective averaging comes into play. It involves the repeated acquisition of one element of the overall data set to form one improved image. This averaged image and reuse of its raw data for retrieving the peripheral k-space of a keyhole imaging series provides an acceleration relative to the individual averaging of each image in the series. Incorporation of averaging into the keyhole scheme makes the CAVKA method especially relevant for applications that tackle high noise (or low SNR) while keeping the acquisition time reasonable.

Multiple-component methods have the advantage of tackling multiple issues, each

being addressed by one component. However, while one component isolated from the others shows a desired effect, its combination with the other components could turn out harmonic or destructive. To assess the components joint effect, combinations of applying the components to varying degrees can be tested. Usually each component (method) has a parameter that can take several values, changing this values for each component and constructing some of their combinations provides a way to achieve the assessment of the components' joint performance. Additionally, if the method relays on well known theoretical concepts, experiments can be designed to test these concepts. The challenge then is to find the appropriate experimental variables to quantify the theoretical predictions. Some quantifications might not be straightforwardly accessible, e.g., pixel-wise ratios under noise conditions.

For new methods that provide acceleration [16, 28, 29], not only the acceleration factor itself is of interest but also the consistency of the data collected by using the new methods when compared to the corresponding data from the conventional (slower) method. To this end, some data comparisons of images are needed and accordingly in an accelerated CEST acquisition the comparison between z-spectra derived from such images is required. Acceleration-providing methods make some experiments feasible that otherwise would take too long to be considered as practical. Another advantage of the acceleration when performed with spatial encoding is the possibility to collect the data from multiple samples (simultaneously) to make a study more comprehensive, or to allow for comparative studies.

Consistency checks with experimental data can sometimes be limited. This is the case when the experimental setup does not allow to test for certain features. High resolution imaging and image contrast in small regions or within objects of complex geometries are examples for such features. However, testing for the robustness of new methods with the resolutions and geometries (or contrast patterns) that are not (yet) feasible experimentally is important, and especially if the method might be applied in other types of serial imaging beyond CEST [30–33]. Accordingly, simulation of image data can come in handy and thus a digital phantom with a more complicated geometry than our experimental phantom was also simulated. It enabled insights into high resolution imaging and detailed investigations of the potential artefacts and

errors in CAVKA images, as well as investigations of the noise patterns in the hybrid CAVKA k-spaces. This might be of minor relevance in a clinical application.

### 3.1 Components of the CAVKA method

The CAVKA method is a novelty based on the keyhole scheme (with the scaled substitution computation) that involves pulse programming at the MRI scanner and post acquisition computational steps. It is complemented by theoretical considerations. The novel ideas that were introduced in CAVKA are: the use of an averaged reference image, enhancing the keyhole images by using VFA and careful evaluation of the substitution factor. Both for the reference and the keyhole images, the flip angle for each k-space line (denoted  $n$ ) out of a total of  $N$  lines is adjusted according to the VFA formula [27] to achieve  $N$  equal transverse magnetizations:

$$\theta_{\text{VFA}}(n) = \arctan\left(\frac{1}{\sqrt{N-n}}\right), \quad n = 1, 2, \dots, N. \quad (3.1)$$

#### 3.1.1 VFA aspects

Before the encoding of the first k-space line, the 3D magnetization vector  $M$  points in the z-direction and has a magnitude  $M_0$ . For the encoding of the first k-space line, the vector is tilted by an angle  $\theta$  (the flip angle) relative to the z-axis. Decomposition of the vector into its longitudinal component (z-axis) and transverse component (in the xy-plane) yields  $M_z = M_0 \cos(\theta)$ ,  $M_{xy} = M_0 \sin(\theta)$ . This kind of tilting and decomposing is valid for each of the sequential encoding of k-space lines with replacing  $M_0$  with  $M_z$  of the previous excitation. The use of flip angles according to Eq. 3.1 delivers equal levels of transverse magnetization ( $M_{xy}$ ) along  $N$  lines. Although  $\theta_{\text{VFA}}(n)$  is a monotonic increasing function of  $n$ , the longitudinal magnetization ( $M_z$ ) is used up from line to line and this combination yields the equal amounts of transverse magnetization.  $\theta_{\text{VFA}}(n)$  also has a monotonic decreasing dependency on  $N$  which provides the optimized use of the available magnetization, i.e., reducing the number of k-space lines leads to a higher transverse magnetization in each line, as illustrated in Fig. 3.1. VFA excitation is also used in the acquisitions of the reference image, yet for another reason than optimizing the use of the magnetization. In the reference

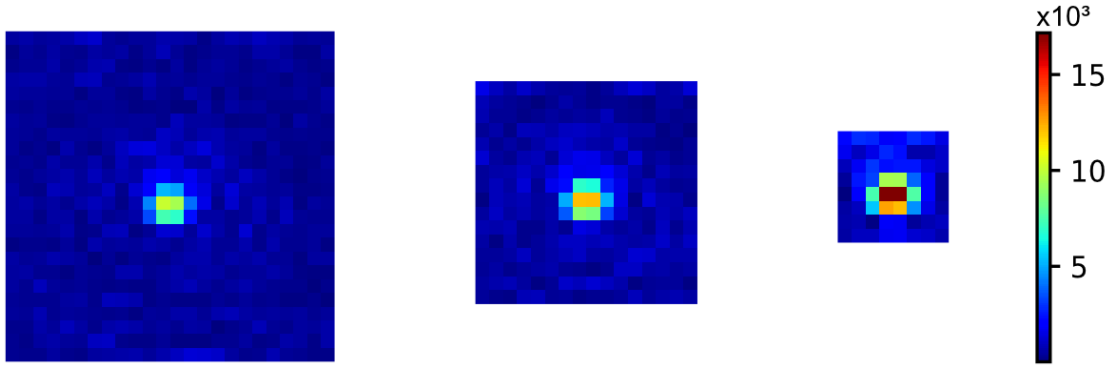


Figure 3.1: Optimizing the use of the magnetization, principle demonstration. Left to right: keyhole domains with size  $24 \times 24$ ,  $16 \times 16$  and  $8 \times 8$  acquired with VFA excitations. Higher signal level is encoded along the rows of smaller domains. Experimental k-space data of  $^{129}\text{Xe}$  detection are displayed.

image, the use of VFA facilitates the scaling of the merged data (keyhole + reference) according to an analytical derivation as will be explained later.

### 3.1.2 Averaging aspects

Whereas VFA amplifies the signal in the keyhole domain, averaging decreases the noise in the reference image. This denoising effect is achieved due to the noise properties in MR images; it is random, additive, complex and in each of its real and imaginary parts it is normally distributed with zero mean and constant standard deviation [34]. Taking the perspective that one image is one sample of signal with noise and denoting the noise  $x_i$ ,  $i = 1, 2, \dots, d$  ( $d$  is the image resolution), one can write  $x_i \sim \mathcal{N}(0, \sigma^2)$ , where  $\sigma^2$  is the noise variance ( $\sigma$  is the noise standard deviation). By applying the basic properties of the variance, averaging of  $N$  samples (images) would result with decreased noise variance as follows:

$$\text{Var} \left( \frac{1}{N} \sum_{n=1}^N x_i \right) = \frac{1}{N^2} \text{Var} \left( \sum_{n=1}^N x_i \right) = \frac{1}{N^2} \sum_{n=1}^N \text{Var}(x_i) = \frac{1}{N^2} \cdot N\sigma^2 = \frac{\sigma^2}{N} \quad (3.2)$$

This means that the noise variance is reduced by  $N$  and thus the noise level (standard deviation), which is the square root of the variance, is reduced by  $\sqrt{N}$  in the averaged

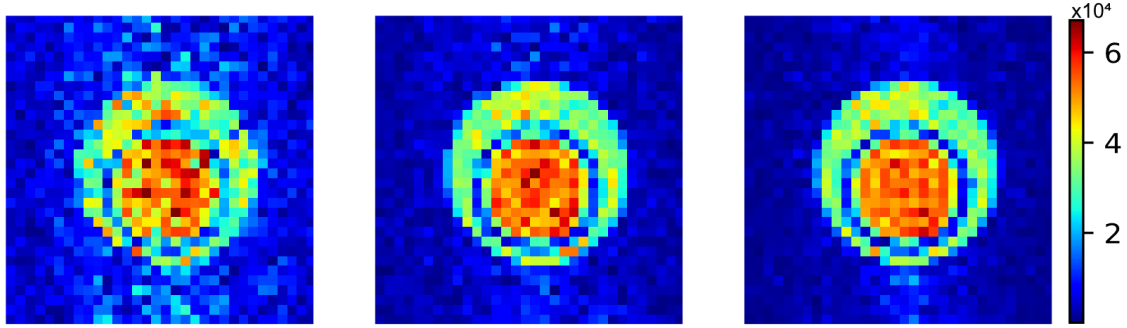


Figure 3.2: Averaging effect in MR imaging. Left to right: averaged images from 1, 4 and 9 acquisitions. Lower noise level is displayed when the averaging is done with a higher number of replicates.  $^{129}\text{Xe}$  experimental imaging data.

image. This holds separately for the real and imaginary noise components. Image data comprises the sum of signal and noise, by averaging multiple replicates of one image, the signal value remains practically unchanged but the noise is reduced as described. Fig. 3.2 demonstrates the effect of averaging in imaging.

### 3.1.3 Substitution factor aspects

Reconstruction of undersampled k-space within the CAVKA method follows the SS computation (Eq. 2.1 in section 2.1), but  $\beta$ , the substitution factor, is calculated in a novel way. The substitution factor scales signal intensities in the k-space periphery to generate a smooth transition between the periphery and the keyhole domains. To demonstrate the importance of the substitution factor, its impact on image reconstruction is shown in Fig. 3.3. In the case of using VFA in the encoding of both the reference and the keyhole images,  $\beta$  can be analytically derived. The transverse magnetization  $M_{xy}$  in the  $n$ -th excitation depends on the amount of longitudinal magnetization  $M_z$  of the previous excitation  $n - 1$  and on the flip angle. Thus,  $M_{xy}$  in the  $n$ -th k-space lines is

$$M_{xy}(n) = M_z(n - 1) \cdot \sin(\theta_{\text{VFA}}(n)), \quad n = 1, 2, \dots, N. \quad (3.3)$$

Comparing the signal in the keyhole k-space lines with the signal in the reference

k-space lines yields the general form of the substitution factor

$$\beta = \frac{M_{xy}(n)_{\text{key}}}{M_{xy}(n)_{\text{ref}}} \quad (3.4)$$

Critically, VFA excitations make the transverse magnetization across the k-space lines uniform. Therefore, we can compare the signal from a single arbitrary line in the keyhole k-space to its corresponding line in the reference k-space. Choosing the first line from both domains provides an elegant solution, since with substitution of  $n \neq 1$  the terms would not simplify as conveniently as follows. The end result is, nonetheless, valid in general since the transverse magnetization remains constant for all lines within each data set and can be taken from the respective first line  $n = 1$ . The phase encoding applied in either the fully sampled reference data or the sub-sampled keyhole causes different segmentation of the overall available magnetization but the suggested analytical scaling does not change. The phase encoding rather just scales the line-wise signal magnitude. Let  $R$  be the undersampling factor, substituting Eq. 3.1 and Eq. 3.3 into Eq. 3.4:

$$\begin{aligned} \beta &= \frac{M_{xy}(n)_{\text{key}}}{M_{xy}(n)_{\text{ref}}} = \frac{(M_z(n-1) \cdot \sin(\theta_{\text{VFA}}(n)))_{\text{key}}}{(M_z(n-1) \cdot \sin(\theta_{\text{VFA}}(n)))_{\text{ref}}} \\ &= \frac{M_z(n-1)_{\text{key}}}{M_z(n-1)_{\text{ref}}} \cdot \frac{\sin\left(\arctan\left(\frac{1}{\sqrt{N/R-n}}\right)\right)}{\sin\left(\arctan\left(\frac{1}{\sqrt{N-n}}\right)\right)} \\ &= \frac{M_z(n-1)_{\text{key}}}{M_z(n-1)_{\text{ref}}} \cdot \frac{1}{\frac{1}{\sqrt{N/R-n+1}}} \stackrel{n=1}{=} \frac{M_0}{M_0} \cdot \frac{\sqrt{N}}{\sqrt{N/R}} = \sqrt{R} \end{aligned} \quad (3.5)$$

In this derivation, the identity  $\sin(\arctan(1/\sqrt{x})) = 1/\sqrt{x+1}$  was used and the initial longitudinal magnetization is  $M_0$ .

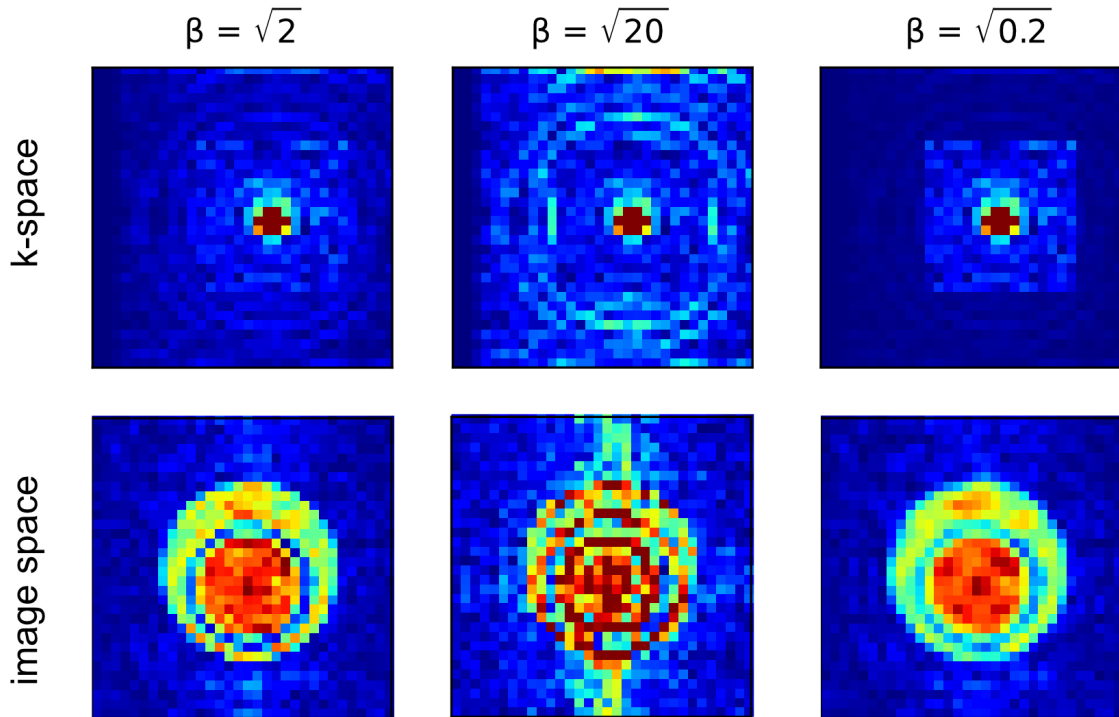


Figure 3.3: Importance of the substitution factor. Left to right: analytically derived value ( $\beta = \sqrt{2}$ ), overestimated value ( $\beta = \sqrt{20}$ ) and underestimated value ( $\beta = \sqrt{0.2}$ ) in k-space (top row) and image space (bottom row). An overestimated value leads to a noisy image and an underestimated value leads to blurring. Experimental  $^{129}\text{Xe}$  data with keyhole size of  $16 \times 16$  ( $R = 2$ ) and reference image size of  $32 \times 32$ .

### 3.1.4 Assembling the required steps for CAVKA

The implementation of the CAVKA method involves the following steps:

1. Acquisition of a fully sampled averaging series with unperturbed starting magnetization and with VFA.
2. Averaging (computationally) the multiple replicates to form one averaged reference image.
3. Acquisition of an undersampled (keyhole) CEST imaging series that benefits from higher starting magnetization by the use of VFA.
4. Merging (computationally) the keyhole series with the (peripheral) data of the

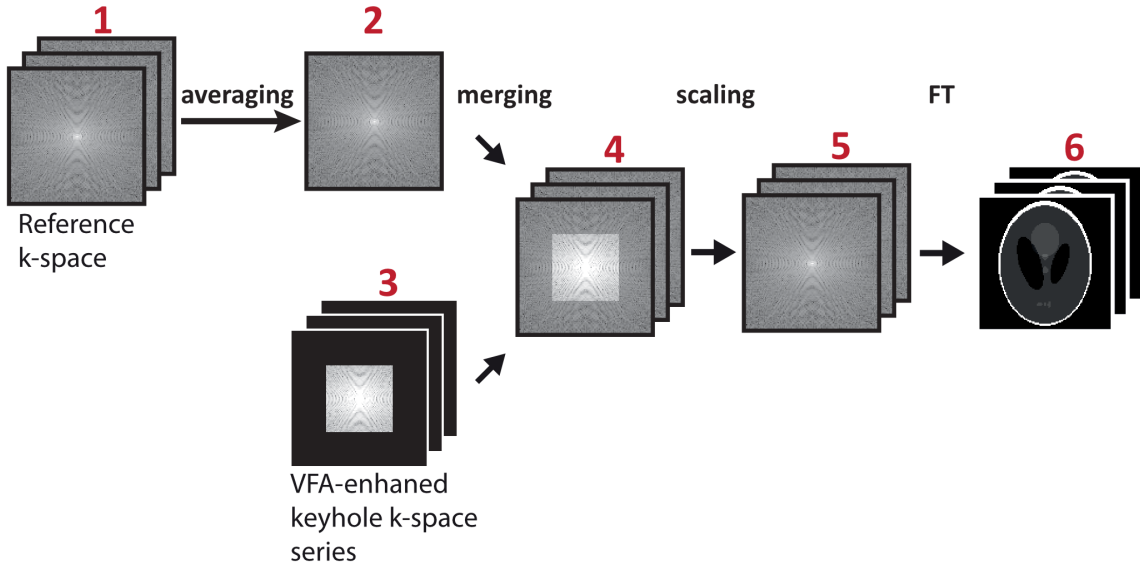


Figure 3.4: Illustration of the CAVKA method. 1) Acquisition of fully sampled averaging replicates using adapted VFA. 2) One averaged reference data is formed by (complex-valued) averaging of the replicates from the previous step. 3) Acquisition of an undersampled (keyhole) imaging series using adapted VFA. 4) Hybrid k-spaces are created by merging the keyhole series with the averaged reference data. 5) Scaling of hybrid k-spaces according to Eq. 3.1. 6) Final CAVKA images are obtained by Fourier transforming the k-space data; the Shepp-Logan virtual phantom [35] was used for illustration.

averaged reference image.

5. Scaling the hybrid k-space according to the analytically derived substitution factor.
6. Image reconstruction of the hybrid k-space data by applying the discrete Fourier transform.

Fig. 3.4 displays a flowchart of all the above steps of the CAVKA method. Throughout this thesis, squared keyhole regions are acquired as stripes with  $N$  frequency and  $N/R$  phase encoding steps ( $R \geq 1$  is the undersampling factor). After the acquisition, the stripes are trimmed into squares of the desired size of  $N/R \times N/R$ . This procedure simplifies the acquisition and eliminates several potential sources of errors as explained in more detail in the discussion section.

## 3.2 Acceleration and xenon saving provided by CAVKA

Xenon MR imaging includes the steps of xenon gas delivery which is typically 10 – 15 s and allowing the bubbles to collapse which is typically  $\leq 5$  s. The combined delivery time  $t_{\text{del}}$  limits the acceleration factor of the CAVKA acquisition to be approximated as  $N_\omega \cdot NA / (N_\omega + NA)$  (see derivation in section 3.2.1). However, for other applications, where the acquisition time is equal to the total encoding time, i.e., the acquisition time is the multiplication of  $TR$  (the repetition time between two phase encoding steps) with the number of phase encodes and with the number of images and/or averages, a higher acceleration factor can be achieved. This factor is given by  $N_\omega \cdot R \cdot NA / (N_\omega + R \cdot NA)$  (see derivation in section 3.2.3). The formulas are based on a constant  $TR$  for all images.  $t_{\text{sat}}$  is the duration of the saturation pulse (part of the CEST preparation block) and is typically on the order of  $t_{\text{del}}$ . The derivation in this case is as follows:

### 3.2.1 Acceleration factor for HyperCEST

The acquisition time of a fully sampled and averaged imaging series is given by

$$t_{\text{fully sampled and averaged}} = (t_{\text{del}} + t_{\text{sat}} + N_{\text{PE}} \cdot TR) \cdot NA \cdot N_\omega.$$

$N_{\text{PE}}$  is the number of phase encoding steps,  $NA$  is the number of averages and  $N_\omega$  is the number of saturation frequency offsets. In CAVKA, one fully sampled and averaged reference image and  $N_\omega$  keyhole images (without averages) are acquired. Thus, the total time is given by:

$$t_{\text{CAVKA}} = (t_{\text{del}} + t_{\text{sat}} + N_{\text{PE}} \cdot TR) \cdot NA + (t_{\text{del}} + t_{\text{sat}} + N_{\text{PE}}/R \cdot TR) \cdot N_\omega.$$

The acceleration factor is given by the ratio of both acquisition times:

$$\begin{aligned} \frac{t_{\text{fully sampled and averaged}}}{t_{\text{CAVKA}}} &= \\ &= \frac{(t_{\text{del}} + t_{\text{sat}} + N_{\text{PE}} \cdot TR) \cdot NA \cdot N_\omega}{(t_{\text{del}} + t_{\text{sat}} + N_{\text{PE}} \cdot TR) \cdot NA + (t_{\text{del}} + t_{\text{sat}} + N_{\text{PE}}/R \cdot TR) \cdot N_\omega} \\ &\stackrel{TR \ll t_{\text{del}}}{=} \frac{(t_{\text{del}} + t_{\text{sat}}) \cdot NA \cdot N_\omega}{(t_{\text{del}} + t_{\text{sat}}) \cdot NA + (t_{\text{del}} + t_{\text{sat}}) \cdot N_\omega} \\ &= \frac{NA \cdot N_\omega}{NA + N_\omega}. \end{aligned} \tag{3.6}$$

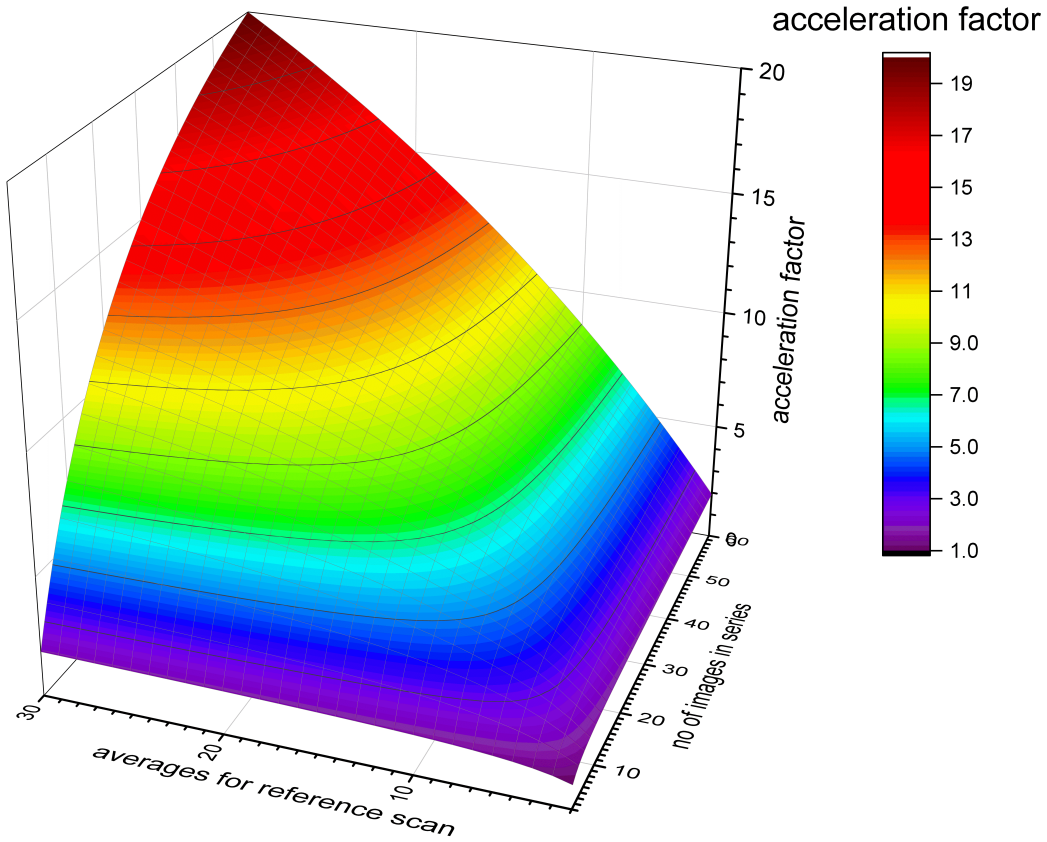


Figure 3.5: HyperCEST acceleration by CAVKA. Dependencies on the number of averages (of the reference image) and the number of offsets (images) in the HyperCEST spectrum are shown.

The overall behavior of the acceleration factor as a function of the number of averages of the reference image and the extent of the imaging series is shown in Fig. 3.5.

### 3.2.2 Xenon deliveries saving

The number of xenon deliveries for a fully sampled and averaged series is  $NA \cdot N_\omega$ . In CAVKA, however, we acquire one fully sampled and averaged reference image and  $N_\omega$  keyhole images. The number of deliveries is therefore  $NA + N_\omega$ . The saving factor regarding the gas deliveries is given by the ratio of the number of deliveries:

$$\frac{NA \cdot N_\omega}{NA + N_\omega}.$$

### 3.2.3 Acceleration factor for other types of imaging series

For generality, we assume an application without a pre-readout preparation block. The calculation remains the same as for HyperCEST but  $t_{\text{del}}$  and  $t_{\text{sat}}$  can be omitted (no delivery and no saturation times):

$$\frac{t_{\text{fully sampled and averaged}}}{t_{\text{CAVKA}}} = \frac{N_{\text{PE}} \cdot TR \cdot NA \cdot N_{\omega}}{N_{\text{PE}} \cdot TR \cdot NA + N_{\text{PE}}/R \cdot TR \cdot N_{\omega}} = \frac{NA \cdot N_{\omega} \cdot R}{R \cdot NA + N_{\omega}}.$$

Applying CAVKA to acquire an imaging series with, for example, 35 offsets would result in acceleration factor of ca. 17, instead of just  $\sim 7$  in HyperCEST.

## 3.3 CAVKA simulations in digital phantom

To investigate potential artefacts and errors in CAVKA images, a simulated image data set was created. A z-spectrum imaging series can be simulated by assigning magnetization values pixel-wise from the numerical solution of the Bloch-McConnell (BMC) equations [8]. BMC equations solver was already used extensively within our group as part of the qHyperCEST framework [9], however the implementation for the solver used to simulate CAVKA images can be found in [36]. The BMC equations describe the time evolution of the macroscopic magnetization in the case of two (or more) magnetization pools that are under spin exchange (see section 1.5). For example, one spin pool represents  $^{129}\text{Xe}@H_2O$  (solution pool or bulk pool), the second pool represents  $^{129}\text{Xe}@\text{host}$  (CEST pool or dilute pool). The set of parameters which is part of the BMC equations and their values within this work are given in Table 1. Solution of the BMC equations for  $t \leq t_{\text{sat}}$  and for a given saturation offset yields an FID which after Fourier transformation yields a Lorentzian line shape. Plotting the line intensity versus the saturation offset yields for each saturation response an exponential Lorentzian function with a width  $\Gamma$  around a center  $x_0$ . This is defined as  $e^{-L(\Gamma, x_0)}$ . Solving the BMC equations for each offset in the z-spectrum provides the simulated signal values in the imaging series (that follows the saturation frequency dimension). By defining multiple domains within one image (inspired by the Shepp-Logan virtual phantom [35]) that correspond to different parameter values, different

Table 3.1: Parameter values used in BMC equations.

Parameter	Value	Remarks
$B_0$	9.4 T	
$B_1$	5 $\mu$ T	
$t_{\text{sat}}$	20 s	
shape	'CW' (continuous wave)	shape of saturation pulse
$T_1$	2 s	in bulk and dilute pools
$T_2$	0.2/0.15 s	in bulk/dilute pool
bulk pool fractional size	0.8/0.9/1	in three compartments
dilute pool fractional size	0.1/0.4/0.5 %	in three compartments
exchange rate	500 Hz	
number of pools	2	
number of offsets	41	ca. 120 ppm spectral width
on-resonant frequency	120/0 ppm	in dilute/bulk pool

z-spectra are calculated for each of the domains. Thus, a contrast pattern can be designed within the image and can be studied under the CAVKA image acquisition and reconstruction approach. Fig. 3.6 displays the digital phantom.

To simulate averaging in the digital phantom, one needs to consider the noise properties under the discrete Fourier transform (DFT). DFT increases the noise level (standard deviation) by  $\sqrt{n}$ ,  $n$ - image resolution (no. of frequency encoding steps multiplied by the no. of phase encoding steps) [37], but DFT also includes a normalization factor in the form of multiplication by  $1/n$ . Depending on the direction of the DFT (forward or inverse) in which the normalization factor is applied, the noise level might be reduced by  $\sqrt{n}$ . In the Python package NumPy, the normalization factor is applied in the inverse DFT, meaning that the forward transform (k-space to image space) increases the noise level and the inverse transform decreases the noise level, either way by a factor of  $\sqrt{n}$ . In order to avoid affecting the noise level unevenly by applying DFT (or inverse DFT) to images of different resolutions, we start the noise processing in image space and end it in image space, this way the forward and inverse transformations are both applied and the division/multiplication by  $\sqrt{n}$  according to the image resolution is canceled out. Fig. 3.7 displays the noise distribution of one image after applying the inverse DFT. Noise was generated in a three-step process.

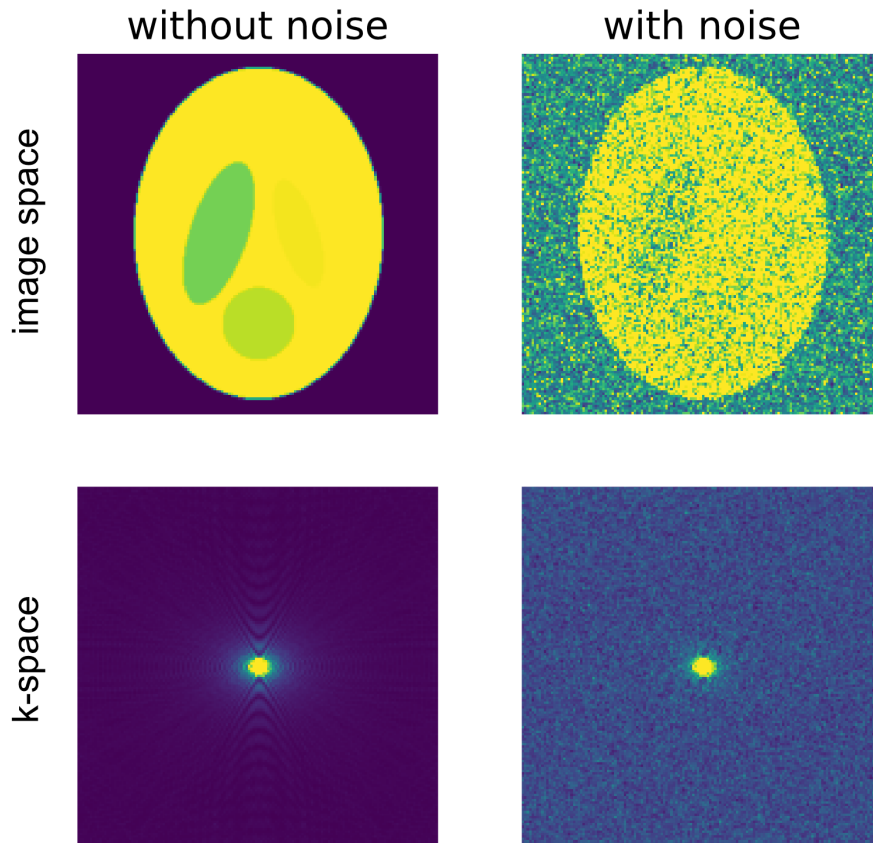


Figure 3.6: The digital phantom image of full resolution (size  $256 \times 256$ ). Image space and k-space view (top and bottom rows) of the simulated magnetization based on the BMC equations in the first offset of the imaging series (at 110 ppm). The corruption of noise is shown (right vs. left columns), when the noise level (standard deviation) is  $2/3$  and signal range is  $0 - 1$ . The phantom comprises four compartments with different magnetization levels.

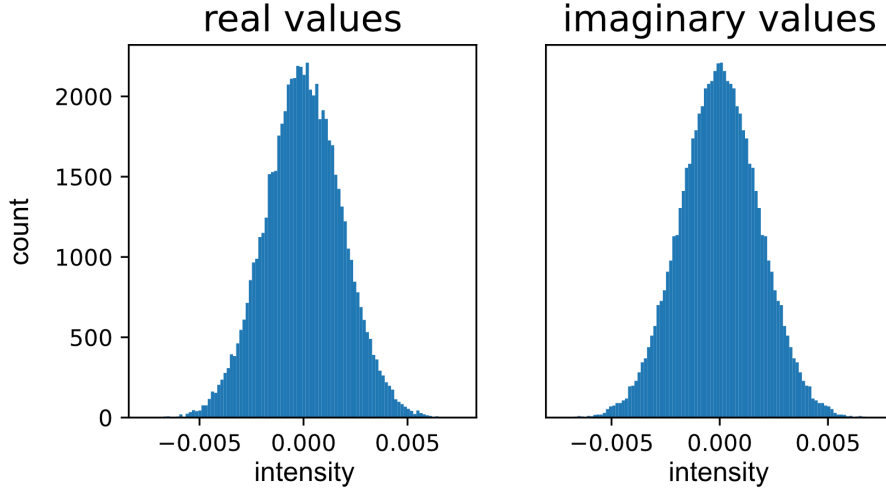


Figure 3.7: Noise distribution in one image after inverse FT (in k-space). In each noise component for real/imaginary signal the standard deviation is 0.0018 which is a reduction by 256 (image resolution  $256 \times 256$ ) from the expected standard deviation (of  $\sqrt{(2/3)^2/2}$ ) according to noise level (of  $2/3$ ) added in image space.

In the first step, normally distributed real-valued noise with zero mean and standard deviation of  $2/3$  was added to a noise-free image. This is repeated to obtain a stack of 500 different noise-carrying images that are afterwards transformed to (complex) k-space. In a second step, a subtraction of the non-noisy data from each element of the noisy data stack yields an isolated noise data stack (500 elements) in k-space. In the third step, the average of randomly selected and complex-valued sets from the noise data stack was added to the noise-free data to create a k-space stack with a pre-selected number of (noise) averages (up to 49). Averaged images were then created by simply Fourier transforming the averaged k-space stack.

To simulate the VFA effect in the digital phantom, Eq. 3.5 turned out to be very helpful. It is clear from the VFA term (Eq. 3.1) that reducing the resolution of the keyhole images (thus reducing  $N$ ) increases their signal, yet instead of applying Eq. 3.1 to simulate the resulted signal increase for each keyhole size, Eq. 3.5 tells us that the signal increase is  $\sqrt{R}$  ( $R$ - undersampling factor) relative to a given full-resolution image. Thus, we can cutout the desired keyhole size from the full resolution data and simply multiply it by  $\sqrt{R}$  to simulate the VFA signal amplification.

## 3.4 Results and discussion

In the following subsections, all results are from double phantom experiments, which contained, unless stated otherwise, H<sub>2</sub>O in the outer compartment and CrA (10 μM in water + 0.2% DMSO) in the inner compartment. Scans were performed using a modified 2D FLASH sequence; that included a preceding CEST preparation block and a VFA scheme for the excitation pulses. <sup>129</sup>Xe imaging parameters were:  $TE = 5.6$  ms,  $TR = 12.2$  ms,  $FOV = 10 \times 10$  mm<sup>2</sup>, slice thickness = 20 mm,  $BW = 4$  kHz, encoding order = "centric", matrix(image resolution) =  $32 \times 32$ . Smaller matrix sizes for keyhole acquisitions were realized by changing the phase encoding interpolation parameter between 1 (matrix =  $32 \times 32$ ) and 8 (matrix =  $32 \times 4$ ). This parameter has the same meaning as  $R$  and appears in the nomenclature of CAVKA reconstructions, e.g., CAVKA-4 for an undersampling factor of 4. Averaging was done separately (outside ParaVision) on complex-valued raw data in Python. Xenon was 5% of the gas mixture (with 85% helium and 10% nitrogen) delivered to the sample. Bubbling was performed for 15 s and additional 3 s were added afterwards allowing potentially generated gas bubbles to collapse.

### 3.4.1 Experimental support to the analytically derived substitution factor

To validate the formula for the substitution factor (Eq. 3.5), we compared the calculated values with experimentally determined ones. The histograms in Fig. 3.8 show the pixel-wise ratios between signal intensities in the keyhole k-spaces and signal intensities in the equivalent areas in the reference k-spaces for six different undersampling factors between  $R = 1.33$  (Fig. 3.8A) and  $R = 8$  (Fig. 3.8F). Due to the decreasing number of pixels for increasing undersampling factors, the total number of counts varies between 576 (Fig. 3.8A) and 16 (Fig. 3.8F). Further, the different levels of transverse magnetization for different undersampling factors lead to a shift of the mode of the histograms towards higher values for higher undersampling factors. This shift clearly follows the prediction according to Eq. 3.5. The analytically derived substitution factors for all investigated  $R$  values (dashed orange lines in Fig. 3.8A-F) fit the mode of the histograms and thus the experimentally observed values

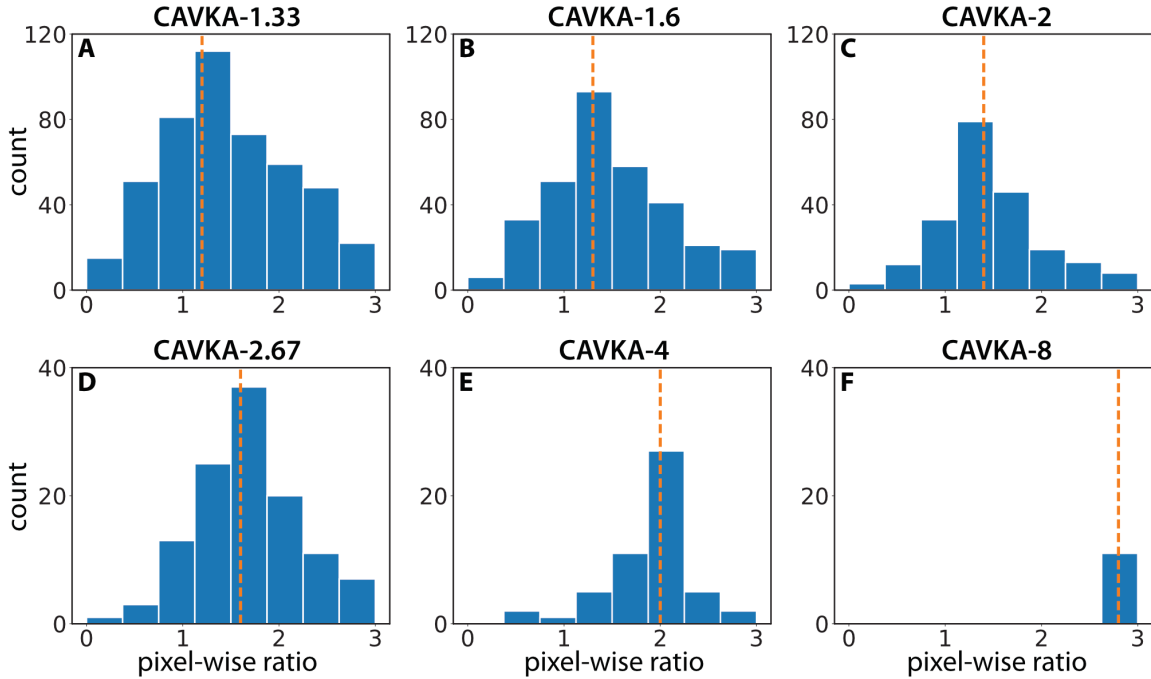


Figure 3.8: Experimental validation of the analytically derived substitution factor  $\beta$ . The histograms show the distribution of the pixel-wise ratios between signal intensities in the keyhole k-space pixels and the signal intensities in the corresponding reference k-space pixels. The dashed orange lines illustrate the analytically derived values according to Eq. 3.5. For all investigated undersampling factors between  $R = 1.33$  (A) and  $R = 8$  (F), the modes of the histograms match the theoretically predicted values.

very well. The choice of the correct substitution factor minimizes distortions in the reconstructed images that result from discontinuity in the signal intensity profiles of hybrid k-spaces. Fig. 3.3 demonstrates the effect of such discontinuities. Whereas overestimated  $\beta$  values lead to higher periphery values and thus to very noisy images (Fig. 3.3 middle), underestimated  $\beta$  values lead to high frequencies (in the periphery of k-space) with lower amplitudes and therefore to blurring (Fig. 3.3, right). This blurring due to underestimated  $\beta$  values is comparable to the effect of zero-filling.

### 3.4.2 Impact of keyhole size and number of averages on SNR

To study the SNR increase which is provided by CAVKA, we independently investigated the effect of the keyhole size on signal intensity (Fig. 3.9A) and the effect of

the number of averages on SNR (Fig. 3.9B), as well as the combined effect of both components (Fig. 3.9C). SNR is calculated as the mean of the signal ROI over the standard deviation of a comparative noise ROI of 49 pixels ( $\sim 5\%$  of total numbers of pixels) located in the top left corner of every image (see in Fig. 3.9C). All data shown in Fig. 3.9A were acquired without averaging. Following the calculations in Eq. 3.5, the signal intensity shows a square root dependency on the undersampling factor (shown by the linear graph with a slope of 0.5 in a log-log plot, Fig. 3.9A). Fig. 3.9B shows the general effect of averaging on SNR for acquisitions without using the keyhole approach. Following Eq. 3.2, the expected square root dependency of the SNR on the number of averages is observed. Finally, Fig. 3.9C shows the combined effect of averaging the reference image (and thus the k-space periphery) and enhancing the signal intensity in the keyhole region (due to the VFA approach). The plot shows the SNR as a function of the number of averages of the reference image for three different undersampling factors of  $R = 1.33$  (green),  $R = 2$  (orange) and  $R = 4$  (blue). In addition, the linear fit from Fig. 3.9B is included (dashed gray line) to show the theoretical SNR values when both, the periphery and the keyhole region, were averaged (at the cost of longer acquisition time). Importantly, for the investigated range, the SNR of the CAVKA method increases with increasing undersampling factors and almost reaches the level of the dashed reference line for CAVKA-4. In addition, for a fixed undersampling factor (e.g., blue data for CAVKA-4 in Fig. 3.9C), the SNR increases with increasing numbers of averages of the reference image. This effect is more dominant for higher undersampling factors (and thus smaller keyhole sizes) because larger fractions of the k-space data benefit from averaging the reference image. A possible limiting factor for the undersampling factor/keyhole size could be the capturing of dynamic changes in detailed (small) features of the image or along sharp edges. In our experiments, dynamic CEST contrast between the two compartments of the phantom was still captured using a  $8 \times 8$  keyhole size ( $R = 4$ ). This matter was also investigated in a four-compartment digital phantom that has a more complex geometry than the two-compartment phantom, see section 3.4.4.

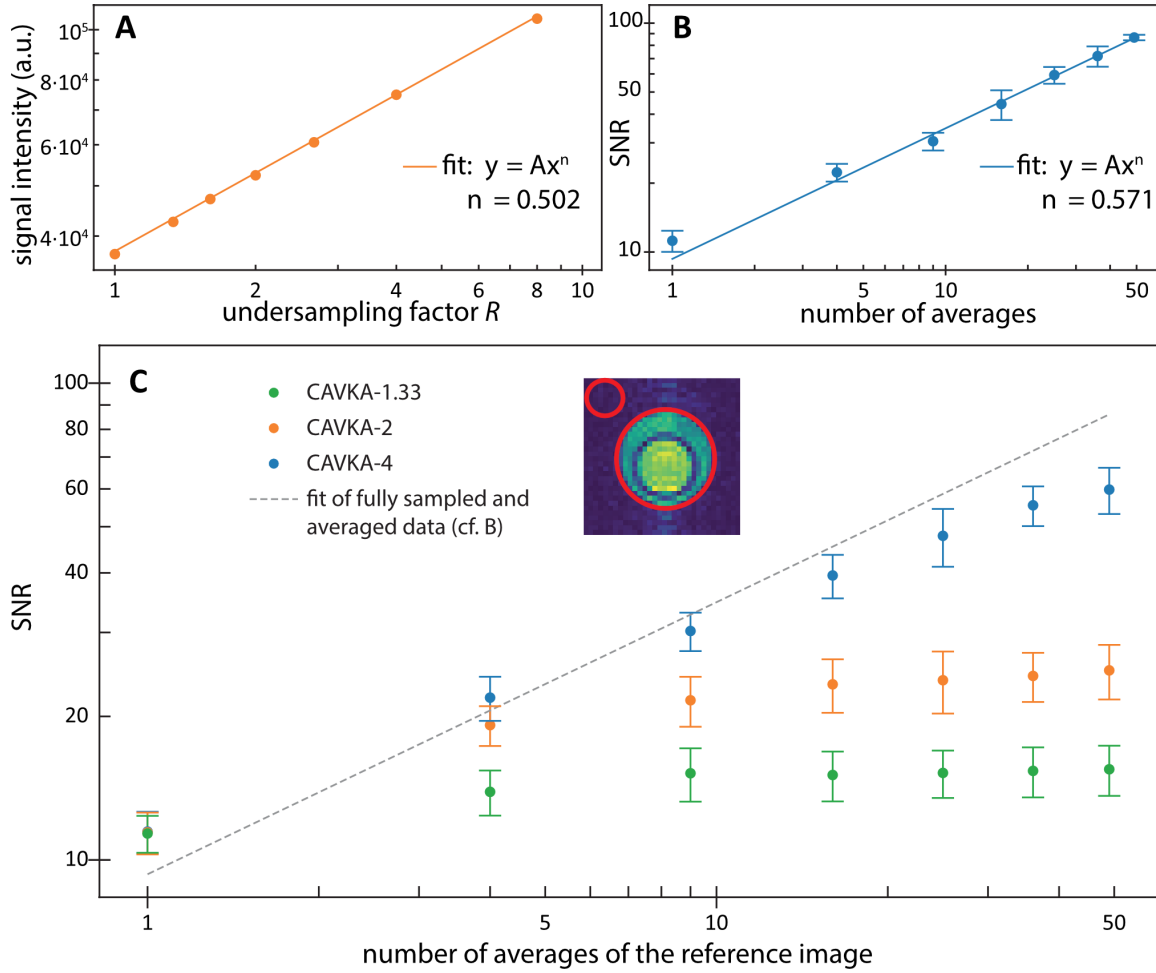


Figure 3.9: Signal and SNR dependencies in the CAVKA method. A) Signal intensity in non-averaged hybrid image vs. undersampling factor (error bars too small to be displayed). B) SNR in fully sampled images vs. number of averages. C) SNR in hybrid images with different combinations of undersampling factors ( $R = 1.33, 2$  and  $4$ ) and number of averages of the reference image. All data points represent the mean  $\pm 1$  standard deviation of 10 independent measurements. The inlay shows the signal and noise ROIs used to calculate SNR and signal intensity.

### 3.4.3 Acceleration in acquisition time by the CAVKA method

In this CEST acquisition, (RF) saturation pulse of 10 s and 15  $\mu\text{T}$  was used. Saturation was applied at 35 offsets ( $-149, -144, -139, -138, -137, -136, -135, -134, -133, -132, -131, -130, -129, -128, -127, -126, -125, -120, -115, -90, -45, -12, -9, -6, -3, -1.5, 0, 1.5, 3, 6, 9$  and 12 ppm) relative to xenon in water. Additional three offsets were used as dummies at the beginning of each spectrum to stabilize the gas delivery. Fig. 3.10 shows the z-spectra from a data set acquired using CAVKA-4 with 9 averages of the reference image (blue) compared to a fully sampled and 9-times averaged data set (orange). The inlay visualizes the corresponding acquisition times of 21 min and 149 min for the CAVKA-4 and the fully sampled and averaged acquisition, respectively. The nature of hyperpolarized nuclei demands their re-delivery for each image in the series and therefore not only for the different offsets, but also for each averaging replicate acquisition. This is due to the fact that the non-equilibrium magnetization is used up after each acquisition. Consequently, the CAVKA approach of acquiring one averaged reference image and (partially) reusing it for the entire image series reduces the number of gas deliveries from 315 to 44 and thus the acquisition time by  $\sim 86\%$ . The z-spectra in Fig. 3.10 show excellent agreement between conventional (fully sampled and averaged) and CAVKA-based acquisitions and thus demonstrate the potential of the proposed CAVKA method to accelerate the acquisition of imaging series (like in CEST MRI) without sacrificing image or data quality.

The reduction of the image acquisition time by CAVKA relative to conventional acquisition with signal averaging was calculated (see section 3.2) as  $NA \cdot N_\omega \cdot R / (R \cdot NA + N_\omega)$ . This acceleration depends on three variables:  $N_\omega$  - the series length,  $NA$  - the number of averages and  $R$  - the undersampling factor. This term holds for acquisitions which include a magnetization encoding block only. When a magnetization preparation block is also a part of the acquisition (e.g., CEST), or when hyperpolarized nuclei are delivered with a certain delivery time, or when both are included (e.g., HyperCEST) the acceleration term reduces to  $NA \cdot N_\omega / (NA + N_\omega)$ . In this case, the  $R$  dependency becomes negligible because  $TR$  is much shorter than the delivery time

and/or the preparation time. These slow steps before the encoding of each averaging acquisition (for each image in the series), make the number of averages and the length of the image series the dominant terms for the acceleration factor.

This acceleration capability addresses the unfavorable combination of time-consuming steps that is beyond the scope of other undersampling approaches such as compressed sensing [16], deep learning [28] and parallel imaging [29]. These assume the phase encoding steps to be the most time-consuming element and target on reducing their number by subsampling. However, a reduced number of phase encodes would not lead to a meaningful acceleration when a fixed time of HP media delivery and/or magnetization preparation is needed before the readout. When time-consuming pre-encoding steps are needed in each averaging acquisition, only a reduction of averaging steps by reusing a reference image to share data along the imaging series dimension provides the desired acceleration. Similarly to the imaging methods of parallel imaging, CAVKA is a technique that can be used to process undersampled data from different types of pulse sequences. However, the two methods pursue different acceleration approaches and differ by the hardware requirements, namely the multichannel receiver array that is needed in parallel imaging. Other keyhole works have recently been published [38, 39]. They show the relevance of the keyhole method in relatively new applications.

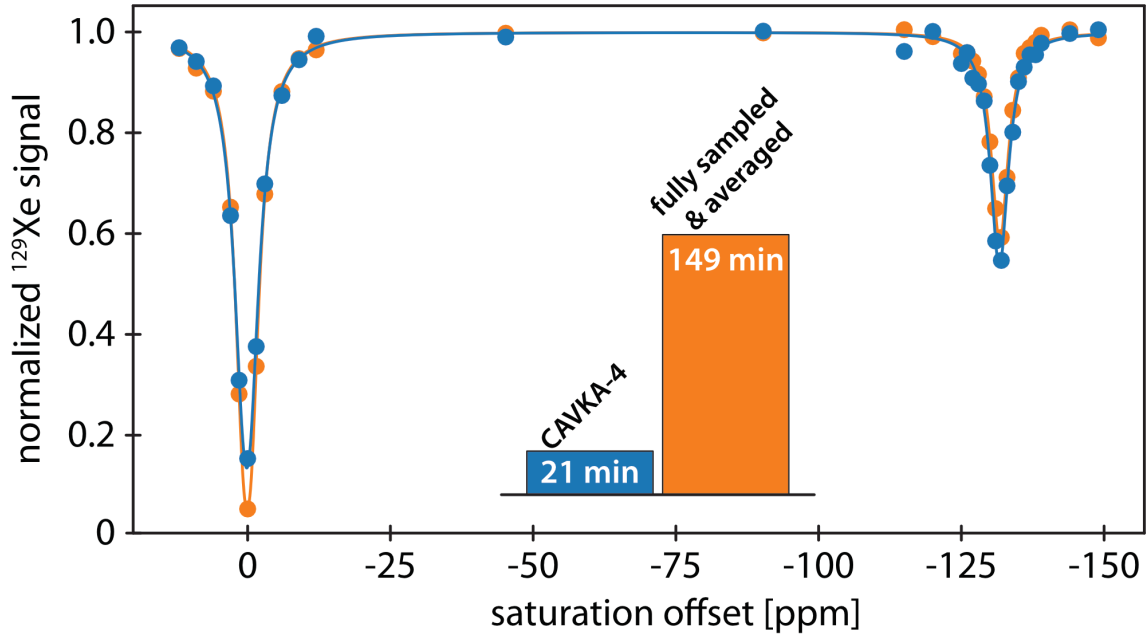


Figure 3.10: HyperCEST z-spectra of CrA acquired by CAVKA-4 method and by conventional imaging with averaging. Data points represent ROI-averaged and normalized signal intensities. The almost complete overlap of the spectra shows the reliability of the CAVKA method and yet with a 7-fold reduction of the acquisition time.

#### 3.4.4 CAVKA simulations for identifying limitations

The utilized digital phantom (size  $256 \times 256$ ) comprises four compartments. Signal intensities of a z-spectrum were assigned to each pixel in the different compartments. These z-spectra (41 offsets between 100 ppm and 140 ppm) are based on numerical simulations following the Bloch-McConnell (BMC) equations for two pools (bulk and CEST). The outer compartment (Comp. 1) remains constant (non-CEST responsive) and the other compartments were carefully designed to provide different combinations of on-resonant and off-resonant contrast: compartments 2 and 3 have the same on-resonant contrast (response at 120 ppm saturation offset), but unlike compartment 2, compartment 3 does not have off-resonant contrast (RF saturation at the offsets 100/140 ppm) at all. Compartment 4 has an on- and off-resonant contrast, however, both are lower compared to compartment 2. These differences in on- and off-resonant contrasts were chosen to test the performance of CAVKA under different scenarios

and were realized by adjusting the relative pool size fractions of the CEST pool to 0.4%, 0.5% and 0.1% for compartments 2, 3 and 4, respectively. Additionally, the corresponding pool sizes of the bulk pool were set to 0.8, 1 and 0.9 (the sum of both pools does not have to be 1). Other simulation parameters appeared in Table 3.1.

CAVKA images were reconstructed for undersampling factors  $R = 2, 4, 8, 16, 32,$  and 64. For the reference image, 16 averages were used. The averaging was mimicked in a three-step process (as explained in section 3.3) to respect the different noise conditions between the keyhole and the periphery. Keyholes were created using the fully-sized k-space, which was multiplied by  $\sqrt{R}$  according to Eq. 3.5 to simulate the VFA signal enhancement, followed by the addition of noise and finally cutting out the center according to the value of  $R$ . The order of operations here is important, noise must be added only after multiplication by  $R$  to avoid amplification of the noise since only the signal is amplified in real acquisition with VFA while the noise has roughly a constant value. Hybrid k-space data were constructed in the same way as with the experimental data.

The keyhole method is prone to loss of image details when excessive undersampling is applied. The influence of reusing high frequency information from the reference image in order to retrieve missing data in a dynamic contrast imaging series was thus investigated for a Shepp-Logan style phantom that has a more complex geometry than the two-compartment phantom. Fig. 3.11 compares between a CAVKA-16 image (created with a reference image of 16 averages) and a fully sampled image simulated to be acquired with the same number of averages.  $R = 16$  is a more extreme application of the method than in our experimental data to validate the robustness of CAVKA. This comparison is done for the off-resonant and on-resonant (120 ppm) cases. Whereas the off-resonant CAVKA image shows no artefacts at all (Fig. 3.11 bottom left), the on-resonant one exhibits artefacts in the form of blurred edges of the inner compartments (Fig. 3.11 bottom right). These kind of artefacts in the vicinity of edges are associated with inaccuracies in the high frequency information of the frequency domain (before the Fourier transformation) and are known to appear from other works in the field of image compression [40, 41].

To investigate these artefacts as a function of the undersampling factor, error maps

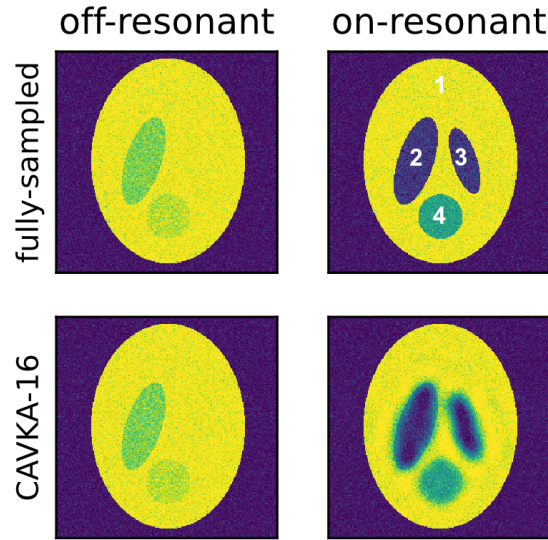


Figure 3.11: CAVKA reconstructions in digital phantom. Off- and on-resonant CEST images illustrating artefacts in CAVKA images. Off-resonant images retain sharp edges, on-resonant images experience blurring for the edges of the CEST-responsive areas. CAVKA images were created with a reference image of 16 averages and were normalized (divided by  $\sqrt{R}$ ) to allow comparison to the fully-sampled images.

for undersampling factors between 2 and 64 were calculated. These maps, presented in Fig. 3.12, show the pixel-wise deviations of the on-resonant CAVKA images from the simulated BMC-based images without noise. As expected, the errors increase with increasing undersampling factors and are most pronounced for compartment 3, which does not have any off-resonance contrast and is thus the most challenging one for the CAVKA method. However, up to an undersampling factor of 16, the errors are restricted to the edges of the compartments. For higher  $R$ -values, distortions start to appear and the errors are not limited to the edges of the compartments anymore. The overall increased errors in the CAVKA-2 error map are the result of high noise values in the relatively large (non-averaged) keyhole region when a small undersampling factor is chosen.

The influence of these distortions was further investigated on ROI-based  $z$ -spectra for  $R = 16$  and 16 averages of the reference image. Fig. 3.13 shows the ROI-averaged  $z$ -spectra of compartments 2 (blue), 3 (orange) and 4 (green). The dashed

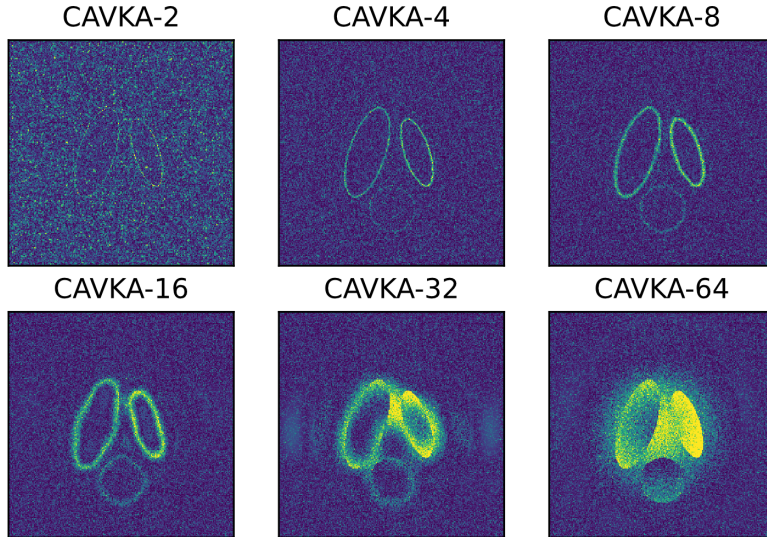


Figure 3.12: Error maps for CAVKA images with undersampling factors 2 – 64. The error maps were calculated by subtracting CAVKA images from noise-free BMC-based images followed by normalization (division by  $\sqrt{R}$ ). Up till  $R = 16$  errors are restricted to the edges of the compartments.

lines correspond to the CAVKA data, the solid lines to the simulated BMC data and the dashed-dotted lines to their difference. Despite including pixels close to the compartments edges (ROIs were identical to the compartments shapes), differences in the spectra occur only at the on-resonant frequency. In agreement with the error maps shown in Fig. 3.12, the largest deviations are observed for compartment 3.

The geometry of the digital phantom was chosen to be more complex than the experimental phantom. The limit for the keyhole size for such synthetic data was found to be around  $16 \times 16$ . However, this corresponds to an undersampling factor of  $R = 16$  and shows that the maximal achievable undersampling factor highly depends on the geometry of the measured object and the matrix size of the reference image. In general, objects with complex geometry or contrast pattern demand for larger keyhole matrix sizes. Furthermore, the simulations revealed that the difference in contrast between the reference image and the keyhole image is a crucial point for the CAVKA approach that should be considered when adjusting the undersampling factor for a specific scenario.

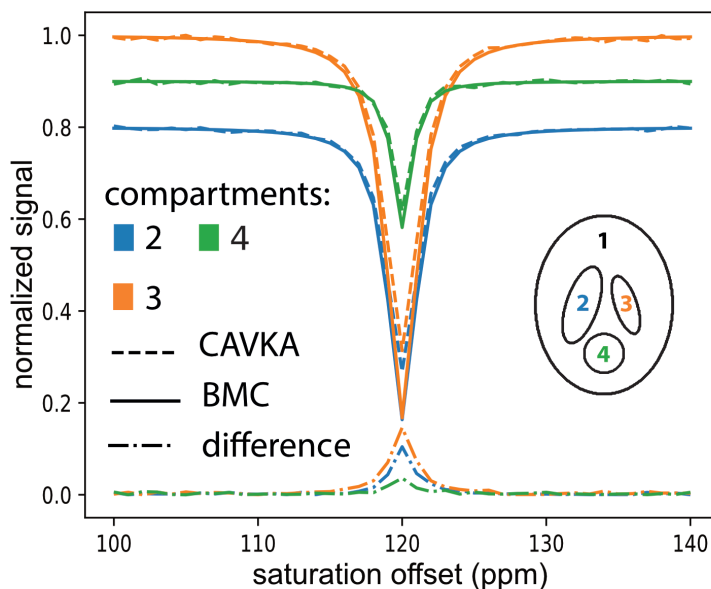


Figure 3.13: CEST compartments and CEST spectra derived from the respective ROIs in the CAVKA-16-reconstructed images (using 16 averages for the reference image) and from BMC-simulated reference spectra.

Simulation also allowed to have a comparative view on CAVKA hybrid k-spaces that are created from different combinations of keyhole sizes and number of averages for the reference image. Fig. 3.14 presents a comparison between sixteen hybrid k-spaces formed by combining four keyhole sizes correspond to  $R = 1, 2, 4$  and  $8$  (when the fully sampled image has a resolution of  $256 \times 256$ ) and four averaged reference images made from averaging  $1, 2, 4$  and  $8$  replicates of the reference image. In the hybrid k-space that merges a keyhole domain with  $R = 2$  (size  $128 \times 128$ ) and a reference image of  $1$  average (non-averaged), which appears in the top row and the second column, the keyhole domain can be distinct from the the periphery by showing a relative low noise level. The noise added to the keyholes and reference images had the same standard deviation, however, the scaling of the reference image in the form of multiplying it by  $\sqrt{2}$  leads to an increase of the noise level (as a side effect to the increase of the signal level which is the purpose of this scaling). We can thus see a somewhat noisier periphery in the hybrid data. Staying with the same undersampling factor and moving down along the second column to the third row,

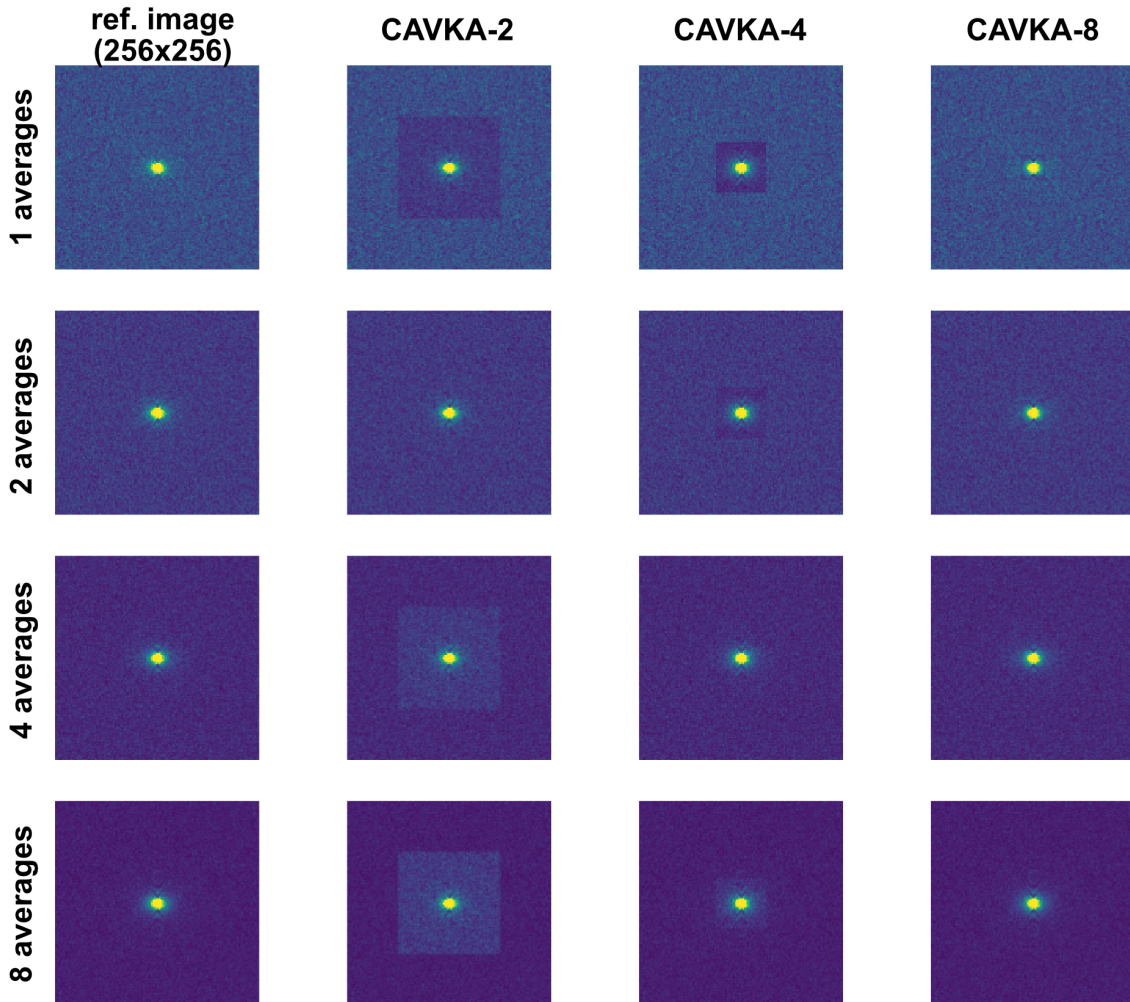


Figure 3.14: CAVKA hybrid k-spaces. When undersampling factors exceed the number of averages (above the diagonal) the noise level in the periphery is higher than in the keyhole. When undersampling factors are lower than the number of averages (below the diagonal) the noise level in the periphery is lower than in the keyhole. Color maps were set with an upper limit that is 2% of the maximal pixel value in each sub-figure to allow a view on both the keyhole and periphery domains.

where the reference image had 4 averages, we can still identify the keyhole domain but this time it has a higher noise level relative to the periphery. As before, the reference image was multiplied by  $\sqrt{2}$ , however, the noise level in this reference image had been already reduced by a factor of  $\sqrt{4}$  due to averaging of 4 replicates. The combined effect (averaging and scaling) yields a reduction by  $\sqrt{2}$  in the noise level. In the first case, the undersampling factor (2) was higher than the number of averages (1) and then the periphery was noisier compared with the keyhole domain. In the second case, the undersampling factor (2) was lower than the number of averages (4) and then the periphery showed a reduced noise level compared with the keyhole domain. This insight holds for other combinations of keyhole sizes and number of averages which appear in Fig. 3.14, yet for the most right column (CAVKA-8) the keyhole domain is too small to be seen clearly. Along the diagonal in Fig. 3.14 appear hybrid k-spaces where the undersampling factors equal the number of averages. In this case the noise level in the keyhole domain and the periphery is the same (the keyhole domain cannot be distinct). Along the diagonal and below it (where the number of averages exceed the undersampling factors) image reconstructions would have reduced noise level and thus better image quality and are the preferred combinations when using the CAVKA method. However, choosing the number of averages for experimental applications should be adjusted to have a sufficient image quality while still keeping the acquisition time reasonable.

Analysis of the error in CAVKA images when changing not only the undersampling factor (as in Fig. 3.12) but also the number of averages of the reference image is too complicated to be done by comparison of images. To allow this kind of analysis, one number is extracted from each image to describe the error which is the mean absolute error (MAE). It is calculated by the absolute value of pixel-wise subtractions (magnitude values) of a CAVKA image from the fully-sampled image with the matching number of averages and followed by averaging of all pixel values. This is done

separately for on- and off-resonant offsets. The exact term of the MAE parameter:

$$\begin{aligned} \text{MAE}^{\text{off}} &= \frac{1}{d} \sum_{n=1}^d ||I^{\text{off}}(n)| - |I_0^{\text{off}}(n)|| \\ \text{MAE}^{\text{on}} &= \frac{1}{d} \sum_{n=1}^d ||I^{\text{on}}(n)| - |I_0^{\text{on}}(n)|| \end{aligned} \quad (3.7)$$

$I^{\text{off}}(n)$  is an off-resonant CAVKA image and  $I_0^{\text{off}}(n)$  is fully-sampled (conventional) off-resonant image with the matching number of averages (which is also the reference image).  $n$  is the pixel index,  $n = 1, 2, \dots, d$ ,  $d = 256 \times 256$  is the image resolution.  $I^{\text{on}}$  and  $I_0^{\text{on}}$  are the on-resonant CAVKA and fully-sampled images, respectively. MAE is calculated for different combinations of number of averages ( $N$ ) and undersampling factors ( $R$ ), by repeating the calculation in Eq. 3.7 for CAVKA images  $I(R, N)$ ,  $R \in \{2, 4, 8, 16\}$ ,  $N \in \{1, 4, 8, 16\}$  (in words, CAVKA images which composed from a reference image with  $N$  averages and a keyhole size that corresponds to  $R$ ) and for reference images  $I_0(N)$ . CAVKA images possess an intrinsic signal increase when compared with the reference (conventional) image. This makes the calculation of a relative error (percentage deviation), like the one done in section 2.2.1, inaccurate. In order to omit the contribution of the signal increase from the error value, all images are normalized to have a maximal signal value of 1 (by dividing each image by its maximal pixel value) before they are used for the MAE calculation. MAE uses absolute values of the pixel-wise errors which prevents reducing the accumulated error due to a change of the error sign (positive/negative) upon averaging. Fig. 3.15 provides the analysis results.

Plotting the MAE vs. the undersampling factor for different number of averages of the reference image and only for the off-resonant offset (Fig. 3.15a) shows that the MAE decreases as  $R$  increases for all number of averages used. This reduction in MAE is the result of the increase in the periphery size when  $R$  increases. For high  $R$ , data is duplicated (signal and noise) from the fully-sampled image that it is compared with for the error estimation. One might expect that the MAE would increase with increasing  $R$  values because of the signal increase in CAVKA images with higher  $R$  values. However, this effect is abolished by the normalization of the images. The

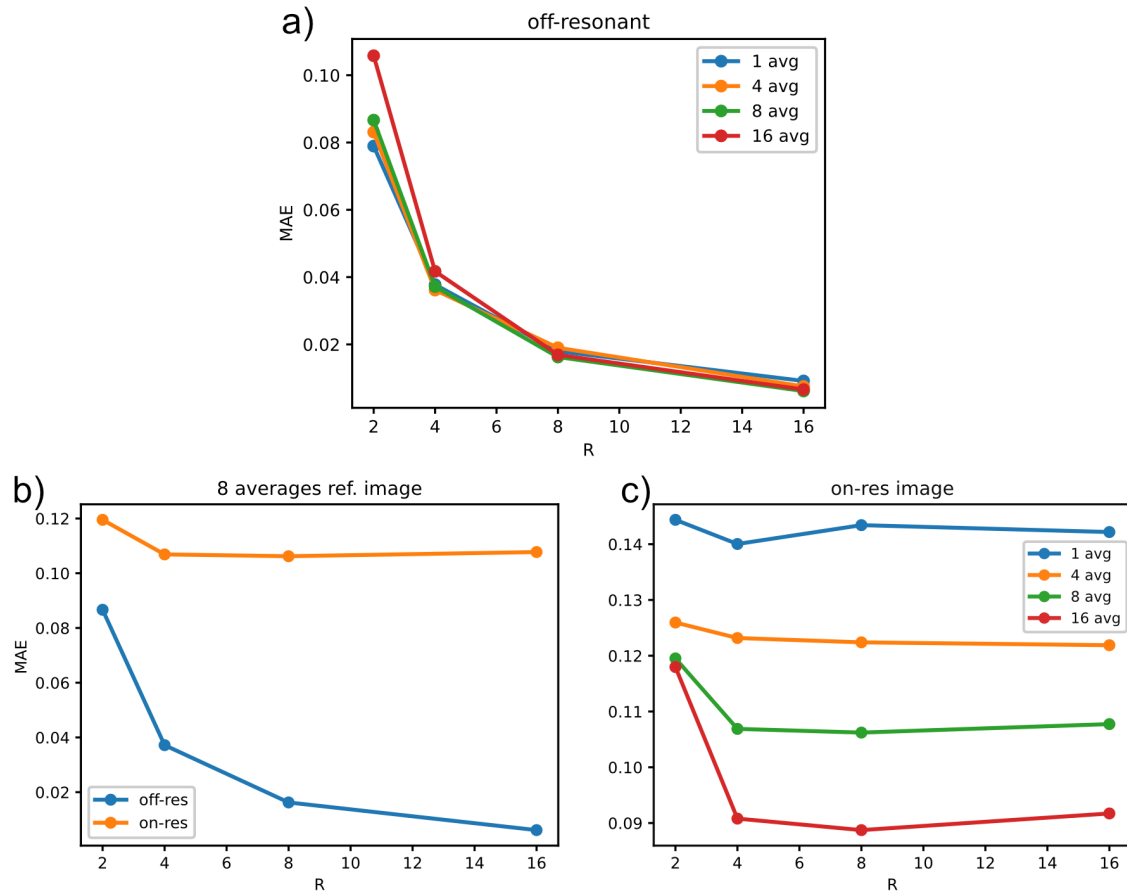


Figure 3.15: Mean absolute error (MAE) in on- and off-resonant CAVKA images composed of combinations of four sizes of the keyhole domain and four numbers of averages to denoise the periphery domain. a) Off-resonant case, decreasing MAE with smaller keyholes. b) On- and off-resonant comparison for one instance of averages (8): higher MAE for the on-resonant case that stabilizes at  $R = 4$ . c) On-resonant case, decreasing MAE with the reduction of noise (higher number of averages), yet with the same trend along the  $R$  axis. MAE was calculated from images that were scaled to have a maximal signal of 1 to allow comparison.

difference in MAE values for the different curves when  $R < 4$  could be explained by the noise difference in the relative large keyhole domain (for these  $R$  values), which is higher for 16 averages (red curve) relative to the other curves. Fig. 3.15b compares the MAE vs.  $R$  between on- and off-resonant offset just for one number of averages (8) of the reference image. It displays a higher MAE for the on-resonant offsets for all  $R$  values. Additionally, the MAE for the on-resonant offset stops decreasing at  $R = 4$ . The reason for the higher error in the on-resonant case is the difference between the noise sets used in the reference image (which is the source for data retrieved in the periphery of a CAVKA image) and in the on-resonant fully-sampled image (that is used to calculate MAE). In other words, in the on-resonant offset there is not a duplication of the noise between the CAVKA image and the comparison image. This lack of duplication is also the explanation for the stop of the decrease in MAE at  $R = 4$ . For  $R \geq 4$ , the error is dominated by the different patterns of the periphery domains (off-resonant pattern in the CAVKA image and on-resonant pattern in the comparison image). The error stays constant for  $R > 4$  due to averaging (more pixels are included with the same error). For  $R < 4$  the error is dominated by the difference in noise levels upon comparison of averaged/non-averaged data in the keyhole domain. In Fig. 3.15c, a comparison of the MAE for combinations of the tested  $R$  and  $N$  values just for the on-resonant offset is shown. The trend of each graph (with different color) is the same as for the orange graph in Fig. 3.15b and was already explained. The decreasing MAE level (for all  $R$  values) for each graph when increasing  $N$  comes from lower noise level in both the CAVKA and the comparison images.

From this analysis it can be concluded that the accuracy of CAVKA images improves upon the use of more averages. The limitation for the number of averages to use comes from the practical reason of how much time could be spent for acquiring the averaged reference image. In contrary, the undersampling factor has only a limited influence on the accuracy of the CAVKA images and in a positive way, i.e., higher undersampling (with the resulting signal increase) beyond a certain point comes without paying a higher price in MAE. However, the critical point of MAE stabilization (here  $R = 4$ ) depends on the noise level and the contrast pattern, i.e., differences between the on- and off- resonant images. Additionally, the accuracy of CAVKA images must

be studied with error maps (see Fig. 3.12) to get a better understanding of how the error is distributed in the image and to check if the quality of some of the image features is satisfying.

## 4 Imaging of hosts with fast Xe exchange

In this relative short chapter the CAVKA method is tested for acquiring MRI with a sample containing gas vesicles.

### 4.1 Challenges of multivalent xenon hosts

The search for highly efficient HyperCEST agents fostered the investigation of hollow protein structures that binds many Xe atoms for fast saturation transfer. Gas vesicles (GVs) are such a new class of contrast agents for MRI of hyperpolarised Xe. They are a natural bacterial product expressed to achieve buoyancy [42, 43] and comprise a closed and hollow protein structure that is permeable to gas exchange with the surrounding environment. For their use as MRI (or ultrasound) reporters, the GV were expressed in bacteria [44] and their names are related to the type of bacteria they originate from: Ana for GV expressed in *Anabaena flos-aquae* and Mega for the ones expressed in *Bacillus megaterium*. Ana and Mega GV have a similar shape, i.e., a cylindrical tube closed by conical end caps [43], but they are different in size with 520, 250 nm in length and 140, 70 nm width, respectively [45]. To maintain their gas binding ability and prevent a collapse of the physical structure, exceeding the pressure range of 2 – 6 bar is prohibited [43].

Although GV differ from the more common chemically synthesized Xe hosts (like cryptophane and cucurbit[ $n$ ]uril families) their principle of contrast mechanism is the same and is based on a selective RF pulse that saturates  $^{129}\text{Xe}$  magnetization only for atoms that are inside the host. However, the GV have a higher volume that can enclose much more Xe atoms than the chemically synthesized hosts. This makes them efficient CEST contrast agents since during saturation, a higher number of xenon atoms are depolarised for causing a stronger CEST response. Another reason for this efficiency is their loading capacity (of xenon atoms) that is based on physical partitioning of dissolved gas following the ideal gas law rather than on the chemical affinity of xenon to its host [45].

However, efficiency as CEST contrast agents also leads to shortened  $T_2$  which can also be described as accelerated loss of spin phase coherence. It stems from

the chemical exchange of the spins in and out of the hosts and the related frequent but stochastic hopping between two Larmor frequencies that cause fast dephasing. Moreover, magnetic gradients induced by gas-filled hosts in a liquied solution [46] cause further relaxation of the transverse magnetization.

Shortened  $T_2$  manifests as low SNR in imaging acquisitions of GVs samples. It actually prevents the use of spin-echo techniques that rely on long echo times. Fast  $T_2$  decay cause blurring that hampers signal extraction from the phantom compartments and make other CEST effect quantifications, that are based on the signal difference between the two compartments, impossible [47, 48]. These types of Xe hosts require novel acquisition strategies tailored to fast  $T_2$  decay and a low starting magnetization to increase the SNR.

Understanding the mechanism of averaging that brings an increase in SNR is also important. Applying averaging in a wrong way, for example, by averaging of magnitude pixel data instead of the complex-valued pixel data, would not provide the expected denoising effect. Noise in magnitude data is Rician distributed. Rician distribution is SNR dependent: when the SNR is low it is a Rayleigh distribution and when the SNR is high it is a normal distribution [34, 49]. Additionally, Rician noise has a non-zero mean which at low SNR regimes makes the signal biased (shifted away from its true value). This makes some areas of the double phantom image (those with low SNR) to appear more noise-corrupted than with averaging of the complex-valued (normally distributed) noise. Moreover, the biased signal masks the expected trend regarding the noise level in averaged images.

In the following chapter, the CAVKA method was applied for MRI of GVs. It includes testing for the SNR in GVs images and for the number of averages needed to improve it, then analysis of averaging with magnitude pixel data is performed in order to explain its failure in denoising the images. Finally, CAVKA images were created and showed the potential of the method in accelerating acquisition tailored for a shortened  $T_2$ .

## 4.2 Results and discussion

In the following subsections, the results from double phantom experiments are presented, which contained H<sub>2</sub>O in the outer compartment and gas vesicles (GVs) of the Ana type (70 pM in dPBS) in the inner compartment. GV samples were provided by Mikhail Shapiro from the California Institute of Technology. Scans were performed using a modified 2D FLASH sequence that includes a preceding CEST preparation block and a VFA scheme for the excitation pulses. Saturation pulses of 10 s duration and 20  $\mu$ T amplitude were applied with frequency offsets of 361.5 ppm and -176 ppm for the off- and on-resonant cases, respectively. <sup>129</sup>Xe imaging parameters were:  $TE = 3.8$  ms,  $TR = 8.6$  ms,  $FOV = 10 \times 10$  mm<sup>2</sup>, slice thickness = 20 mm,  $BW = 5$  kHz, encoding order = "centric", matrix (image resolution) =  $32 \times 32$ . The keyhole was realized by changing the phase encoding interpolation parameter to 4 (matrix =  $32 \times 8$ ), followed by trimming the rectangular matrix to a  $8 \times 8$  square matrix. Reduced flow of 70 ml/min and reduced overpressure of 1.5 bar were used to prevent collapsing of the GV. The xenon fraction was 5% of the gas mixture (with helium and nitrogen) being delivered to the sample. Bubbling was performed for 25 s and additional 3 s were added afterwards for allowing potentially generated gas bubbles to collapse. Averaging was done separately (outside ParaVision) on complex-valued raw data in Python. SNR in images was calculated by defining signal and noise ROIs, then taking the average of pixels inside the signal ROI and divide it by the standard deviation of pixels inside the noise ROI.

### 4.2.1 Signal averaging for the reference image

A low SNR was expected in the GV acquisition, however, as with new samples, it was not clear beforehand how low the SNR would be. Thus, an imaging series with 20 elements was acquired for adjustable retrospective signal averaging (all on the same off-resonant frequency). Next, averaged images with a different number of averaging replicates were generated as shown in Fig. 4.1. The improved visual quality can be spotted; whereas only noise is displayed without averaging, 9 and 16 averages allow the visualization of the phantom geometry. The 16 averages image shows reduced

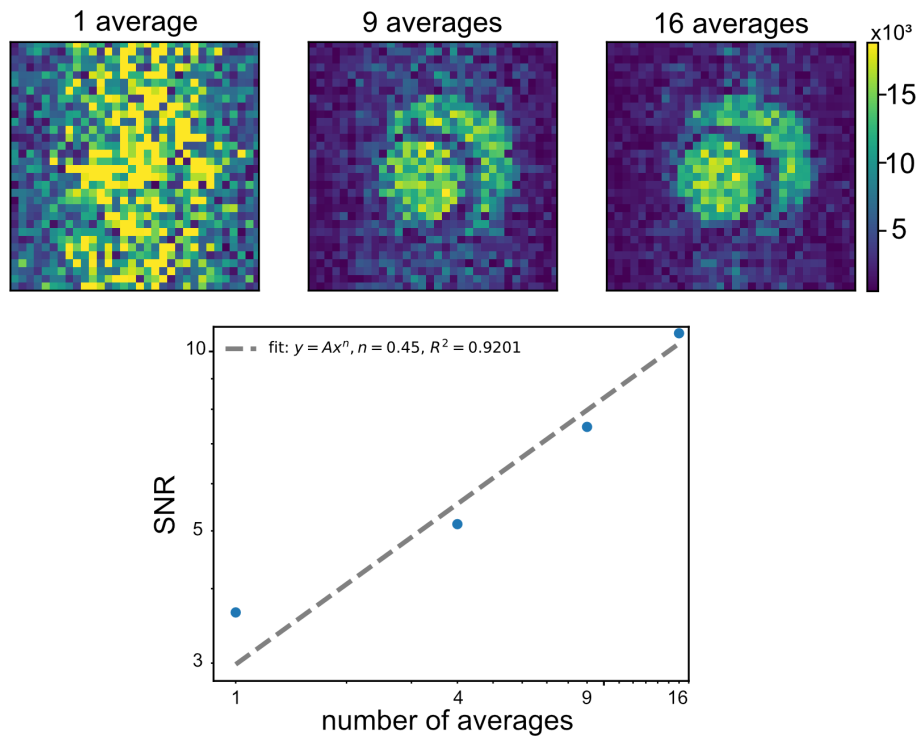


Figure 4.1: Testing the number of averages required for the reference image with the GVs sample. Top: Averaged reference images constructed with an increasing number of averages. Imaging without averaging (left) of the GVs sample with short  $T_2$  displays only noise. Bottom: SNR in the images (on top) vs. the number of averages. The expected trend (as a squared root function) is validated by curve fitting; the output slope is  $n = 0.45$ . Plotting is with logarithmic axes.

noise level in the area around the phantom compared to the 9 averages image, but it is clear that the visual quality is already sufficient with 9 averages for defining the signal ROI. Despite this sufficient quality, the 16 averages image was used as a reference image for the CAVKA reconstruction (in section 4.2.3) since the longer time for its acquisition was already invested and it provides, as shown in Fig. 4.1, a higher SNR and visual quality.

To further analyze the SNR in averaged images, a plot of SNR vs. the number of averages was drawn using four numbers of averages of 1, 4, 9 and 16, as shown in Fig. 4.1. Data was plotted using a logarithmic scale for the x- and y-axis and the data was fitted to a model function of the form  $y(x) = Ax^n$ , SNR should theoretically present a square root dependency on the number of averages. This expectation was tested then by checking how close the fit result for  $n$  is to 0.5. A reasonable value of  $n = 0.45$  was the result of the fitting procedure. The goodness of the chosen model to the experimental data is given by  $R^2 = 92\%$ . Random selection was used for choosing the individual averaging replicates (out of the 20 that were available) for each averaged image.

#### 4.2.2 Analysis of magnitude data averaging

For the sake of illustration, an averaged reference image was created by averaging the magnitudes of the averaging replicates instead of the complex-valued images. Fig. 4.2 presents these images. It is clearly seen that this kind of averaging process for low SNR raw data did not provide the expected improvement in visual quality as in Fig. 4.1. Direct comparison to the images in Fig. 4.1 helps in recognizing the phantom, but without this comparison the phantom would not be so easily recognizable. One can also see a high noise level in the area outside the phantom, increasing the number of averages does not seem to denoise this area as expected.

The explanation to these observations is related to the noise properties in complex and magnitude image data. Whereas noise in complex image data is normally distributed with zero mean (in each of its real/imaginary components), the noise in magnitude image data is Rice distributed with a non-zero mean [34] (simply because magnitudes are non-negative and thus the random noise is distributed around a pos-

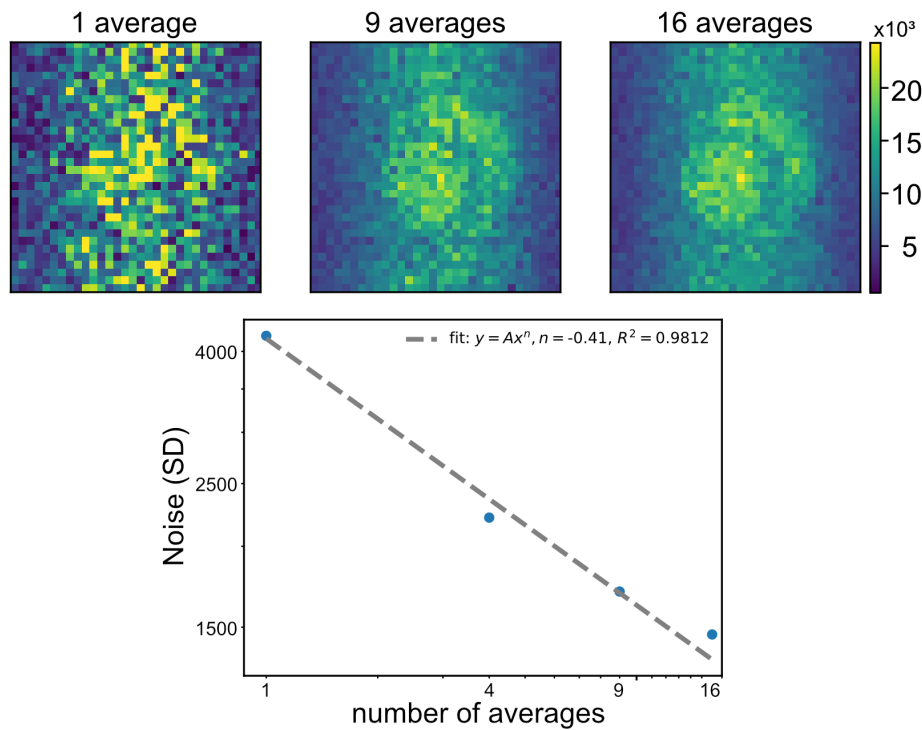


Figure 4.2: Magnitude-averaged reference images fail to provide a sufficient denoising effect. Top: The resulted images of magnitude averaging from 1, 9 and 16 replicates show non-zero mean noise. Bottom: Noise standard deviation (SD) in the images (on top) vs. the number of averages. Noise reduction is confirmed as expected according to Eq. 3.2, however the non-zero mean noise prevents observing this reduction. Plotting is with logarithmic axes. Noise ROI as shown in Fig. 3.9 in section 3.4.2.

itive number). Averaging of multiple complex noise data sets keeps the noise mean at zero and thus the noise level as seen at the area outside the phantom (Fig. 4.1) is relatively low. Averaging of magnitude images, with their non-zero mean noise, results with a non-zero mean noise in the averaged image and thus the area outside the phantom (Fig. 4.2) appears noisier.

Increasing the number of averages reduces the noise SD in the same amount for Rice distributed noise as for normally distributed noise, since the derivation appeared in Eq. 3.2 in section 3.1.2 is invariant to the type of noise distribution. Yet, in the magnitude images this effect is not easily seen. To verify that the noise SD is indeed reduced as expected when increasing the number of averages, the two are plotted against each other and displayed in Fig. 4.2. This confirms the expected noise behavior. Additionally, Eq. 3.2 predicts a reduction of the noise SD when increasing the number of averages according to the function  $y(x) = Ax^{-1/2}$ . By the same curve fitting procedure described in the previous section, the expected trend could be verified by showing a fit output  $n = -0.41$ , presented in Fig. 4.2. The reason for not observing this confirmed reduction in the noise level is the non-zero mean noise. It manifests a higher value than the noise SD and thus prevents the visualization of the noise reduction.

### 4.2.3 CAVKA imaging - Proof of principle

The GVs sample with shortened  $T_2$  provided the first real test to the CAVKA method. During development of the method, experimental studies had been conducted with the well investigated Xe host CrA. However, the conditions with CrA provided sufficient SNR and image quality in the conventional acquisition that it only marginally benefited from the expected CAVKA improvements. In contrast, the conventional acquisition with a GVs sample showed a very low SNR (and image quality) as can be seen in Fig. 4.3 (top row). In this case, the CAVKA acquisition does not only provide a nice-to-have SNR increase rather turns totally noisy and blurred images into ones that display the imaged object properly (Fig. 4.3, bottom row). Table 4.1 provides the SNR values for the off-resonant images (left column) in Fig. 4.3 and also for the same images with CrA as the Xe host (values from experiments conducted in section

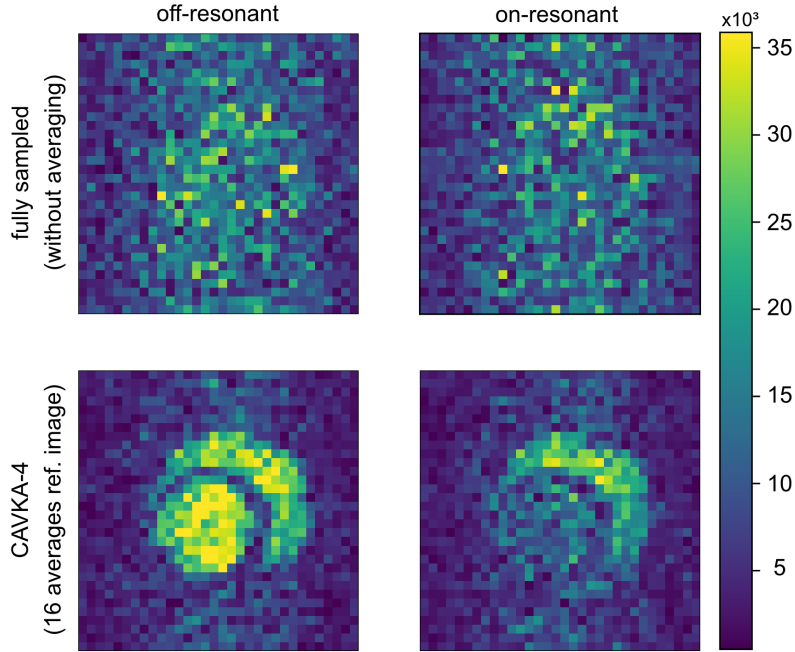


Figure 4.3: CAVKA images of a GV sample. Off- and on- resonant images (left and right) display the expected saturation of  $^{129}\text{Xe}$  magnetization in the inner compartment that contains the GVs. Improved imaging quality with the CAVKA acquisition (bottom) vs. simple VFA acquisition (top).  $^{129}\text{Xe}$  MRI of phantom with 70 pM GVs (Ana) in the inner compartment and  $\text{H}_2\text{O}$  in the outer compartment.

3.4.2). The SNR with the GVs sample in a VFA acquisition without averaging is 3-fold lower than with the CrA sample.

CAVKA was used to acquire an imaging series of 2 images (on- and off-resonant) which provided a 1.78-fold acceleration (using the formula developed in section 3.2.1) compared with acquiring 16 averages for each of the two images in a double phantom experiment. This acceleration factor reduced the acquisition time from  $\sim 26$  min to  $\sim 15$  min. This degree of acceleration is not very high due to the short length of the imaging series. However, with an acquisition of the full HyperCEST spectrum this acceleration factor would be much higher (see section 5).

The reason for a lower SNR in the GVs imaging acquisition is the shortened  $T_2$  of  $^{129}\text{Xe}$  undergoing fast exchange with the GVs core. This has two reasons:

1. Efficient exchange with frequent large frequency jumps. The exchange rate comprises the rate of Xe going into the host and the rate of Xe coming out of the

Table 4.1: SNR comparison between GVs and CrA (double phantom) images without saturation (at an off-resonant saturation frequency) in conventional (VFA) acquisition and CAVKA-4 acquisition.

	GVs	CrA
Fully sampled (without averaging)	3.65	11
CAVKA-4 (16 averages ref. image)	10.75	40

host. The rate of going into the host is slower (due to the dominant pool of unbound Xe) and thus it is the limiting factor. For GVs this rate is  $13.3 \text{ s}^{-1}$  [45] whereas for CrA is only  $0.3 \text{ s}^{-1}$  [50], as quantified by the qHyperCEST method (under steady state assumption, i.e., the exchange rate of going into the host is the product of the exchange rate of coming out of the host and the fraction of bound Xe). In [45] 38 pM Ana GVs was used while in this work 70 pM was used and since the exchange rate increases linearly with the host concentration (as long as it is not limited by the Xe concentration) it has a value of  $24.7 \text{ s}^{-1}$ .  $R_2$  ( $1/T_2$ ) of Xe in pure water (without a host molecule) is  $3.1 \text{ s}^{-1}$  according to [51]. Thus, exchange reflects a 8-fold higher contribution in the 70 pM GVs sample. However, it is limited to large frequency jumps that dephase the spins.

2. Magnetic susceptibility difference between the gas phase inside the GVs and the liquid phase of the solution. This close proximity of gas filled space in the GVs core and surrounding liquid imposes strong magnetic field gradients on spins exchanging in and out of the gas vesicles as reported in [46]. Although quantification of this effect has been done for the Mega types GVs, it is qualitatively also applies for the Ana type GVs under the assumption that they have similar shapes. A  $T_2$  measurement from 670 pM Mega GVs yielded  $T_2 = 2.2 \text{ ms}$  ( $R_2 = 455 \text{ s}^{-1}$ ) while the exchange-induced decay rate was only  $18.3 \text{ s}^{-1}$ . Thus, a far bigger contribution in addition to the exchange was demonstrated, which was attributed to the magnetic susceptibility difference.

An additional reason for the reduced SNR in GVs imaging is the lower  $^{129}\text{Xe}$  concentration. The GVs must be handled with care to prevent their collapse, thus

the total pressure condition under which the sample is measured had to be adjusted to 1.5 bar (instead of the usual 4.5 bar). This 3-fold pressure reduction has a direct influence on the concentration of  $^{129}\text{Xe}$  in solution, which then also decreases 3-fold to  $\sim 86 \mu\text{M}$  according to  $[\text{Xe}] = (\Gamma \cdot \rho \cdot X_{\text{e}_{\text{pc}}}) / 0.0254 \text{ L/mM}$ , where  $\Gamma$  is the Ostwald solubility constant for Xe in water (temperature dependent) at room temperature  $\Gamma = 0.11 \text{ L/atm}$  [52].  $\rho$  is the total pressure (1.5 bar) and  $X_{\text{e}_{\text{pc}}} = 5\%$  is the Xe percentage in the gas mix. This yields  $[\text{Xe}] = 325 \mu\text{M}$ . However, only  $^{129}\text{Xe}$  provides signal (with natural abundance of 26.4%), thus the concentration is  $86 \mu\text{M}$ .

## 5 Spectroscopy of host-guest system with competitive binding

In this chapter the aim is to study the exchange kinetic of cucurbit[7]uril (CB7) and cucurbit[6]uril (CB6) as molecular hosts and of xenon as a guest in the presence of different competitive guests by imaging-based HyperCEST spectroscopy.

### 5.1 Introduction

The cucurbit[ $n$ ]urils (CB $n$ ) are a family of macrocycles that come in different sizes according to their number  $n$  of repeating subunits of glycoluril ( $C_4H_6N_4O_2$ ), see Fig. 5.1. They have been used in a variety of applications [53–57] from stabilization of dye assays to being carriers in drug delivery. Their synthesis is done by acid-catalyzed condensation of glycoluril and formaldehyde. The purification of a single CB $n$  can introduce impurities e.g., acetone and methanol. Additionally, CB6 is a known side product in the synthesis of CB7 [58]. Separation and identification of these CB6 by-products is challenging. However, the cavity size of different CB $n$  affects their supramolecular binding affinity to guests of different sizes. This can be used to analyze CB7 sample for CB6 impurities more sensitively than with other approaches like direct NMR spectroscopy of CB6/7

For example, the guest *cis*-1,4-bis(aminomethyl)cyclohexane (will be referred to as the blocker or **1**) that appears in Fig. 5.1, is known as a strong binder to CB7. The binding is characterized by the binding constant  $k_A$  which is defined for the chemical equation:



as

$$k_A = \frac{[\text{guest@host}]}{[\text{guest}][\text{host}]},$$

where  $[\cdot]$  denote concentrations. For **1** and CB7  $k_A \sim 10^{12} \text{ M}^{-1}$ . Whereas the cavity size of CB7 is  $279 \text{ \AA}^3$  [59] and large enough to accommodate the blocker, the cavity size of CB6 is  $164 \text{ \AA}^3$  [59] and probably too small to encapsulate the blocker. It was also

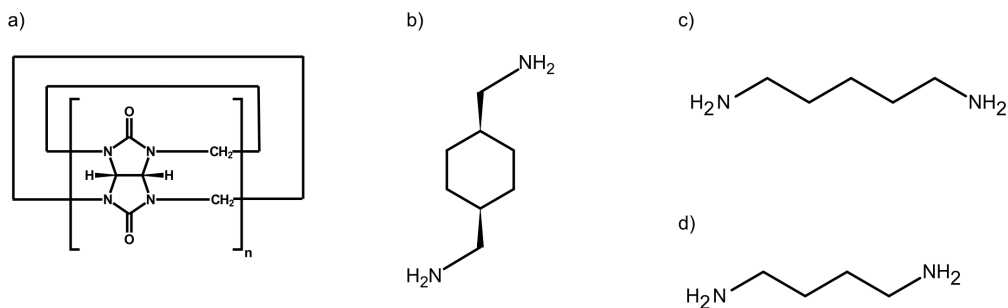


Figure 5.1: Chemical structures of hosts and guests. a) CB $n$  general scheme, in 3D the  $n$  repeating units form the macrocyclic hosts CB7/CB6 (with  $n = 7/6$ ). b) *cis*-1,4-Bis(aminomethyl)cyclohexane, strong binding guest of CB7. c) Cadaverine. d) Putrescine. Drawings were done with ChemSketsch (ACD/ChemSketch, version 2021.1.1, Advanced Chemistry Development, Inc., Toronto, ON, Canada, www.acdlabs.com, 2022).

suggested by Marquez et al. [60] that the effective container volume of the CB6 cavity is approximately  $105 \text{ \AA}^3$ . This also supports that the volume of the blocker exceeds the available cavity space. Another guests is cadaverine (1,5- diaminopentane), see Fig. 5.1. It has a smaller molecular volume than the blocker and can bind both to CB6 with binding affinity of  $k_A$  of  $10^9 - 10^{10} \text{ M}^{-1}$  [61] and to CB7 with binding affinity of  $k_A = 1.4 \times 10^7 \text{ M}^{-1}$  [62]. Putrescine (1,4- diaminobutane) is another guest that binds stronger to CB6 with  $k_A = 2 \times 10^7 \text{ M}^{-1}$  [63] than to CB7 with  $k_A = 3.7 \times 10^5 \text{ M}^{-1}$  [62].

Xenon atoms can also be considered as guests to CB $n$ , yet when it comes to describing their exchange kinetic with CEST, a different parameter than the binding constant is important, namely the exchange rate. Xenon was assumed to have a a faster exchange rate with CB7 than with CB6 due to the larger cavity of the former. However, this exchange rate was never quantified. The dissociation rate of Xe and CB6 was in fact quantified by using the HyperCEST method [50],  $k_{BA} = 2100 \text{ s}^{-1}$ , among other exchange kinetic parameters. The relative high exchange rate makes CB $n$  promising candidates as so-called HyperCEST agents for ultra-sensitive Xe MRI [64].

It should be mentioned in this context that certain hosts yield only very labile

interactions for Xe with presumably short resident times around the portals. One example is the family of macrocyclic hosts based on pillar[5]arene. They were studied as potent saturation transfer agents due to their expected fast Xe exchange rate [51]. A member of this family was investigated for its host-guest dynamic with  $^{129}\text{Xe}$  and the reported z-spectrum showed a broad peak around the free Xe saturation frequency and no peak around the bound Xe saturation frequency. This indicated that the exchange kinetics of  $^{129}\text{Xe}$  and pillar[5]arene under the studied conditions can be described by some kind of fast (labile) interaction which is not CEST based.

Xenon HyperCEST could presumably be applied to sense the formation of a host-guest complex of CB7 and a potential guest. This would be reported in the z-spectrum by the CEST response, where its partial or a complete suppression would reveal the degree of occupancy of the cavity. This concept, can find many applications, for example, sensing for stabilization of fluorescent dyes as reported in [65–68]. This motivated us to explore the host-guest system of CB7 with different blocking molecules and revealed differences in host-guest interactions for CB6 vs. CB7.

The portal to the cavity of CBn is another important characteristic that affects their exchange with guests [69–71]. Electrostatic interactions between positively charged cations and the negative carbonyl groups at the portal was demonstrated to decelerate the host-guest exchange rate [72–74]. Thus, the portal role should be kept in mind when coming to analyze CBn host-guest systems and more specifically when analyzing Xe HyperCEST observations from CB7 systems.

A direct comparison of spectra from different host/guest combinations would obviously benefit from accelerated methods that preserve the spectral information. Thus, the CAVKA method was tested for a CB7 application and evaluated the impact of three competitive molecular binders *cis*-1,4-bis(aminomethyl)cyclohexane (**1**), cadaverine (**2**) and putrescine (**3**) that impact the accessibility for mono-atomic Xe. The method acquires multiple spectra simultaneously to reveal different exchange kinetics from a combination of different hosts and guests and emphasizes the analytical potential of CEST spectroscopic imaging in accelerated screening.

## 5.2 Results and discussion

In the following subsections, all results are from double phantom experiments. These, unless stated otherwise, contained CB7 (50  $\mu\text{M}$  aqueous solution, Strem Chemicals Inc., Kehl, Germany) in the inner compartment. The outer compartment also contained a 50  $\mu\text{M}$  CB7 solution but also either of the competitive guests **1** (*cis*-1,4-bis(aminomethyl)cyclohexane, TCI chemicals, Eschborn, Germany) or **2** (1,5-diaminopentane, Sigma Aldrich, Taufkirchen, Germany). **1** was added with an up to 60-fold excess over the CB7 concentration, **2** was added with 10-fold dilution relative to the CB7 concentration. Samples were measured at room temperature ( $T = 298\text{K}$ ) by using the variable temperature unit to maintain stable conditions.

In section 5.2.3 CB6 (Strem Chemicals Inc., Kehl, Germany) was used. A CB6 stock solution in  $\text{H}_2\text{O}$  at a concentration of 10  $\mu\text{M}$  was prepared (the solubility of CB6 in water is  $\leq 18 \mu\text{M}$  [75]) and then further diluted to concentrations of 5, 1.5, 1, 0.5  $\mu\text{M}$ . They were used in either single or double phantom experiments. CB6 (10  $\mu\text{M}$ ) was also mixed with the guest **1** at a 1 : 1 ratio. CB7 dilution of 0.5  $\mu\text{M}$  was also prepared (additionally to the 50  $\mu\text{M}$ ) and was used with/without the addition of the guest **1** at a 1 : 1 ratio. 5 mM aqueous solution of the guest **3** (1,4-diaminobutane, Sigma Aldrich, Taufkirchen, Germany) was prepared and further diluted (by adding it to CB7 solutions) to final concentrations of 0.5, 1, 4  $\mu\text{M}$ . CB7 + **3** solutions were used in either single or double phantom experiments.

Scans were performed using a modified 2D FLASH sequence; to include a preceding CEST preparation block and a VFA scheme for the excitation pulses.  $^{129}\text{Xe}$  imaging parameters were:  $TE = 4$  ms,  $TR = 48.8$  ms,  $FOV = 10 \times 10$  mm<sup>2</sup>, slice thickness = 20 mm,  $BW = 5$  kHz, encoding order = "centric", matrix size (image resolution) =  $32 \times 32$ . Smaller matrix sizes for keyhole acquisitions were realized by changing the phase encoding interpolation parameter from 1 (matrix =  $32 \times 32$ ) to 4 (matrix =  $32 \times 8$ ). This parameter has the same meaning as  $R$  and appears in the nomenclature of CAVKA reconstructions, e.g., CAVKA-4 for an undersampling factor of 4. Averaging was done separately (outside ParaVision) on complex-valued raw data in Python. The xenon fraction was 5% of the gas mixture (with helium and nitrogen)

and was delivered to the sample at a continuous flow rate of 300 standard ml/min and at a total pressure of 4.5 bar. 100 ml/min of the total gas flow (70 ml/min with 3 mM **1** to reduce foaming) was bubbled into the sample. Bubbling was performed for 15 s (20 s with 70 ml/min flow) and additional 3 s (4 s with 70 ml/min flow) were added afterwards allowing potentially generated gas bubbles to collapse. For CEST preparations, a rectangular pulse with amplitude  $B_1 = 6 \mu\text{T}$  (71 Hz) and duration  $t_{\text{sat}} = 20$  s was used. Where z-spectra were acquired, saturation was applied at 36 offsets (−361.4, −361.3, −360.4, −121, −111.5, −101, −100, −99, −98, −97, −95, −93, −92, −91, −90, −89, −78.5, −69, −61.9, −54.8, −47.7, −40.6, −31.1, −21.6, −12, −9, −6, −3, 0, 3, 6, 9, 12, 21.6, 31.1 and 40.6 ppm) relative to  $^{129}\text{Xe}$  in water. The first three offsets were used as dummy scans to stabilize the gas delivery and were not included in the data processing. All data post-processing and analysis was performed using self-written Python scripts (Python Software Foundation. Python Language Reference, version 3.8. <http://www.python.org>). The reference power for accurate VFA implementation was calibrated in the beginning of each acquisition by curve fitting to the transverse magnetization decay along the k-space lines with constant flip angle (CFA) and disabled phase encoding (and the rest of the acquisition parameters as in the post calibration images) of a pure water sample (see section 1.3).

In section 5.2.3 CEST spectroscopy was done with conventional unlocalized acquisition (in addition to MR imaging) using a (pseudo) 2D sequence that included saturation and excitation. The saturation pulse had a power of 3 mW ( $6.2 \mu\text{T}$  or 73 Hz) and duration of 20 s. Z-spectra were acquired with 61 saturation frequencies offsets (−200, −200, −200, −130, −120, between −111 and −80 in steps of 1, −70, −60, −50, −45, −40, −35, −30, −25, −20, −15, −10, −5, 0, 5, 10, 15, 20, 25, 30, 35, 40, 200, 200 and 200 ppm) relative to  $^{129}\text{Xe}$  in water. The first five offsets were used as dummy scans to stabilize the gas delivery and the last three offset were turned out unnecessary. These offsets were not included in the data processing. Gas flow parameters and composition and bubbling times were the same as in the imaging experiments. Additionally, short imaging experiments in a single phantom were also performed. They included a list of only 9 saturation frequencies offsets (−360, −360, −360, −121, −95, −69, −40.6, 0 and 40.6 ppm) relative to  $^{129}\text{Xe}$  in water where

the first three offsets were acquired as dummy scans (to stabilize the gas flow) and were omitted in data processing. CFA scheme for the excitation pulses was used,  $FA = 20^\circ$ . Matrix size =  $32 \times 32$ . The rest of the acquisition parameters were the same as in the double phantom experiments (detailed in the previous paragraph). Volume of the samples in the single phantom was 1.5 ml.

### 5.2.1 Synergistic benefits from the CAVKA acquisition

CAVKA aims to make optimum use of the available magnetization, minimizes the necessary segmentation, and confines time-consuming signal averaging to the shared reference data that requires higher segmentation of the starting magnetization. Separate analysis of the impact from the reduced keyhole size and from using the reference image illustrates a yet unused synergistic effect as follows: The VFA approach ensures equal initial magnetization for each line in the encoding matrix (k-space). Such stable signal intensity along the phase encoding dimension prevents blurring in the image that would otherwise impair quantification based on the ROIs in the entire image array. However, accelerated exchange conditions make any multidimensional encoding challenging. Figure 5.2 exemplary shows the limited starting quality that gradient echoes provide for spatial encoding: a single scan does not provide sufficient spatial information to visualize the sample geometry (Fig. 5.2a). This problem originates from two aspects. 1) Since VFA requires to employ gradient echoes along the phase encoding dimension, it provides significantly less starting magnetization than a spin echo train that would in fact start with maximum transverse magnetization. 2) The exchange-driven accelerated (irreversible) loss of phase coherence causes incomplete refocussing and thus further signal reduction (see also section 5.2.4). This issue would occur for any type of echo formation, but spin echoes of magnetization pools under accelerated exchange would suffer from unacceptable decay of magnetization along the phase encoding dimension. VFA segmentation is thus a suitable concept, it just needs to be complemented by signal averaging if a certain matrix size is exceeded.

Averaging of the (complex-valued) raw data was thus applied and indeed recovered the sample geometry (Fig. 5.2b). The full synergistic effect of the CAVKA approach is shown in Fig. 5.2d. The VFA approach provides the control to achieve a reduced

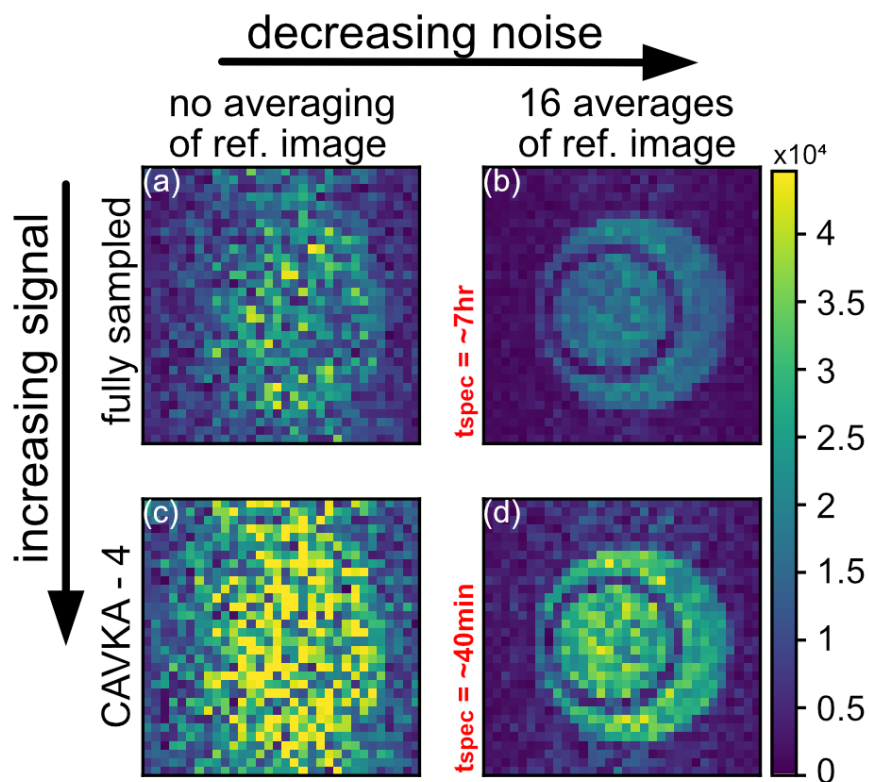


Figure 5.2: Four combinations of applying/omitting the two components of the CAVKA acquisition. Signal increase due to VFA-enhancement (top vs. bottom row) and noise decrease due to averaging (left vs. right column). The acquisition time  $t_{\text{spec}}$  of a z-spectrum (with 36 offsets) is reduced 11-fold in the CAVKA acquisition relative to conventional averaging.  $^{129}\text{Xe}$  MRI of phantom with  $50 \mu\text{M}$  CB7 (aqueous solution) in the inner compartment and CB7 : 1 at 1 : 60 molar ratio in the outer compartment.

segmentation for the k-space center with higher signal. Fig. 5.2c shows this signal gain with 4-fold fewer lines for the k-space center than in Fig. 5.2a. It still lacks the geometrical details because the k-space periphery is acquired with high noise. Finally, Fig. 5.2d presents the effect of combining a VFA-enhanced center and an averaged periphery in a CAVKA acquisition and its significant SNR improvement compared to the conventional application of VFA (Fig. 5.2a). Our application of CAVKA involves acquisition of a complete HyperCEST spectrum (36 offsets) with overall acquisition time  $t_{\text{spec}}$ . Employing 16 averages throughout the full spectral domain would result in an unacceptable  $t_{\text{spec}} = 7.3$  hours. With CAVKA, we reuse one-time acquired averaged data (of a reference scan) in each offset of the spectrum and achieve a serious reduction down to  $t_{\text{spec}} = 39.5$  minutes (11-fold acceleration). This is independent of the general advantage of including the option to obtain image-based data from multiple samples at once to achieve  $2 \times 11$ -fold acceleration, i.e., the acquisition time is reduced by 95.5%.

### 5.2.2 HyperCEST spectroscopy of accelerated exchange with competitive guest binding

After quantifying the benefits of CAVKA, we next acquired two HyperCEST spectra simultaneously by using a two-compartment phantom that contained CB7 as a host in the inner compartment and CB7 together with the competitive guest **1** as a potential CB7 “blocker” in the outer compartment. Xenon was dispersed into both samples where freely accessible CB7 alone provides presumably rapid guest turnover. The blocker in its *cis* conformation has a high affinity ( $k_A \sim 10^{12}$ ) for CB7, thus it is expected to at least impair (or completely suppress) the xenon exchange with CB7. As first experiment we compared the z-spectra from a solution of CB7 : **1** at 1 : 1 ratio and a solution containing only CB7. Fig. 5.3a shows these two spectra. Contrary to the expectation, no difference between the CEST responses with or without the blocker is detected. However, a difference between the spectra does appear in the form of the broader response from the direct saturation around 0 ppm in the absence of the blocker. At this stage, two possible explanations were considered: 1) as we do observe a CEST response at  $-95$  ppm xenon must reach the CB7 cavity. The

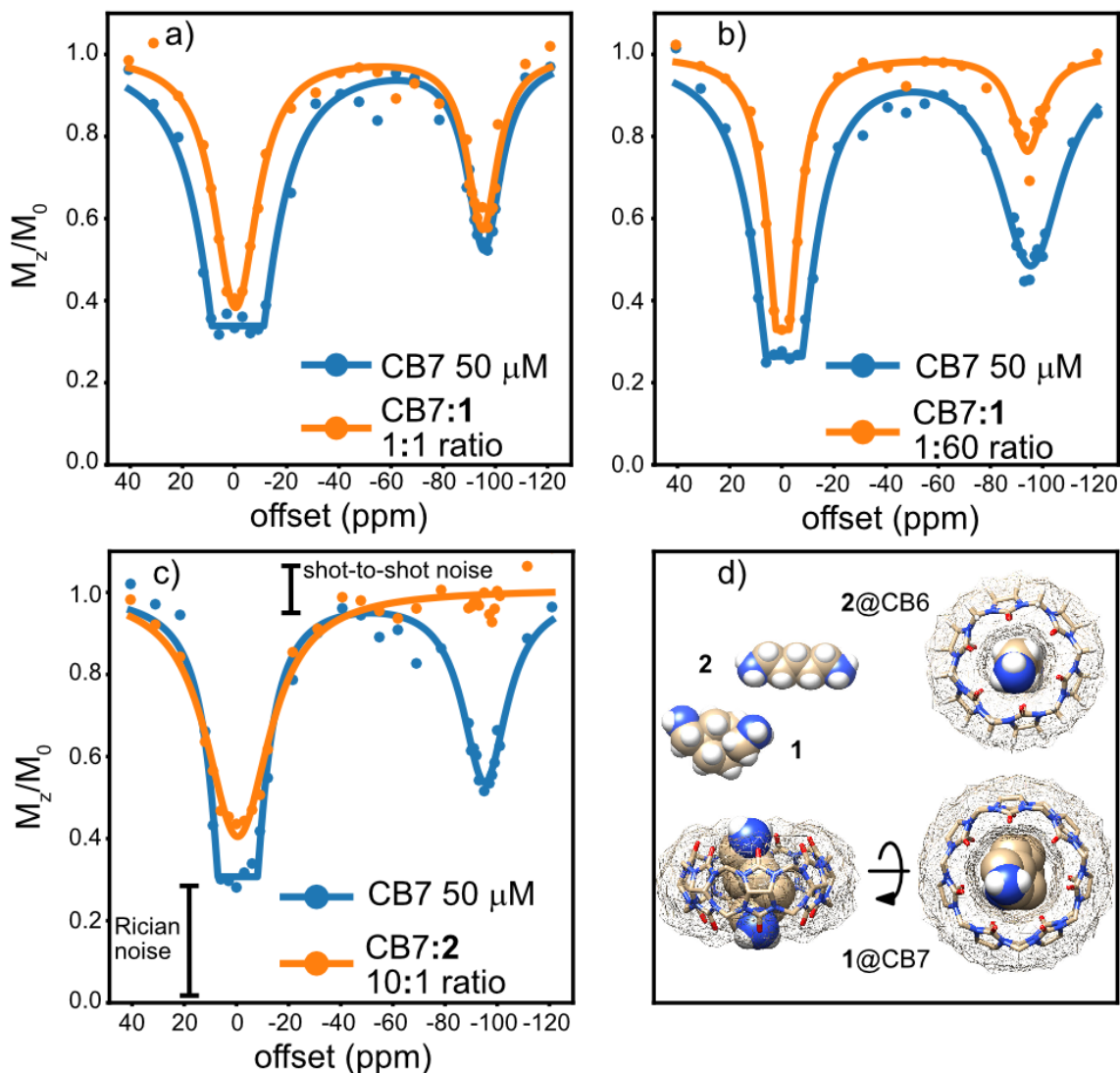


Figure 5.3: Comparative HyperCEST z-spectra acquired with the CAVKA method to study the exchange of Xe with CB7 and **1**. a) CEST response from CB7 without **1** and from CB7 : **1** at 1 : 1 ratio. b) No full suppression of the CEST response from CB7 upon addition of **1** in 60-fold excess. c) Suppression of the CEST response upon addition of **2** in only 1/10 of the CB7 concentration, indicating the CEST response is actually from the CB6 impurity. d) Chemical structure of the guests **1** and **2** and the host-guest complexes **2@CB6** and **1@CB7** (in two viewing angles). Points represent experimental data (ROI-averaged values) and solid lines are fitting of Lorentzian curves.

cavity could also be occupied by the blocker and therefore there is a co-occupancy of the CB7 cavity by one blocker molecule and one xenon atom. However, if this is the case, one would also expect the chemical shift to change and no longer to appear at  $-95$  ppm. 2) Xenon kicks out the blocker molecule from the cavity, in this case the chemical shift value matches the expectation, but the high binding affinity of the blocker to CB7 makes this hypothesis rather unlikely. Another experiment was thus conducted, i.e., the same as the first experiment, but this time with a solution of CB7 : **1** at 1 : 60 ratio. Fig. 5.3b shows the comparative spectra. With an excess of the blocker over CB7, we highly expect to completely suppress the CEST response in the orange curve. However, a CEST response is still observed, although it is weaker than the response seen in the spectrum of CB7 : **1** at 1 : 1 ratio (orange curve in Fig. 5.3a). Consistently with the previous experiment, a narrower solution peak appeared when the blocker is present (orange vs blue curves in Fig. 5.3a and 5.3b). The fact that one could still observe a CEST response is again not in line with expectations and thus a third hypothesis was formulated: 3) Only the CB6 residuals in the CB7 solution [58] cause the observed CEST response. The chemical shift of xenon inside CB6 is also at  $-95$  ppm [50], thus the CEST response could indeed come from CB6. Additionally, the CB7 blocker (**1**) is a too bulky guest to occupy the CB6 cavity and to block it for the xenon exchange, which is in line with the result of the first experiment, where we could not detect any difference between the CEST response with or without this blocker (Fig. 5.3a). At a 60-fold excess of the blocker we do see partial suppression, thus we can only speculate that this high excess of the blocker produces conditions that eventually lead to partial penetration into the CB6 cavity. To test the third hypothesis, we designed another double phantom experiment. This time in the outer compartment the CB6 blocker **2** (cadaverine) was used which binds strongly to CB6 ( $k_A \sim 1 \times 10^9 \text{ M}^{-1}$ ). By using a solution of CB7 : **2** in 10 : 1 ratio ( $5 \mu\text{M}$  cadaverine), we would be able to completely suppress a CEST response from the up to 10% CB6 impurity, but would only partially suppress a CEST response from CB7. Fig. 5.3c presents the results of this experiment with a full suppression of the CEST response in the cadaverine compartment (orange vs. blue curve in Fig. 5.3c). Therefore we could conclude that the xenon HyperCEST response detected

from a CB7 solution is actually from a CB6 impurity. Moreover, CB7 does not produce a CEST response (peak) in a HyperCEST spectrum, which could also be inferred from the complete suppression. The fact that we could measure such a clear CEST response from a CB6 impurity actually demonstrated the high sensitivity of the HyperCEST method. The accelerated acquisition of CEST spectra from CAVKA-encoded data thus revealed the details of the competitive host-guest systems studied here that would otherwise require significantly longer acquisition times. It nicely demonstrated the first example of a co-analysis of fast and slow Xe exchange regimes within the same sample. Conventional spectroscopy would not reveal this interaction and comparative CEST measurements clearly benefit from the acceleration enabled by CAVKA to screen multiple samples at once. Overall, a labile interaction of Xe with the CB7 portals, as observed for pillar[5]arenes [51] is now assumed. Addition of the blocker impair this labile interaction which manifested as the narrowing of the direct saturation response around 0 ppm. Such interactions are reflected by the symmetric magnetization transfer (MT) effect around 0 ppm. It does not provide a separate CEST response that would allow more detailed analysis, see also section 5.2.4.

### **5.2.3 Further investigations regarding the hypothesis that the CB6 impurity in CB7 is the only source of the CEST response**

To further base the theory that the host which provides the CEST response in a CB7 sample is not CB7 but rather CB6, a number of additional experiments were performed. They are described in this section.

A solution of 0.5  $\mu\text{M}$  CB7 was prepared and was tested for CEST response with and without the addition of the blocker **1** at 1 : 1 ratio. In this low concentration of CB7, the CB6 impurity is unlikely to produce a significant CEST response. Thus, the potential residual CEST response from CB7 can be measured and also the blocking effect of **1** on CB7. The measurement was done by the CAVKA acquisition with the double phantom with CB7 in the inner compartment and CB7 + **1** in the outer compartment. Fig. 5.4a shows the z-spectra from the two compartments. There was no CEST response detected in the CB7 compartment and also no response in the

compartment of CB7 + **1**. This result confirms the above interpenetration since the CB6 impurity is at a too low concentration to produce a CEST peak in the spectrum (in blue). Regarding the second spectrum (orange), there was no CEST peak that could be suppressed. Additionally, the solution peak around 0 ppm (blue spectrum) is not as wide as with the 50  $\mu\text{M}$  CB7 (see Fig. 5.3a). This can be explained by the lower CB7 concentration for which the labile interaction between xenon and the CB7 portals is also reduced. The width of the solution peak does not get smaller upon the addition of **1** to CB7 (orange spectrum) since the effect of the labile interaction on the width is presumably negligible before the addition of the blocker to yield a change when the blocker is added. Additional control experiment in section 5.2.4 showed that CB7 was present in the solution by a shorter FID duration relative to pure water.

A solution of 0.5  $\mu\text{M}$  CB6 was also prepared in order to test if CB6 in an isolated form can produce the same CEST response that was observed from 50  $\mu\text{M}$  CB7. CB7 contains up to 1% impurities according to the commercial provider and therefore 50  $\mu\text{M}$  CB7 could contain up to 0.5  $\mu\text{M}$  CB6. To measure these solutions and plot their  $z$ -spectra, unlocalized spectroscopy acquisitions were done to reduce the noise. They are more time consuming relative to the CAVKA method, however since the CAVKA method is novel, it was decided to invest the extra time in order to improve spectral quality for detecting CB6 traces. Fig. 5.4b displays the  $z$ -spectra. In the spectrum of 0.5  $\mu\text{M}$  CB6 (orange) a CEST peak could not be observed. This, allegedly, contradicts the hypothesis that CB6 is the source of the CEST signal. However, since the chemical shift between free and bound Xe in the spectrum of 50  $\mu\text{M}$  CB7 (ca. 95 ppm) matches the chemical shift in a CB6 spectrum (of higher concentration than 0.5  $\mu\text{M}$ , e.g., in [9, 61]) and it is unlikely that a different cavity than that of CB6 would result with the same chemical shift between free and bound xenon, it still seems that the hypothesis of CB6 as the CEST-providing host is true. Nevertheless, for the hypothesis to be in line with this result, the concentration of the CB6 impurity in CB7 must be higher than 1%. To demonstrate that the same CEST response as from 50  $\mu\text{M}$  CB7 can be reproduced by a CB6 solution with a higher concentration than 0.5  $\mu\text{M}$ , the  $z$ -spectrum of 5  $\mu\text{M}$  CB6 was acquired. It appears in Fig. 5.4b

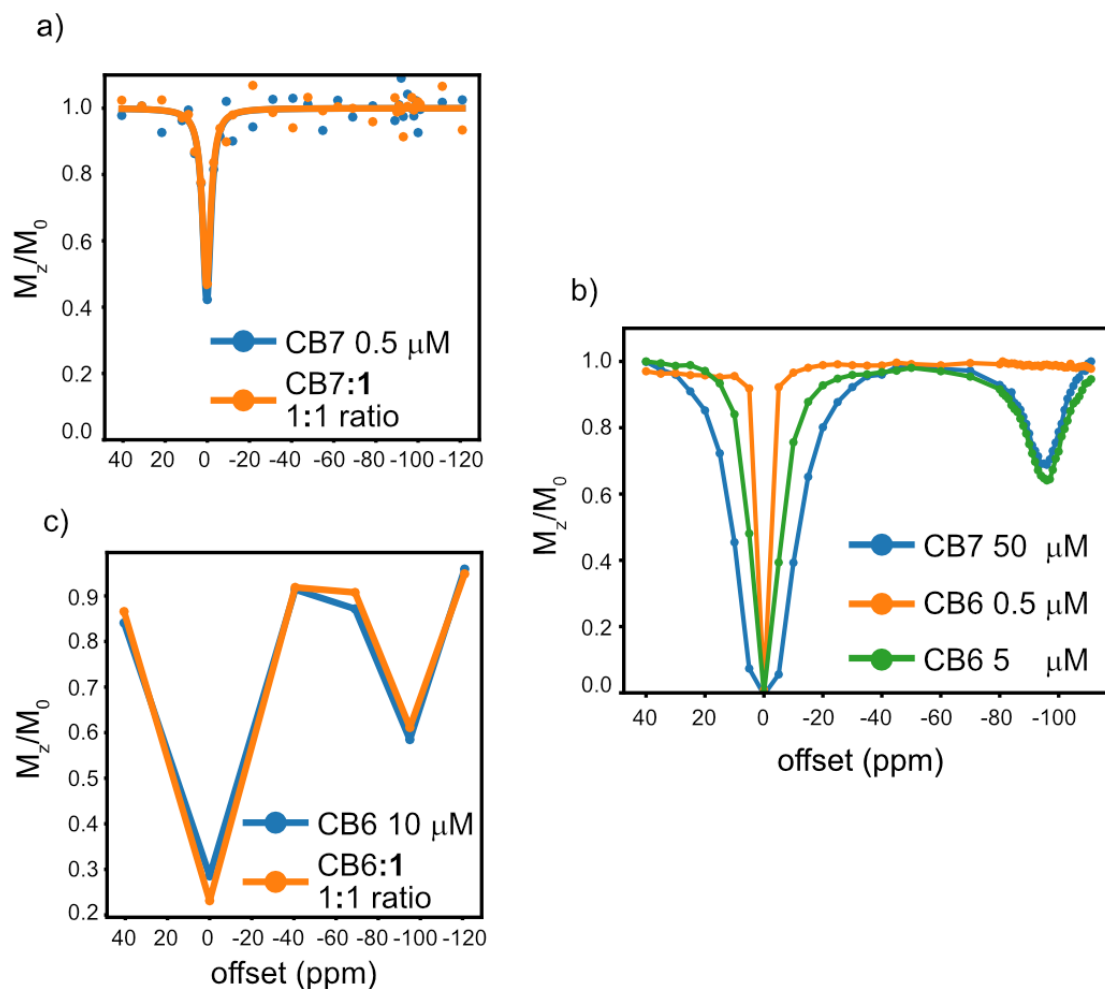


Figure 5.4: Tests with CB6, CB7 and **1** to identify the source of the of CEST response from CB7 samples. a) No CEST response is detected for 0.5  $\mu\text{M}$  CB7 (blue) where the concentration of the CB6 impurity is too low to be detectable and no change in the response upon the addition of **1** (orange) is seen. b) High resolution data with unlocalized spectroscopy: 0.5  $\mu\text{M}$  CB6 (orange) does not reproduce the CEST response of 50  $\mu\text{M}$  CB7 (blue). However, increasing the concentration of CB6 to 5  $\mu\text{M}$  (green) does give a comparable CEST response, showing that Xe chemical shifts ( $\sim 95$  ppm) from the samples of CB6 and CB7 match. c) Coarse sampling: No effect of the blocker **1** on CB6, confirming the observation in Fig. 5.3a by using a sample of isolated CB6 (instead of CB6 impurity in CB7).

(green). It shows that indeed the chemical shifts in the spectra from CB6 and CB7 (green and blue) match and it also shows that the signal dips around  $-95$  ppm in the two spectra are very similar in intensity. Since the results suggest that the CB6 impurity exceeds 1%, an inquiry with Strem was made about how they determine the degree of purity. Their response was by  $^1\text{H}$  NMR and elemental analysis. However,  $^1\text{H}$  NMR would not easily detect low concentrations of CB6 impurity ( $\leq 10\%$ ) in a CB7 sample and therefore the possibility that an impurity of CB6, which is higher than 1%, is not completely excluded. The green and blue spectra in Fig. 5.4b show the broader solution peak around 0 ppm in the CB7 spectrum that is assumed to be the result of a labile interaction between Xe and the portals of CB7 (see section 5.2.2). This interaction was also shown to be influenced by the blocker **1**. In contrast, the narrowing of the solution peak upon reducing the CB6 concentration (orange vs. green spectra) is due to the lack of a CEST response in the orange spectrum since the width of the solution peak also depends on the existence of the CEST peak.

Finally, the blocking effect of **1** on isolated CB6 (that is not simply an impurity in CB7) was tested. In the previous section (5.2.2), it was concluded that this blocker does not suppress the CEST response from the CB7 sample since the response comes from the CB6 impurity and that **1** is probably too bulky to occupy its cavity. However, this non-blocking effect was not tested with a dedicated CB6 solution and this is done here. To this end, a  $10\ \mu\text{M}$  CB6 solution was used and was tested for the CEST response with and without the addition of **1** at 1 : 1 ratio. This ratio was chosen because in the original experiment (CB7 : **1** at 1:1 ratio) most of **1** is included in CB7 leaving no measurable impact on CB6. The two experiments were done as short imaging experiments with reduced saturation frequencies listed in the single phantom, Fig. 5.4c shows the results. The list of saturation frequencies was designed to capture the CEST response and the solution response (around 0 ppm) while being relatively short to save time. It therefore produces results with a limited resolution yet sufficient for this type of control experiment. The spectrum of CB6 (blue) and the spectrum of CB6 + **1** display the same CEST response. Thus, as expected no blocking ability of **1** on CB6 was detected. Although the CB6 impurity has presumably a lower concentration than  $10\ \mu\text{M}$ , this concentration allows to get a more consistent CEST

response and therefore permits testing for the blocking effect reliably.

To narrow down the concentration of the CB6 impurity, a series of experiments with different CB6 concentrations were performed to identify the concentration that produces the same CEST response from the 50  $\mu\text{M}$  CB7 sample. To this end, short imaging experiments in the single phantom were done. CB6 solutions, starting with a concentration of 0.5  $\mu\text{M}$  and increasing the concentration in 0.5  $\mu\text{M}$  steps, were measured for their CEST response and were compared to the response of the CB7 sample. Fig. 5.5a shows the results. The CEST response increases when CB6 concentration increases and a concentration of 1.5  $\mu\text{M}$  (red) comes close to the response from 50  $\mu\text{M}$  CB7 (blue). Next, a more detailed CAVKA acquisition of the double phantom with 50  $\mu\text{M}$  CB7 in the inner compartment and 1.5  $\mu\text{M}$  CB6 in the outer compartment was performed to directly compare the CEST responses in a more accurate way with a longer frequency list. Fig. 5.5b shows the results. In contrast to the single on-resonant shot in Fig. 5.5a, the fully acquired CEST response from the CB6 compartment is lower than from the CB7 compartment. This means the CB6 impurity concentration is higher than 1.5  $\mu\text{M}$  and the discrepancy between the two measurements is related to the inaccuracy of the short imaging experiment. Although the responses in Fig. 5.5b are not equal, a quantitative analysis based on information extracted from Lorentzian fitting to the two spectra provided an estimation of the impurity concentration.

The CEST response (signal at  $-95$  ppm) can be modeled using the term  $M_0 e^{-\lambda t_{\text{sat}}}$  where  $\lambda$  denotes the xenon depolarization rate,  $t_{\text{sat}}$  the saturation time and  $M_0$  the unsaturated signal (the spectrum baseline). In the weak saturation regime (saturation pulse strength used in experiments is in this regime) the depolarization rate can be approximated as

$$\lambda \approx f_{\text{B}} k_{\text{BA}} \frac{(\gamma B_1)^2}{k_{\text{BA}}^2 + (\gamma B_1)^2}. \quad (5.1)$$

$B_1$  is the saturation pulse amplitude,  $f_{\text{B}}$  is the concentration fraction of bound xenon ( $[\text{Xe@host}]/[\text{Xe}]$ ) and  $k_{\text{BA}}$  is the rate with which the host releases xenon (see section 1.5). For CB6 (in water), this rate was quantified as  $k_{\text{BA}} = 2100 \text{ s}^{-1}$  [50]. Assum-

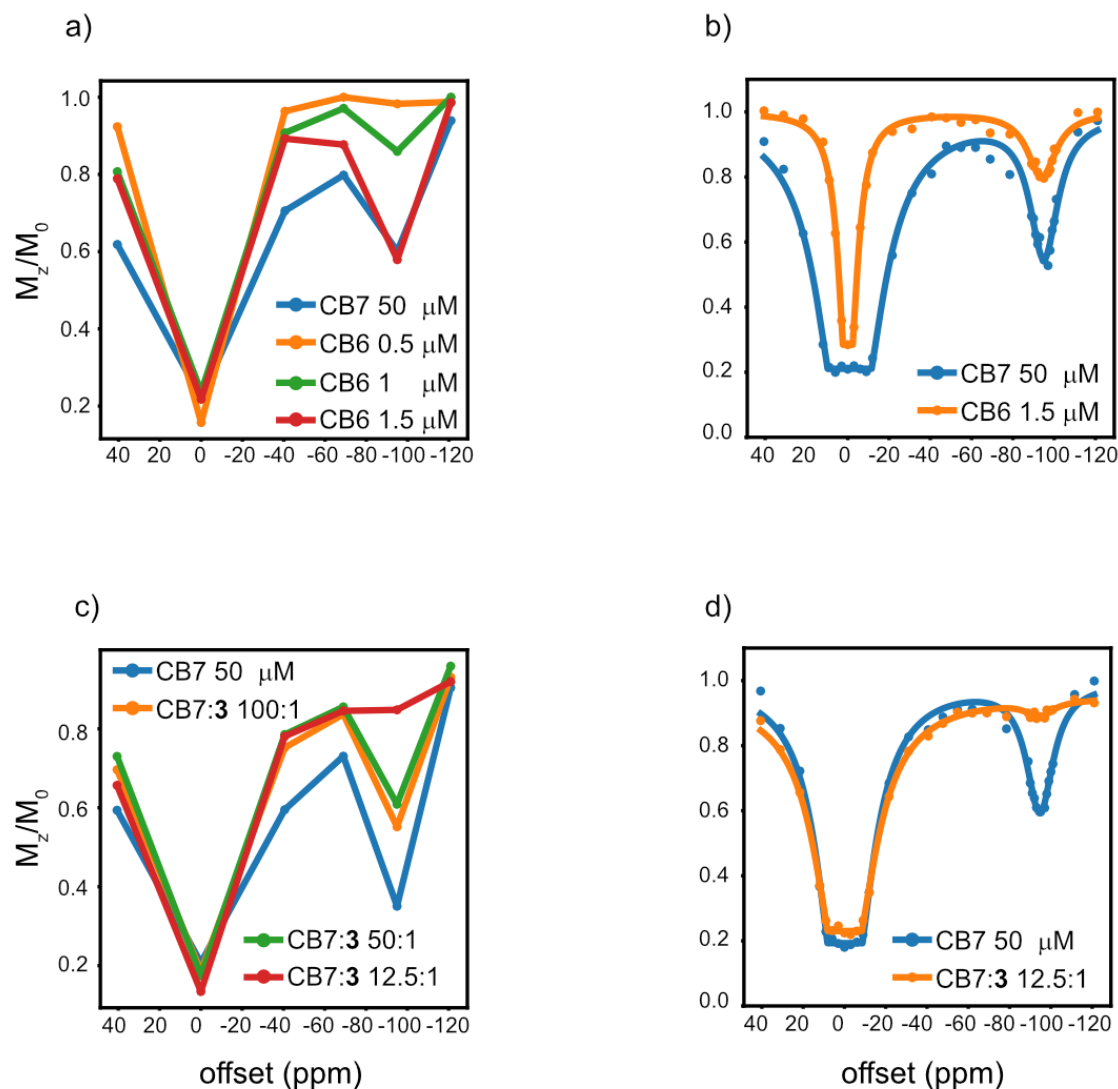


Figure 5.5: Estimating the concentration of the CB6 impurity in a CB7 sample. a) Comparing the CEST response (at  $-95$  ppm) from a  $50 \mu\text{M}$  CB7 solution to increasing concentrations of CB6. b) Using an initially approximated CB6 concentration (from a) in a double phantom experiment with dedicated CAVKA acquisition. Based on the two comparative spectra (through parameter extraction from Lorentzian curve fitting) an estimation for the CB6 impurity could be made. c) Testing for the concentration of guest **3** that blocks the CEST response from CB7 sample. d) Using an initially approximated concentration of **3** for a direct comparison with unblocked CB7 by a CAVKA acquisition of the double phantom. The acquired spectra allowed, based on parameter extraction from Lorentzian curve fitting, to give one more estimation to the concentration of the CB6 impurity.

ing that the CEST-providing host in both spectra is CB6 (same  $k_{BA}$ ) and since the saturation pulse amplitude was also the same in both acquisitions (same  $B_1$ ), the ratio between the depolarization rates according to Eq. 5.1 reduces to the ratio of  $f_B$ . Moreover, since both measurements are done with an excess of xenon over the host, the ratio of  $f_B$  between the two compartments represents the ratio of the host concentrations. The value of each depolarization rate can be extracted from Lorentzian curve fitting to each spectra and their ratio yielded 2.59 (see Table 5.1). The CB6 sample had a concentration of  $1.5 \mu\text{M}$  and thus the CB7 sample has a CB6 impurity concentration of  $3.9 \pm 0.5 \mu\text{M}$ . Table 5.1 provides all the parameter values and their errors (standard deviations) which were extracted from Lorentzian curve fitting. These values show, as was already observed, that the CEST chemical shifts are quite similar  $-95$  vs.  $-94$  ppm. Additionally, the values for the width of the CEST peak provide another indication that it is the same host in the two samples as they are quite similar with  $14.2 \pm 1.8$  vs.  $15.9 \pm 2.4$  ppm. The width of the CEST peak is related to the exchange rate constant  $k_{BA}$  (when the  $B_1$  amplitude is fixed), thus similarity of widths points to similarity of hosts. The slightly larger width from the CB6 sample can be partly explained by the  $B_1$  inhomogeneity that was investigated in [13]. CB6 was in the outer compartment which can potentially experience a higher  $B_1$  value and thus produces a moderate peak broadening compared to the inner compartment.

Repeating this calculation for the spectra appeared in Fig. 5.4b where the CB6 sample had  $5 \mu\text{M}$  concentration yielded a CB6 impurity concentration of  $4.6 \pm 0.1 \mu\text{M}$ . The parameter values extracted from the Lorentzian curve fitting for these spectra also appear in Table 5.1. This is consistent with the impurity concentration that was based on the CAVKA spectra with  $1.5 \mu\text{M}$  nominal CB6 reference (Fig. 5.5b) and also shows that the novel CAVKA method produces spectra of sufficient quality to allow curve fitting and extraction of parameters that are comparable with the traditional spectroscopy acquisitions. Nevertheless, the error of the extracted parameters is higher for the CAVKA spectra (see Table 5.1).

It is important to mention the non-linearity of the CEST response with respect to the host concentration (exchange of already saturated xenon atoms), when the response is over  $25 - 30\%$ , as was mentioned in [76]. In this cases, additional parameters need

Table 5.1: Parameter values extracted from Lorentzian curve fitting in the three experiments (E1 - E3) where quantitative analysis was performed for estimating the CB6 impurity concentration. E1: CB7 and 1.5  $\mu\text{M}$  CB6 (CAVKA, double phantom), E2: CB7 and 5  $\mu\text{M}$  CB6 (unlocalized spectroscopy, single phantom) and E3: CB7 and CB7 : **3** at 12.5 : 1 ratio (CAVKA, double phantom). 50  $\mu\text{M}$  CB7 was used in all experiments. The Lorentzian curve model was

$$f(x) = \max \left\{ M_0 e^{\frac{-\Delta_1(\Gamma_1/2)^2}{(\Gamma_1/2)^2 + (x-x_{01})^2} + \frac{-\Delta_2(\Gamma_2/2)^2}{(\Gamma_2/2)^2 + (x-x_{02})^2}}, R \right\},$$

where  $M_0$  is the unsaturated magnetization (curve baseline),  $\Delta_i$  is the depolarization constant (the product of the depolarization rate ( $\lambda_i$ ) and the saturation time),  $\Gamma_i$  is the peak width,  $x_{0_i}$  is the peak position and  $R$  is the noise level. Fitting was done first to the raw spectra to extract the value of  $M_0$  and then the spectra were normalized using this value and a second fitting was done.

		$M_0$	$\Delta_1$	$\Gamma_1$	$x_{01}$	$\Delta_2$	$\Gamma_2$	$x_{02}$	$R$
E1	CB7	$1 \pm 0.02$	$4.9 \pm 2.1$	$14.8 \pm 4$	$-0.97 \pm 0.4$	$0.57 \pm 0.03$	$14.2 \pm 1.8$	$-95 \pm 0.3$	$0.21 \pm 0.01$
	CB6	$1 \pm 0.007$	$1.9 \pm 0.2$	$6.6 \pm 0.5$	$0 \pm 0.1$	$0.22 \pm 0.01$	$15.9 \pm 2.4$	$-94 \pm 0.5$	$0.28 \pm 0.02$
E2	CB7	$1.04 \pm 0.007$	$10.7 \pm 3.4$	$6.1 \pm 1$	$-0.51 \pm 0.1$	$0.41 \pm 0.01$	$14.1 \pm 0.6$	$-94.5 \pm 0.1$	$0 \pm 0$
	CB6	$1 \pm 0.004$	$6.3 \pm 2.9$	$3.9 \pm 1$	$-0.4 \pm 0.07$	$0.45 \pm 0.009$	$13.9 \pm 0.4$	$-95.1 \pm 0.1$	$0 \pm 0$
E3	CB7	$1 \pm 0.02$	$4.7 \pm 1.4$	$12.4 \pm 2.5$	$-0.3 \pm 0.3$	$0.5 \pm 0.03$	$13.7 \pm 1.6$	$-94.7 \pm 0.3$	$0.2 \pm 0.01$
	CB7+ <b>3</b>	$1 \pm 0.008$	$2.7 \pm 0.2$	$17.7 \pm 1.2$	$-0.2 \pm 0.2$	$0.05 \pm 0.01$	$15.3 \pm 7$	$-94.4 \pm 1.2$	$0.2 \pm 0.006$

to be considered through fitting of the Lorentzian line shapes to allow comparisons. CAVKA delivers reliable spectra in a short time for a direct comparison between samples. The estimation of a host concentration based on a reference sample within one image has been shown in a more complex way in [77], but without the CAVKA acceleration.

The CB6 impurity concentration was estimated in yet another way through a series of experiments with guest **3** (putrescine). Unlike the blocking experiment with **2** (Fig. 5.3c) that was designed to show that the CEST-providing host is unlikely to be CB7 and led to the hypothesis that CB6 residuals provide the CEST response, the experiments with **3** are used to estimate these residuals concentration. First, the minimal putrescine concentration to achieve nearly full blocking of the CEST response from CB7 was tested. To this end, short imaging experiments in the single phantom were performed. The CEST response from a 50  $\mu\text{M}$  CB7 solution was measured and compared to the responses of solutions containing 50  $\mu\text{M}$  CB7 and **3** in increasing concentrations of 0.5, 1 and 4  $\mu\text{M}$ . Fig. 5.5c shows the results. An increasing suppression of the CEST response is observed upon increasing the concentration of **3** with an almost full suppression by the addition of 4  $\mu\text{M}$ . This type of short imaging experiments are with a limited accuracy but yet sufficient to determine the minimal blocking concentration that will be used next. This limited accuracy is also the reason for the increased CEST response observed from the CB7 solution compared to other measurements (60% vs. 40% ).

Next, a more detailed CAVKA acquisition of the double phantom that had 50  $\mu\text{M}$  CB7 in the inner compartment and CB7 : **3** at 12.5 : 1 ratio in the outer compartment was done. The spectra appear in Fig. 5.5d with the Lorentzian curve fitting. The fitting was done first to data of the CB7 compartment and then the obtained position and width of the CEST peak were used as prior knowledge to identify the residual CEST signal in the second compartment. Repeating one more time the quantitative analysis based on Eq. 5.1 provides the third estimation to the CB6 impurity concentration. A small difference here, compared to the other times of using this quantitative analysis, is that the depolarization ratio equals to the ratio of CB6 concentration in the CB7 sample to the unoccupied CB6 concentration in the sample of

CB7 and **3**. The result for the CB6 impurity concentration is  $4.4 \pm 0.09 \mu\text{M}$ . The parameter values extracted from the Lorentzian curve fitting for these spectra appear in Table 5.1.

The difference between the binding constants to CB6 and CB7 of each of the two guest **2** and **3** (cadaverine and putrescine) is roughly the same, i.e. 100-fold higher binding constant to CB6 than to CB7. Thus, it is expected that the by far larger part of the guest molecules would be included in CB6 and not in CB7, although CB7 is in excess over CB6 (ca. 10-fold according to the estimated concentration of the CB6 impurity). This is important since otherwise (i.e., for more similar binding constants) only small part of the guest would occupy CB6 and a full blocking could not have been observed.

The  $^{129}\text{Xe}$  HyperCEST response from CB7 was also studied in [78]. They believe that the origin of the response is not from CB7 since the width of the CEST peak was too narrow compared to that of CB6 (which has a smaller cavity and thus it is expected to have a slower exchange rate). Additionally, they observed that interactions of  $^{129}\text{Xe}$  and CB7 are manifested through a relatively wide solution peak. However, they suggested inverted CB7 (iCB7) as the source for the CEST response as ca. 1% of it is known to form as a stereo isomer during CB7 synthesis. iCB7 has a lower cavity size because of a one inverted unit of glycoluril and thus the peak of CB7-bound Xe was assigned to it. The option that iCB7 is a source for the CEST response is not excluded by this work as iCB7 is not commercially available and investigations to this matter were not possible. However, the matching chemical shifts from signals in CB6 and CB7 samples do not agree with the expectation that iCB7 with a rather different cavity shape and atom binding would yield a rather different chemical shift.

Additional candidates for the source of the CEST response could be presumably CB5 or CB8 that are also side products in CB7 synthesis. These are less likely to contribute to the observed CEST response as CB5 exchanges Xe in a slow rate of  $0.002 \text{ h}^{-1}$  [79] and CB8 has a low water solubility  $\leq 10 \mu\text{M}$  [54] and would exchange xenon rather fast.

In conclusion, the CB6 impurity concentration in CB7 is estimated to be in the range of 3.9 - 4.6  $\mu\text{M}$  or 7.8% - 9.2%. This was concluded from three independent

experiments and quantitative analysis of their hyperCEST spectra. The CAVKA experiments produced high quality spectra (that permit parameter extraction through curve fitting) and in a relatively short time.

#### 5.2.4 Labile exchange manifestation in the FID

The labile interaction between Xe and CB7 could also be observed in the  $^{129}\text{Xe}$  NMR FIDs from CB7 samples with and without the blocker. Fig. 5.6 displays the short FID (180 ms) as a consequence of the labile exchange between xenon and CB7 and the longer lasting FID (700 ms) when the blocker at 60-fold excess is added. Thus, upon inclusion of the blocker into the cavity, the blocker prevents some of the labile interaction between Xe and the portals of CB7 which are destructive to the magnetization (irreversible loss of the spins phase coherence) and by that the FID lasts longer. In Fig. 5.3d, the chemical structure of the inclusion complex of CB7 and blocker is shown. The amino groups of the blocker (nitrogen appear as blue spheres) stick out of the cavity and could, in theory, deny the access of xenon to the portals. This suggested mechanism explains the suppression of the labile interaction at the portals of CB7 which are otherwise known to affect host-guest exchange kinetics [72–74].

In section 5.2.3, an experiment with  $0.5\ \mu\text{M}$  CB7 (a relatively lower concentration than in other CB7 experiments) was done and in line with expectations, a CEST response was not observed. As indication that CB7 was still present in the solution, the FID from the CB7 sample was compared to the FID of a Xe in water sample. Fig. 5.7 shows the two FIDs. A shorter ringing FID was recorded for CB7 than for the water sample with signal decays within 0.6 vs. 2 s.

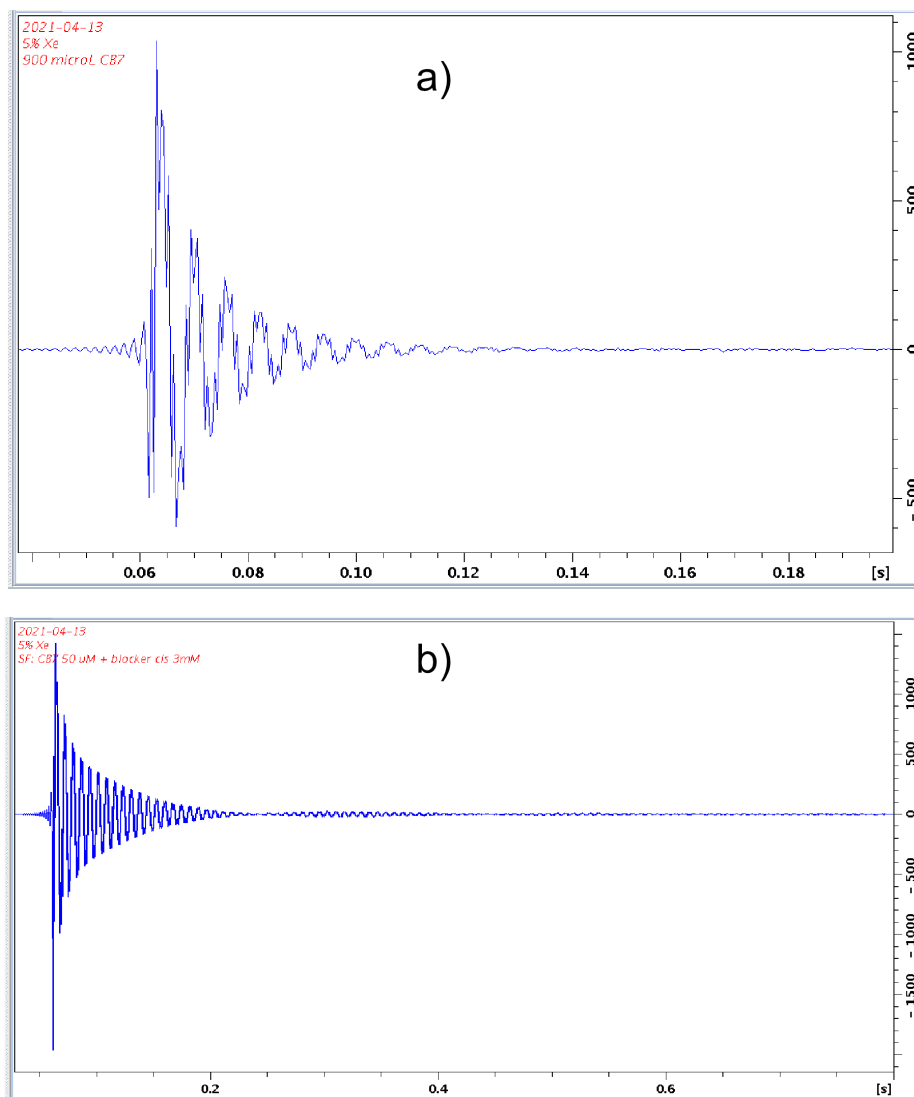


Figure 5.6: Labile interactions of CB7 and  $^{129}\text{Xe}$  indicated by the duration of the FID.  
 a) Duration of 180 ms when  $^{129}\text{Xe}$  has unrestricted access to CB7 (50  $\mu\text{M}$  solution).  
 b) Duration of almost 1 s in the presence of the blocker in a 60-fold excess over CB7.

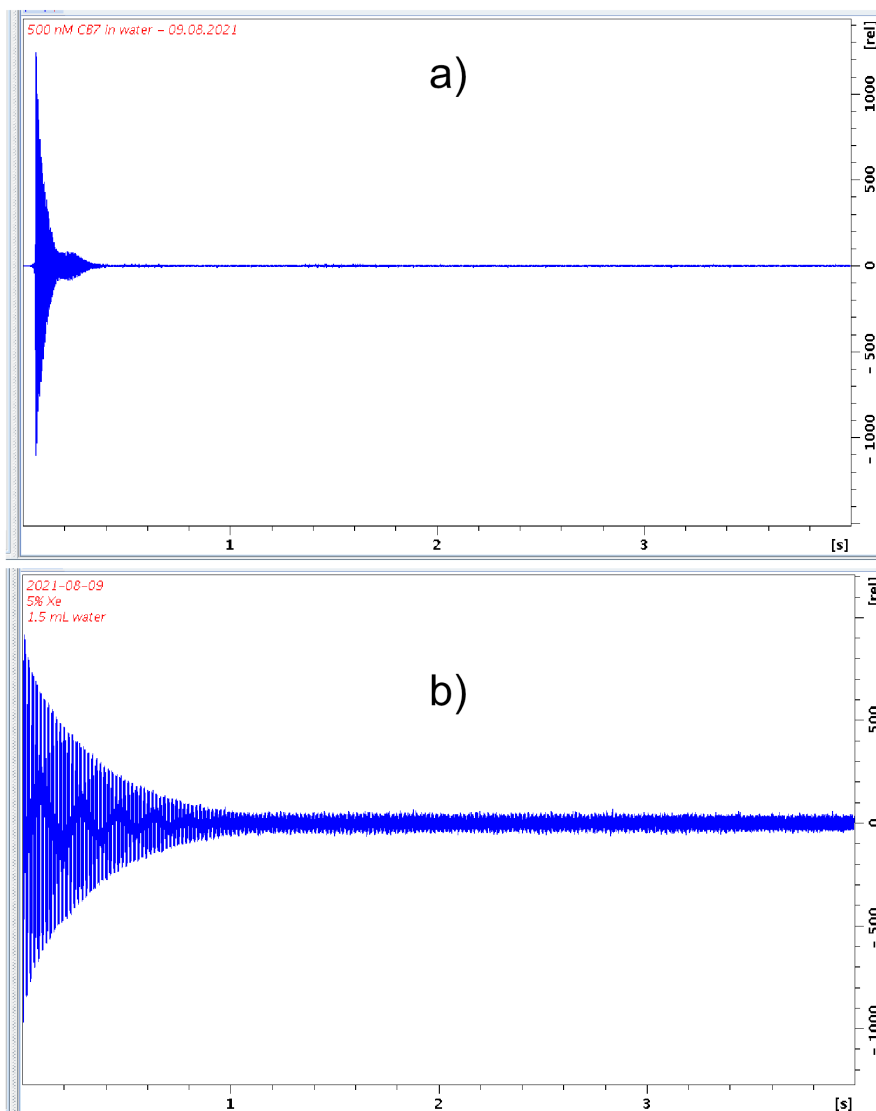


Figure 5.7: The FID illustrating the labile interaction to validates the presence of CB7 in solution. a) In a sample of  $0.5 \mu\text{M}$  CB7 an FID of 600 ms was recorded. b) In a water sample an FID of 2 s was recorded.

### 5.2.5 Chirality of the "blocker"

The supposedly low blocking ability of **1** with regards to the signal at  $-95$  ppm could also be related to a selectivity of the CBn cavity for either the *cis* or *trans* stereo isomers of **1**. A control experiment with the *trans* enantiomer of the blocker was thus performed. The aim of the experiment was testing for complete suppression of the CEST response. Fig. 5.8 presents a comparison between the z-spectrum of a CB7 with the *trans*-blocker (left) and the z-spectrum of a CB7 with the *cis*-blocker (right) where a complete CEST suppression by any of the enantiomers could not be observed. The two spectra do show a small difference in the CEST response with the *cis* enantiomer being a slightly more efficient blocker (it yields a lower CEST response). However, this kind of interpretation should only be seen as a rough qualitative assessment since the difference in CEST responses is about the same as the shot-to-shot noise (shown in Fig. 5.3c). Importantly, after realizing that the bound Xe peak in a CB7 spectrum is from a CB6 impurity the concluded insignificance regarding the chirality of the blocker applies to CB6 and not to CB7. This is in line with expectations since the CB6 cavity is most likely too small to include any of the guest enantiomers, even when *cis/trans*- 1,4-bis(aminomethyl)cyclohexane (TCI chemicals, Eschborn, Germany) were added to 50  $\mu\text{M}$  CB7 solution with CB6 impurity of ca. 4  $\mu\text{M}$  in a 60-fold excess in order to prepare samples.

## 5.3 CAVKA vs. UFZ

In the following section, a comparison between Ultrafast z-spectroscopy (UFZ), as described here [80], and CAVKA is made. The slow stepwise encoding has been addressed in various contexts of NMR spectroscopy by the concept of spatial parallelization [81] to accelerate the data acquisition. It enables encoding of spectral information along one spatial dimension by applying a gradient during preparation and readout. This concept has been used in CEST spectroscopy (called UFZ) for thermally polarized spins [82–84] and for hyperpolarized Xe [80, 85]. Accordingly, the information is stored in a so-called "projection profile", where the magnetization is segmented into many points along the readout dimension. Overall, the method

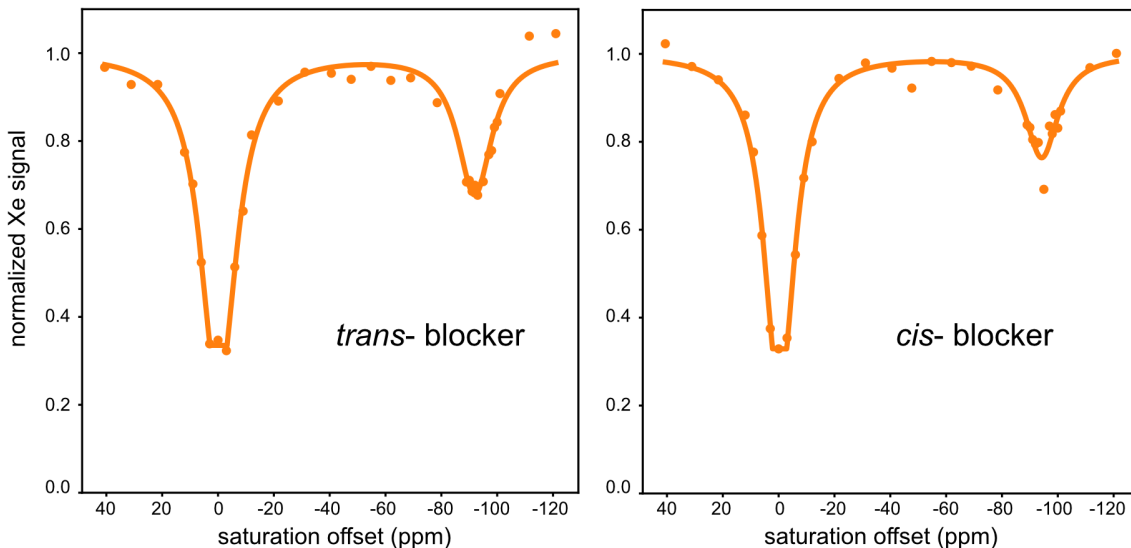


Figure 5.8: Testing the impact of the chirality of **1** on CEST suppression. Nor the *trans* isomer (left) nor the *cis* isomer completely muted the CEST response by vanishing the peak at  $-95$  ppm. Samples contained  $50 \mu\text{M}$  CB7 (aqueous solution) and *cis/trans* 1,4-bis(aminomethyl)cyclohexane in a 60-fold excess ( $3 \text{ mM}$ ). Points are experimental data (ROI-averaged) and solid lines are Lorentzian curve fittings.

becomes faster but the sensitivity is reduced and rather noisy data is produced unless combined with signal averaging or expensive isotope enrichments (where the abundance of the isotope  $^{129}\text{Xe}$  is above 80%, while the natural abundance is 26.4%). The summation of echoes has been suggested in this context to decrease the noise level. For systems with high exchange rates, however, the combination of large chemical shift separations, see Fig. 5.9a-b, and frequent transitions between two Larmor frequencies causes rather strong  $T_{2,\text{ex}}$  effects [48] and turns this averaging strategy rather inefficient. Döpfert et al. [80] defined a stop criterion up to which echo number the signals should be added up before further addition contributes predominantly noise. According to this criterion, echo no. 2 should have at least 41.4% signal intensity of the first echo to be added. Exchange-induced loss of phase coherence can occur with time constant  $\tau$  of a few milliseconds [86] that are comparable to the applied echo time  $TE$ . For  $TE = \tau$ , the second echo is already decayed to 36.8% of the first echo and thus signal summation rather increases the noise. This motivates the search for other ways to speed up the acquisition while maintaining high quality spectra (see

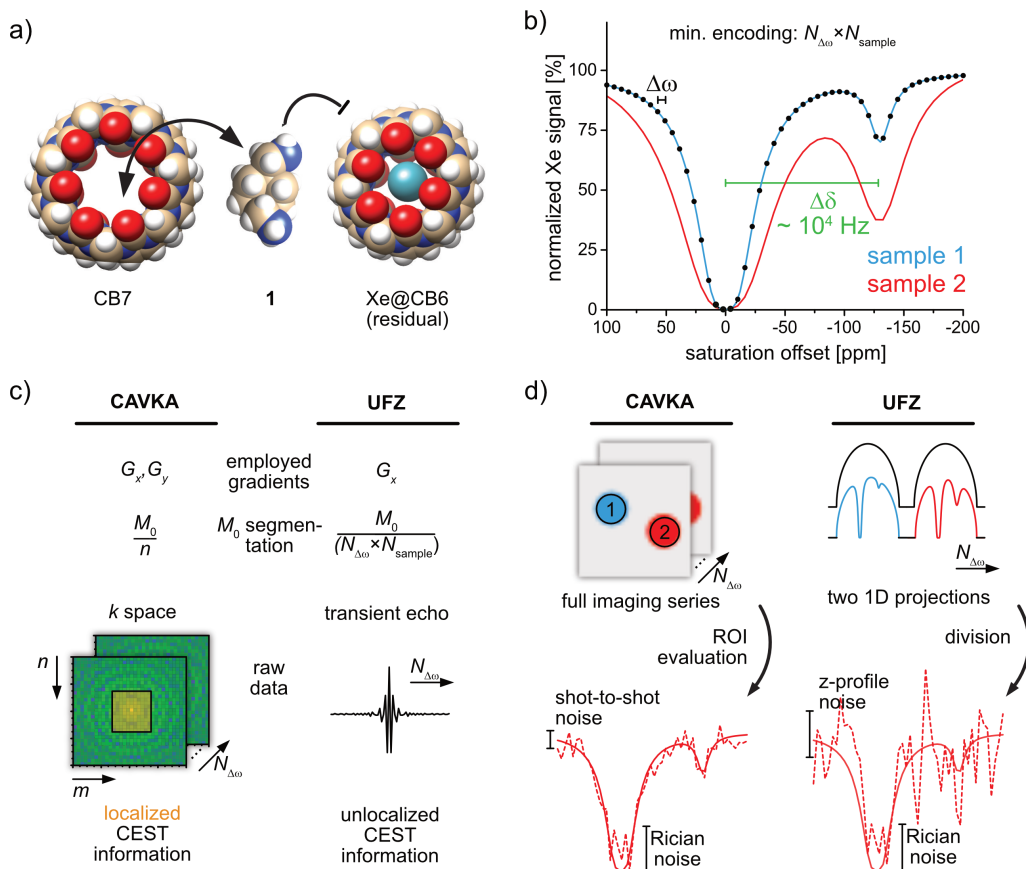


Figure 5.9: Host-guest interactions revealed by CEST spectroscopy and related encoding techniques with acceleration through spatial parallelization. Free Xe is detected after bound Xe has been saturated. a) CB7 provides a cavity and a portal wide enough to reversibly bind **1** (*cis*-1,4-bis(aminomethyl)cyclohexane). Residual CB6 with the smaller portal does not allow easy access for **1**, yet traps Xe long enough to yield a well resolved CEST signal. b) Z-spectrum of multiple samples ( $N_{\text{sample}}$ ). Each spectrum is sampled with a resolution of  $\Delta\omega$  along the spectral dimension and  $N_{\Delta\omega}$  data points. The large chemical shift separation of  $\sim 10^4$  Hz enables access to relative fast exchanging systems. A reduction of the Xe exchange rate reduces the intensity and the width of the CEST response. c) Comparison of the raw data of CAVKA and the UFZ approach. UFZ employs only one gradient and requires high segmentation to cover all data points along the spectral dimension. CAVKA uses reduced segmentation, but encodes a full series of images. The CEST information is restricted to a sub-section of the raw data that can be sampled with increased signal. d) Comparison of the processed data from CAVKA and UFZ. The imaging series in CAVKA allows to define ROIs that yield spectra with low shot-to-shot noise. UFZ yields projection profiles that are divided by each other and carry a relatively high noise level along the spectral dimension due to the high segmentation of the initial magnetization.

section 5.3.1 for more details). The delivery of hyperpolarized nuclei can be done for multiple samples simultaneously for obtaining NMR data from physically separated volumes with different chemical conditions. This can be implemented with separate RF coils [87] or by applying MR imaging concepts [48]. The latter offers flexibility regarding the acceleration strategies that are used to obtain multiple spectra from a series of images as illustrated in Fig. 5.9c-d. Translating the magnetization segmentation step from the chemical shift dimension (as in UFZ) into the domain of image encoding (i.e., spatial frequencies stored in k-space) will yield good spectral quality while still allowing highly accelerated data acquisition.

### 5.3.1 Limits of echo summation

As mentioned above, Döpfert et al. [80] defined a stop criterion up to which echo number the signals should be summed before further addition contributes more noise than signal increase. Echo number  $n$  with signal  $s_n$  should be added only if  $s_n > \left(\sqrt{n/(n-1)} - 1\right) \sum_{i=1}^{n-1} s_i$ . For exponentially decaying echoes,  $\tau/TE$  (i.e., the decay constant in units of the used echo spacing  $TE$ ) is the critical parameter ( $\tau$  is given by  $T_2$  for spin echo train and by  $T_2^*$  for gradient echoes). We arbitrarily assign the first echo signal intensity  $s_1 = 1$  (though this is smaller than the starting magnetization at  $t = 0$ ). Assuming relatively slow sampling or fast decay, i.e.  $TE = \tau$ , then the second echo is already decayed to 36.8% of the first echo. The stop criterion for echo no. 2 requires that it should at least be 41.4% of the first echo to be added. Thus,  $TE = \tau$  yields best signal for no further addition. The ideal case for sampling the echoes infinitely faster than the decay means that each signal  $s_i$  contributes almost  $s_i \sim 1$ . The sum of the preceding  $n - 1$  echoes is  $n - 1$  and thus the upper limit that the  $n$ -th contribution yields after normalization by the previous sum is given by  $(n - 1)^{-1}$ . The "test criterion", shown in Fig. 5.10 can not reach the yellow area but must stay outside the red area. For  $\tau = 2 \cdot TE$ , summation up to  $n = 3$  is beneficial. For  $\tau = \{5, 10, 50\} \cdot TE$ , summation up to  $n = \{6, 13, 63\}$  improves the signal. We thus see that rapidly decaying signals like those in fast exchanging systems ( $\tau < 10$  ms for gas vesicles as seen by the FID decays in the FA calibration [86]) suffer from strong limitations with regard to efficient echo accumulation.

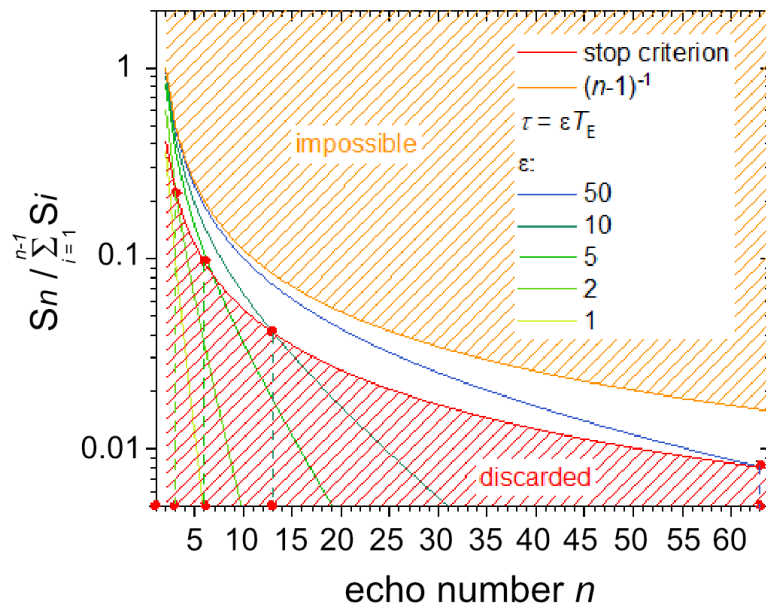


Figure 5.10: Signal improvement by summation of echoes. Red area under the curve  $\sqrt{n/(n-1)} - 1$  is where echo summation contributes noise rather than signal. Yellow area above the curve  $1/(n-1)$  is impossible due to the non-zero scan time. Curves in green and blue with different values of the critical parameter  $\tau/TE$  intersect the red curve to show the maximal number of echoes that should be summed to improve the signal. Data is simulated.

### 5.3.2 Further segmentation considerations

The z-spectra obtained by gradient echoes as shown by Döpfert et al. [80] were quite quickly noise dominated. They also included a blurring related to the sharp edges and had a small dynamic range where the Rician noise level relatively soon impaired the information in the same range of frequencies that CEST-induced signal loss started to appear. For fast decaying signals and a low starting magnetization, there are important limitations for segmenting the available magnetization, as in UFZ, into pieces along the chemical shift dimension:

- only a rather small part of both the starting magnetization and the host actively participates in the CEST effect (those with the "matching" frequency along the gradient direction);
- in the typical implementation with cylindrical NMR tubes, different sections of the CEST spectrum are encoded with different reference magnetization, in other words the shape of the reference z-spectrum depends on the shape of the phantom and/or the shape of the excitation pulse along the direction of the applied gradient. Low magnetization levels at the edges are dominated by Rician noise, thus the "valuable" CEST information should be concentrated towards the center.
- no redundancy exists in the data.
- equidistant sampling is applied along the saturation frequency (CEST) dimension, thus selectively more dense sampling around ranges of interest (the spectrum peaks) is not possible. The noise along the readout dimension after FT can be pretty high in UFZ. Contrary, the shot-to-shot noise along the saturation frequency dimension for conventional CEST encoding with the polarizer operating in continuous flow mode is rather low (e.g., less than 0.56% is possible [88]). Working with natural abundance  $^{129}\text{Xe}$  and choosing continuous flow operation has the advantage of i) being cost effective and ii) providing stable magnetization conditions over an extended period of time for comparing different spectra. It comes, however, with reduced starting magnetization

(compared to enriched  $^{129}\text{Xe}$  and cryo-separation), but this can be overcome by carefully choosing certain dimensions for signal averaging, identifying signal redundancies and segmenting the starting magnetization i) along an "uncritical" dimension and ii) into fewer steps. It should thus be favorable to maintain step-wise (but not equidistant) encoding along the  $\Delta\omega$  axis with replenishing of the magnetization for each saturation offset and to implement acceleration for one or the other encoding dimensions. Instead of segmenting the magnetization into at least 64 pieces of variable amplitude along the saturation offset dimension, it can be divided into 32 equal segments to optimize encoding along the spatial dimension via the VFA approach. Along the spectral dimension, no nuclei will be affected at all by RF saturation for certain offsets, but for the important frequencies (around the peaks), all nuclei and hosts participate in the CEST mechanism and thus make most efficient use to encode the CEST effect, even for small host concentrations. Transferring the magnetization segmentation step from the chemical shift dimension (where the noise level would otherwise seriously impair the quality of the z-spectrum) into the domain of spatial frequencies (k-space) for imaging helps to spread the noise across all pixels in image space.

## 6 Denoising of hyperpolarized $^{129}\text{Xe}$ MR images

In this chapter, two denoising methods, namely principal component analysis and wavelets, are applied to hyperpolarized Xe MRI.

### 6.1 Introduction

Denoising is the reduction of the noise level that accompanies a signal. Many digital spectrometers, seismometers and MRI scanners process signals that are contaminated with noise. The two main sources of noise in MR images are the electronics (hardware) and dielectric and inductive losses in the sample [89, 90]. The noise impairs image quality, can mask fine details and it also leads to errors in imaging-based signal quantification. These effects create the need for denoising methods.

Noise removal in MRI can be done in a number of ways, for example by cooling of the imaging hardware (to reduce noise from a thermal source) [91], by signal averaging (which has already been discussed extensively throughout this thesis), or by image domain filtering (Gaussian filter, Wiener filter and others [92]). Principal component analysis (PCA) and wavelets are the two methods used for denoising in the following chapter.

PCA and wavelets can be considered as spectral decomposition methods: spectral in the sense that there is a set of functions  $\{g_i\}$  that is used to give the signal a representation in the form of  $\sum_i a_i g_i$ , where  $a_i$  are coefficients (amplitudes) for the functions in the set (the spectrum). Denoising can be achieved by using a reduced number of spectrum functions, like in PCA, or by setting some of their coefficients to zero, like in wavelets. The spectrum constituents in PCA are eigenvectors of the signal-related covariance matrix and in wavelets these are the wavelet functions.

Tuning of parameters in these spectral methods is important for tailoring them to the type of MRI data that is to be denoised and serves the final goal of achieving optimized SNR while sustaining relevant image features. PCA is applied on k-space data and the number of principal components (pc) needs to be tuned, whereas wavelets are applied on image space data and the threshold value for zeroing out wavelet coefficients is tuned, as well as the type of thresholding procedure (soft/hard).

The denoising method of PCA demands a series of images for its implementation. It uses the multiple images to identify redundancies in the data and removing these redundancies facilitates the removal of noise. Wavelets, on the contrary, takes a single image as input and the removal of noise is done by local averaging of pixel areas with only small variation. However, for some imaging applications a series of images is anyway acquired, thus both denoising methods could be used without prolonging the image acquisition time.

Normalization of the data is needed for some denoising methods to adjust the noise properties to the requirements of the method. In wavelets denoising, calculation of the SURE (Stein Unbiased Risk Estimate) threshold assumes a noise level of 1 and the images are normalized to respect this. To this end, the noise level has to be estimated as a preliminary step. PCA denoising also includes a preliminary step which is the centering of the images from the series to have a zero mean pixel-wise.

## 6.2 Principal component analysis (PCA)

Principal component analysis is a dimensionality reduction technique. It takes repetitions of multivariable information as input and constructs new variables as a linear combination of the original ones. The criterion for constructing these new variables is that the change of the information along them is maximal. If this process ends successfully, the number of the new variables would be lower than the number of the initial variables. In image data each pixel is considered as one variable and its repetitions come from obtaining a series of images. If the image resolution is  $p$  and the number of images is  $n$ , the data matrix  $X$  has dimensions  $n \times p$ , where each row of  $X$  is formed by 2D image that was reshaped to a one dimensional array (a vector). The data matrix is assumed to be centered (i.e., the mean value of each column is zero). If this is not true, it could always be realized by subtracting each column mean from the entries of the column. The covariance matrix of the data is calculated by  $X^* X$ , where  $*$  denotes transpose and complex conjugate (division by  $n - 1$  is omitted here since it is irrelevant to the derivation). A new set of variables is sought as a linear combination of the original variables, thus a set of weights  $w_1, w_2, \dots, w_p$  (each is a column of  $p$  entries in a matrix  $W$ ) is defined and the data matrix written with

the new variables is given by  $XW$  (each column of  $XW$  has the repetitions of one new variable). In order to find the new variables (or just the weights that define the new variables),  $XW$  is subjected to the constraint that the variance of this matrix should be maximal and to an additional constraint that the weights are unit vectors,  $\|w_i\|_2 = 1$ . This is posed as an optimization problem:

$$\begin{aligned} & \arg \max_{\|w\|=1} \{(XW)^* XW\} \\ & \arg \max_{\|w\|=1} \{W^* X^* XW\} \end{aligned}$$

and since weights are unit vectors, this can also be written as,

$$\arg \max_{\|w\|=1} \left\{ \frac{W^* X^* XW}{w^* w} \right\}.$$

The last expression can be recognized as the Rayleigh quotient [93]. It can be shown that the maximum is found when the weights in (the columns of)  $W$  are assigned to the eigenvectors of  $X^* X$ . Additionally, the eigenvalues give the values of the Rayleigh quotient for the respective eigenvectors, thus the eigenvectors that correspond to the largest eigenvalues define new variables for which the variance change along them is maximal. Taking the first  $l$  eigenvectors, where usually  $l \ll p$ , provides the dimensionality reduction. After obtaining  $W$ , the PCA reconstruction matrix is calculated by  $XWW^*$  which yields a matrix with dimension  $n \times p$  as the original data matrix. It can be shown that the new variables are an orthogonal set, thus the transformation to the new variables decorrelates the original variables or in other words reduces the redundancy in the data [94]. Moreover, since the new variables are orthogonal, they are referred to as the directions of the PCA coordinate system. The weights vectors that define the new variables are called the principal components (pc) and the values of the new variables (the projection of the data on the new variables) are called scores.

PCA implementation in this chapter involved singular value decomposition (SVD). In SVD, the data matrix  $X$  is decomposed as  $X = USV^*$ , where  $U$ ,  $V$  are orthonormal matrices (their columns are an orthonormal set) with dimensions  $n \times r$  and  $p \times r$ , respectively. Thus,  $U^*U = I$ ,  $V^*V = I$ , where  $I$  is the identity matrix.  $S$  is a diagonal matrix with dimensions  $r \times r$ . To implement PCA, one seeks for the eigenvectors of the covariance matrix  $X^* X$  and it can be shown that these eigenvectors are equal to

the columns of  $V$ . Thus, obtaining  $V$  replaces solving for  $W$ . In order to derive this connection let the covariance matrix be written in terms of the SVD decomposition,

$$X^*X = (USV^*)^*USV^* = VS^*U^*USV^*,$$

since  $U^*U = I$  and  $S$  is diagonal (therefore  $S^*S$  is also diagonal with the element-wise multiplication of  $S^*$  and  $S$ ) then

$$X^*X = VS^*SV^*.$$

This can be identified as the diagonalization of  $X^*X$  where  $V$  is the diagonalizing matrix that according to the diagonalization theorem [95] has in its columns the eigenvectors of  $X^*X$ . Not any arbitrary matrix can be diagonalized, however the covariance matrix is symmetric and thus, according to the diagonalization theorem, can be diagonalized. Using SVD terms, the data matrix with the new variables ( $XW$ ) and the PCA reconstruction matrix ( $XWW^*$ ) can be written as,

$$\begin{aligned} XW &= USV^*V = US, \\ XWW^* &= USV^*VV^* = USV^*. \end{aligned}$$

The eigenvalues of  $X^*X$  are, in SVD terms,  $S_1^2$  (the elements in the diagonal of  $S$  squared). The PCA reconstruction is done using the first  $l$  columns of  $V$  the same way it was done with  $W$ .

### 6.3 The discrete Wavelet transform

The wavelet decomposition begins by giving a representation to a signal  $f(x)$  (assuming  $x \geq 0$  without loss of generality) by using a series of integer-shifted step functions (also called scaling functions)  $\{\phi_m(x)\}$ ,  $m = 0, 1, \dots, M - 1$ , where  $m$  are the shifts and  $M$  is the signal length. They are functions of a constant value over a narrow domain (support) and of zero-value elsewhere, each allows representation of the signal value in one spatial location:

$$f(x) = \sum_{m=0}^{M-1} a_m \phi(x - m),$$

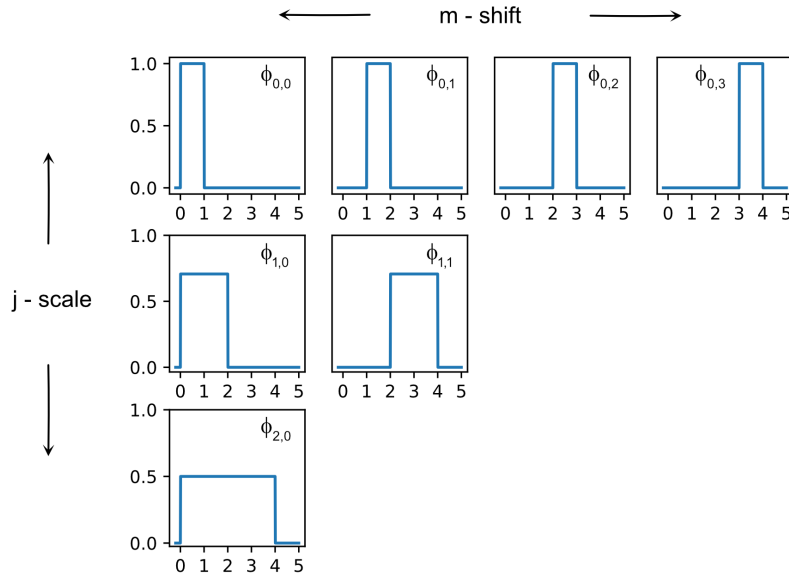


Figure 6.1: Scaling functions  $\phi_{j,m}(x)$ .  $m$  sets the shift of the scaling functions, e.g., first row  $m = 0, 1, 2, 3$ .  $j$  sets the support (width) of the scaling functions, e.g., last row  $j = 2$ .

$$\phi(x) = \begin{cases} 1, & \forall x \in [0, 1) \\ 0, & \text{otherwise} \end{cases}.$$

An approximation for this initial representation is then built by using step functions with a support that is twice as wide for each following interval and thus the resolution is reduced 2-fold. This is known as the dyadic decomposition (or multiresolution analysis) and it takes the approximation from one level (scale)  $j$  to the next coarser one  $j + 1$ . In each level  $j$  ( $j \in \mathbb{Z}$ ) the step functions are constructed according to

$$\phi_{j,m}(x) = 2^{-j/2} \phi\left(\frac{x - m}{2^j}\right).$$

The information that is needed to move back to a finer level is represented by another series of shifted functions (called the wavelet functions)  $\{\psi_m(x)\}$ . Each allows representation of the difference between the approximations of two levels in one spatial location. This difference takes the form  $\sum_{m=0}^{M-1} w_{j,m} \psi_{j,m}(x)$ , where  $w_{j,m}$  are the coefficients of the wavelet functions at level  $j$ . The 'Haar' wavlet [96] is an example

which is one of the few with an analytic form:

$$\psi(x) = \begin{cases} 1, & \forall x \in [0, 1/2) \\ -1, & \forall x \in [1/2, 1) \\ 0, & \text{otherwise} \end{cases}.$$

Shifting and dilating the Haar function is according to

$$\psi_{j,m}(x) = 2^{-j/2} \psi\left(\frac{x-m}{2^j}\right).$$

For other wavelet functions, the wavelet coefficients are obtained by conjugate mirror filters [97].

Wavelet decomposition of an image demands a generalization of the above description to 2D, which is done easily via a tensor product [97]. It yields 4 matrices in each level of decomposition, 1 approximation matrix (with half the resolution in each direction) and 3 wavelet coefficients matrices that store the difference information in three directions: horizontal, vertical and diagonal (with same dimensions as the approximation matrix). Areas in the image where the pixel values do not change a lot yield wavelet coefficients of low magnitude. On the contrary, edges in the image correspond to high magnitude wavelet coefficients. Keeping the large wavelet coefficients and neglecting (assigning to zero) the rest was shown [98,99] to produce good approximations of the original image while reducing the amount of information needed to represent it. This is known as the sparsity of the wavelet domain. Selective vanishing of wavelet coefficients is termed thresholding and two types exist. 1) Hard thresholding: neglecting all coefficients with a value under the specified threshold and keeping the other coefficients unchanged. 2) Soft thresholding: neglecting all coefficients with a value under the specified threshold and reducing the remaining ones by the value of the threshold.

Several ways were suggested to determine the threshold value [100–103], some are adaptive to the signal that is being decomposed and others use general noise properties to set it. The universal threshold [100]  $\lambda = \sigma\sqrt{2\log n}$ , where  $n$  is the signal length (the image resolution for images) and  $\sigma$  is the standard deviation of the noise that corrupts the signal, is the solution of the optimization problem that finds, under

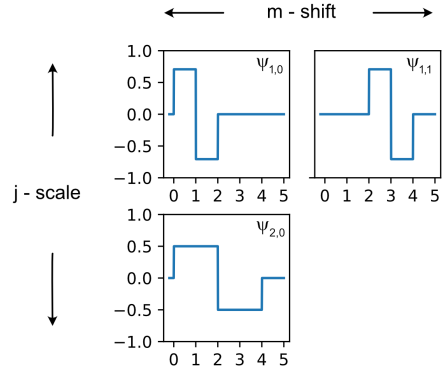


Figure 6.2: Haar wavelet functions  $\psi_{j,m}(x)$ . The wavelet functions retrieve fine details information to the approximation in level  $j$  from the approximation in level  $j - 1$ .  $m$  and  $j$  has the same role as in Fig. 6.1

certain assumptions, a threshold value that minimizes the error between the original signal and its wavelet reconstruction. The term reflects dependency only on the signal length and noise level. It is easily found (without any further computations on the wavelet coefficients) and was developed with independent, zero mean and normally distributed noise and it has an increasing accuracy as  $n \rightarrow \infty$  (asymptotic behavior). Another type of threshold  $\lambda$  is SURE (Stein Unbiased Risk Estimate) [101, 104]. It is also the solution of the optimization problem mentioned above, but with adaptivity to the data degree of smoothness. To obtain the SURE threshold, one seeks the value  $\lambda$  that minimizes the SURE function:

$$SURE(\lambda, w) = n + \sum_{i=1}^n \min(|w_i|, \lambda)^2 - 2 \cdot \#\{i : |w_i| < \lambda\},$$

where  $w_i$  are wavelet coefficients and  $\#$  is the cardinality (number of wavelet coefficients that are smaller than  $\lambda$ ). It can be shown [102] that the solution can be obtained by sorting the wavelet coefficients in ascending order and then plugging them into the SURE function. The coefficient that gives a minimal value to the SURE function is the desired solution. These additional processing steps make the SURE threshold harder to obtain than the universal threshold, but this also makes it more adaptive to the signal as it has a dependency on the wavelet representation of the signal rather than just on its length. SURE threshold cannot exceed the universal threshold amid

to its mathematical derivation. It also assumes noise level of 1 and thus the signal must be normalized accordingly.

The thresholding procedure can be applied on the wavelet coefficients matrices of the first decomposition level of the signal, or it can be applied iteratively on multiple levels. The latter involves further decomposition of the first level approximation matrix to a coarser approximation and 3 wavelet coefficients matrices. The wavelet coefficients matrices of the first level are not further decomposed. This is known as the Mallat way of wavelet decomposition [97].

## 6.4 Results and discussion

In the PCA section (6.4.1) two experimental datasets were used, one of an averaging imaging series and the second of a CEST imaging series. In both datasets, experiments were done in a double phantom with H<sub>2</sub>O in the outer compartment and CrA (10  $\mu$ M in H<sub>2</sub>O + 0.2% DMSO) in the inner compartment. The averaging series was acquired with a FLASH sequence and the CEST series with a RARE sequence. PCA worked for both types of sequences.

In the averaging dataset, scans were performed using a modified 2D FLASH sequence to include a preceding CEST preparation block and a VFA scheme for the excitation pulses. <sup>129</sup>Xe imaging parameters were:  $TE = 5.6$  ms,  $TR = 12.2$  ms,  $FOV = 12 \times 12$  mm<sup>2</sup>, slice thickness = 20 mm,  $BW = 4$  kHz, encoding order = "centric", matrix (image resolution) =  $32 \times 32$ . The xenon fraction was 5% of the gas mixture delivered to the sample. Bubbling was performed for 10 s and additional 4 s were added afterwards for allowing potentially generated gas bubbles to collapse. All images were acquired with an off-resonant saturation at 361.5 ppm (40 kHz), for 10 s and 20  $\mu$ T to include the full CEST timing.

In the CEST dataset, scans were performed using a modified RARE sequence with a CEST preparation block. <sup>129</sup>Xe imaging parameters were:  $TE = 10.7$  ms,  $TR = 10.35$  ms,  $FOV = 10 \times 10$  mm<sup>2</sup>, slice thickness = 20 mm,  $BW = 4$  kHz, encoding order = "centric", matrix(image resolution) =  $32 \times 32$ . The xenon fraction was 5% of the gas mixture that was delivered to the sample. Bubbling was performed for 10 s and additional 4 s were added for gas bubbles to collapse. A saturation pulse

of 10 s and 6  $\mu\text{T}$  was applied at 23 offsets between  $-204$  and 60 ppm ( $-22584$  and 6642 Hz) in 12 ppm (1328.45 Hz) steps relative to the resonant frequency of xenon at water (that was set to zero). This range is designed to cover the Xe@H<sub>2</sub>O (at 0 ppm) and Xe@CrA (at  $-132$  ppm) resonance frequencies. The RARE factor was equal to the number of phase encoding steps.

PCA was implemented with Python 3.8 by using the SVD (singular value decomposition) function of the linalg (linear algebra) submodule of the NumPy library. This implementation was found to be 20-fold faster than an alternative option of using the function eig (also from the linalg submodule) that finds the eigenvalues and eigenvectors of the covariance matrix of the data. PCA was applied to complex-valued k-space data in a component-by-component manner. SNR in images was calculated as the mean of the signal ROI (a circle with a radius of 10 pixels) over the standard deviation of the noise ROI (a circle with a radius of 4 pixels) located in the top left corner of every image.

In the wavelets section, (6.4.2) two experimental datasets were used, one with a low and another with a higher SNR condition. In both datasets experiments were done in a double phantom with H<sub>2</sub>O in the outer compartment and CrA (10  $\mu\text{M}$  in H<sub>2</sub>O + 0.2% DMSO) in the inner compartment. Scans were performed using a modified 2D FLASH sequence to include a preceding CEST preparation block and a VFA scheme for the excitation pulses. <sup>129</sup>Xe imaging parameters were:  $TE = 5.6$  ms,  $TR = 12.2$  ms,  $FOV = 12 \times 12$  mm<sup>2</sup> ( $10 \times 10$  in the high SNR dataset), slice thickness = 20 mm,  $BW = 4$  kHz, encoding order = "centric", matrix (image resolution) =  $32 \times 32$ . The xenon fraction was 5% of the gas mixture delivered to the sample. Bubbling was performed for 10 s ( 15 s in the high SNR dataset) and additional 4 s (3 s in the high SNR dataset) were added afterwards for gas bubbles to collapse. All images were acquired at an off-resonant saturation at 361.5 ppm (40 kHz), for 10 s and 20  $\mu\text{T}$ .

The discrete wavelet transform was implemented with Python 3.8 by using the PyWavelets library [105] and included the use of the functions 'dwt2', 'threshold' and 'idwt2' for the discrete wavelet transform, for the thresholding procedure and for the inverse discrete wavelet transform, respectively. All wavelet transformations were

done with the Haar wavelet function and all thresholding was done as soft thresholding, since hard thresholding was less efficient. Complex-valued image data was directly input to processing pipeline. Upon specifying a threshold value, thresholding was done according to the magnitude value of the (complex) wavelet coefficients.

#### 6.4.1 PCA denoising of k-space data

PCA requires multiple images as an input. At first, replicates of a single image were used (an imaging series for averaging) to test the denoising effect of PCA. The k-space data of this imaging series was used to find the PCA directions (principal components) and the first direction (only) was taken to project the original data into the PCA system of coordinates. Fig. 6.3 (top) shows one of the k-space replicates before and after the PCA transformation that was based on 15 images. It can be seen how the pixel values in the periphery of k-space is reduced in the left image (after PCA) versus the right (original k-space). Pixel values in the periphery of k-space are associated with noise [26] and thus this demonstrates qualitatively that PCA achieves a denoising effect.

Next, the length of the imaging series was checked for its impact on the denoising ability. This was done by applying PCA, which was based on imaging series of lengths 1, 5, 10, 15, 20, ..., 50, to one k-space, then Fourier transforming the denoised k-space to get the corresponding image and finally measuring the SNR in this image, Fig. 6.3 (bottom) shows the results in a plot of SNR vs. the length of imaging series. Using series with up to 10 images yielded small denoising effect with SNR values that are under 11, using 15-30 images yielded roughly constant SNR value of ca. 13 and series with length over 30 yielded SNR of more than 29. The SNR value in one image from a set of 50 individual images before PCA denoising was 6.9 (averaged SNR value from the 50 replicates), this value was also used as the initial SNR value (corresponding to length of 1) in plotting the gray dashed line in Fig. 6.3. The graph at the bottom of Fig. 6.3 shows that more than 30 images are needed in order to achieve the higher SNR increase of ca. 4.2-fold and with series of shorter length, the SNR increase is only 1.9-fold at best.

Thus, it can be concluded that for an averaging imaging series PCA, as a denoising

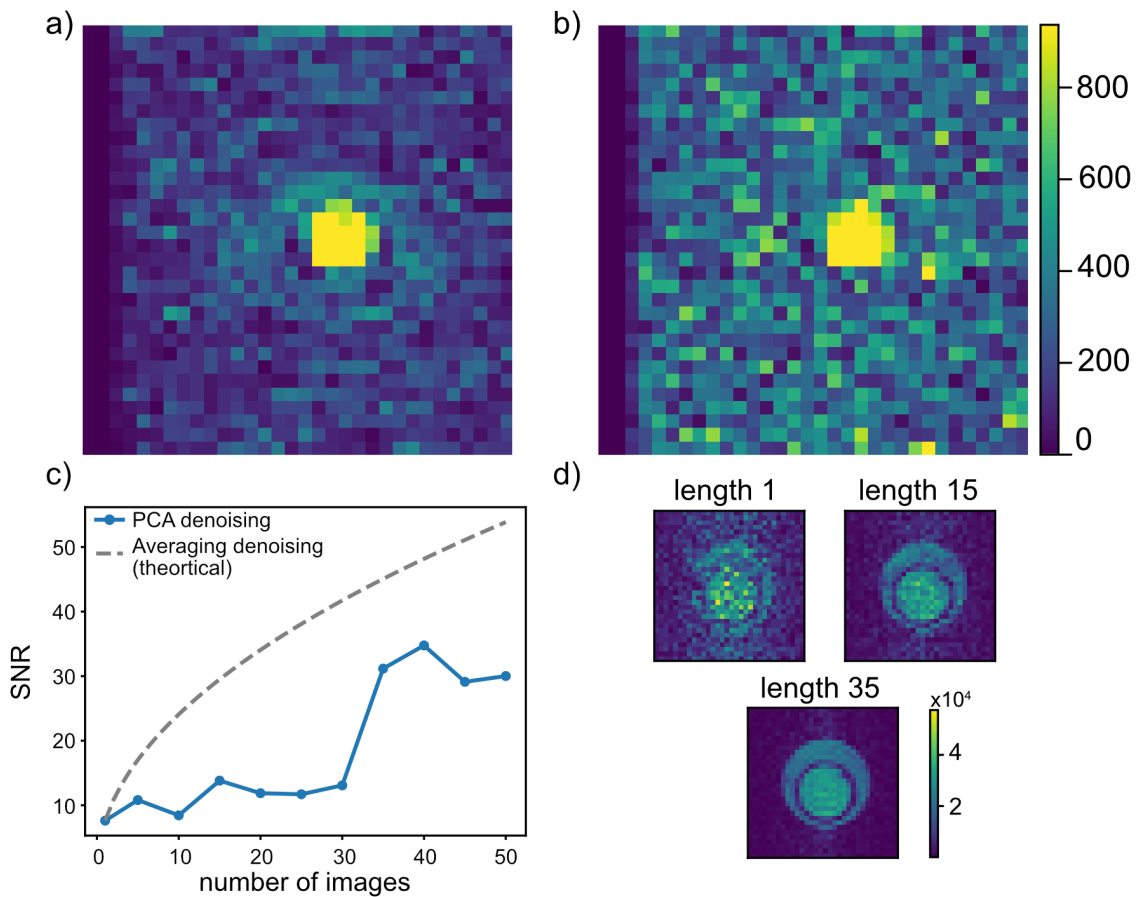


Figure 6.3: PCA denoising of an averaging series. a-b) k-space before (b) and after (a) denoising. A qualitative demonstration of the reduced pixel value at the periphery of k-space by the PCA transformation. Color maps were set with an upper limit of 20% of the maximal pixel value to allow good visibility of the k-space periphery. c) SNR as a function of the length of the averaging series. SNR was measured in image space (Fourier transformed k-space). Gray dashed line shows the SNR that would be achieved by averaging for comparison purposes. d) PCA reconstructed images from averaging series of lengths 1, 15 and 35.

method, would have a higher impact when more than 30 replicates are included. Additionally, this plot clearly shows that averaging is more efficient as a denoising method than PCA by providing higher SNR for each length (of the imaging series) that was tested. However, averaging can only be used to denoise one image, the averaged image, from a series of its replicates. PCA, on the contrary, can be used to denoise images from a dynamic contrast imaging series (like CEST) and thus increases the SNR (although not as much as averaging) without spending the additional time for acquiring the images replicates. The efficiency of averaging versus PCA for denoising hyperpolarized xenon images was also discussed in [106]. There, PCA was applied, unlike in this work, to image space (magnitudes) data. It was concluded, that PCA can be more efficient when many different saturation frequencies are desired.

SNR in PCA-denoised images was also checked upon varying the number of principal components (pc), Fig. 6.4a shows the results (from a PCA transformation based on 15 images). The graph has a decreasing trend. Additionally, a relatively large SNR reduction is displayed in the transition from 1 to 2 pc. The observed trend is in line with expectation since the PCA reconstruction is getting closer to the original image and includes more of the undesired image noise and by that the SNR declines as the number of pc grows [107].

Another criterion that is considered regarding the number of pc is the value of the eigenvalues. Fig. 6.4b shows the values of all eigenvalues of the system (with a total number as the number of images in the imaging series) for each of the real/imaginary components of the data. The eigenvalues are ordered from the largest to the smallest as they are given in this order by the PCA procedure. The decay rate of the eigenvalues appears as more or less constant (a linear decay with a constant slope) for the first 14 eigenvalues and a drop in value is then seen for the last eigenvalue. This kind of decay rate does not provide a clear cutoff to the number of pc that should be used, since the criterion [108] specifies to keep the largest eigenvalues up till the one with a recognizable drop in value. However, in Fig. 6.4b the drop comes only at the last eigenvalue and keeping all eigenvalues misses the aim of reducing the dimensions of the data in order to achieve denoising.

Finally, the number of pc that are needed for reconstructing CEST contrast was

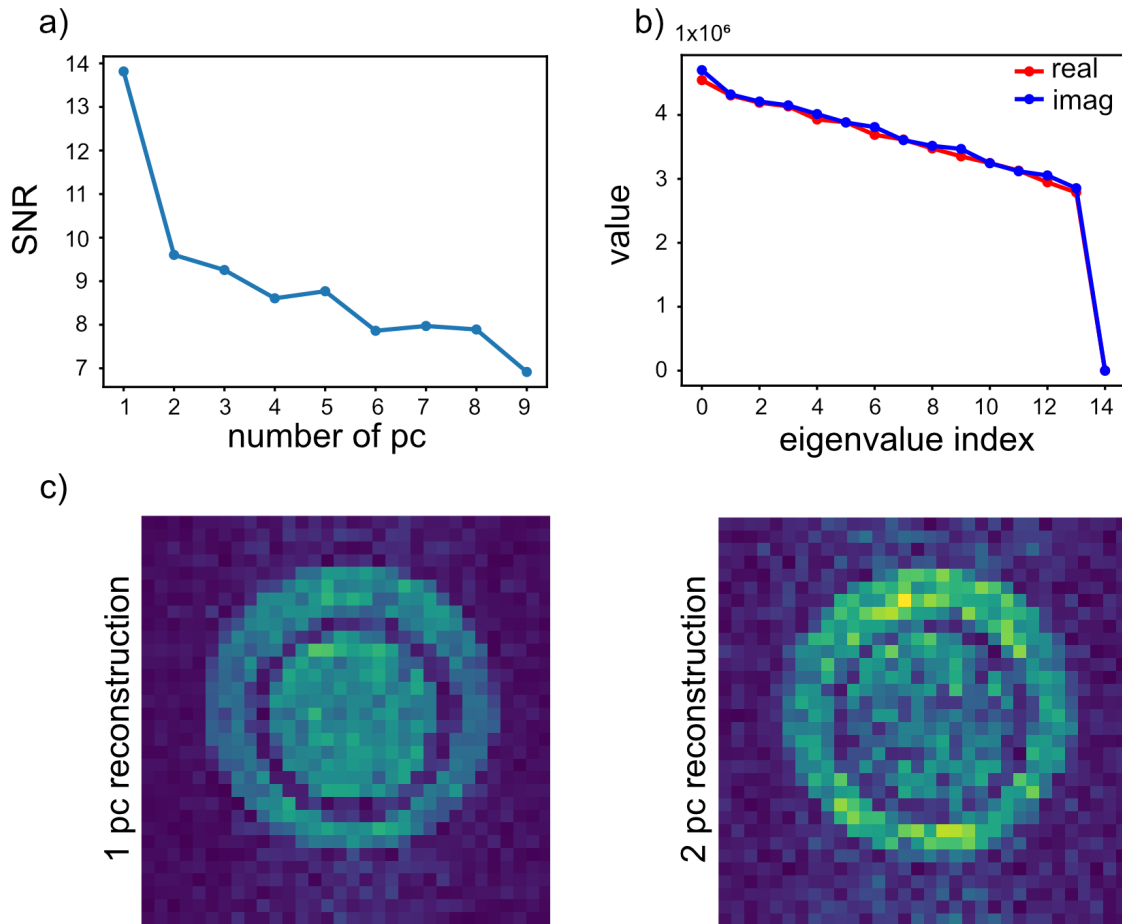


Figure 6.4: Optimal number of principal components (pc) to achieve maximal SNR and to reconstruct CEST contrast. a) SNR vs. the number of included pc showing a decreasing SNR trend with increasing number of pc. b) Eigenvalue decay rate does not provide clear criterion to the number of pc. c) Impact of the number of pc on capturing CEST contrast, contrast between the compartments is reconstructed with 2 pc (right) whereas with 1 pc it is lost (left).

checked. To this end, PCA was applied to a CEST imaging series. Fig. 6.4c shows the results of a PCA transformation that is based on 23 images (the length of the CEST imaging series). It displays the PCA-denoised images at the on-resonant frequency of Xe@CrA, where a contrast between the phantom compartments should appear. Using only 1 pc to reconstruct the image leads to a loss of the CEST contrast (left image) that was present in the original image, whereas using 2 pc successfully captures the CEST contrast (right image). The first pc only represents the overall geometry whereas using a higher number of pc ( $\geq 2$ ) also captures the CEST contrast.

Thus, it is concluded that 2 pc are the optimal number of pc in this case, since a larger number would result in lower SNR and a smaller number would not capture the important feature of CEST contrast. Table 6.1 provides the SNR values in on- and off- resonant images before and after PCA denoising, the pc were calculated from a CEST imaging series (length of 23) and 2 of them were used. The eigenvalue decay rate analysis (like in Fig. 6.4b) for the CEST imaging series showed that 2 pc are required for the real component by presenting a clear drop in value for the eigenvalues that follow it. By that, this analysis supports the number of pc that was also needed for correct contrast reconstruction (Fig. 6.4c). For the imaginary component, however, the decay rate plot showed 1 pc is sufficient. Nevertheless, since using unequal number of pc for the real and imaginary components was not considered, 2 pc were used for each component.

In the previous work [106] where PCA denoising was applied to image space (magnitudes) data of hyperCEST imaging series, the selected number of pc was also two. The arguments for this selection were: 1) two CEST agents were used each in one compartment of the double phantom. Thus, the change in pixel intensity along the CEST series was expected to be mainly in two groups of pixels, those of the inner and the outer compartments. 2) A plot of the decay rate of the eigenvalues showed that most of the data variance is captured by the first two pc. This was also confirmed by producing the PCA-reconstructed CEST series with 3 pc and observing lower SNR. Reconstruction was also done with 1 pc which led, as in this work, to incorrect display of contrast for the inner compartment. Following the same logic as in the first argument, 2 pc are again expected here since two different signatures are

Table 6.1: SNR comparison between original and PCA-denoised images (of the double phantom) at off- and on-resonant saturation frequencies. PCA transformation was based on 23 images of a CEST imaging series and 2 principal components were used.

	Original	PCA denoised
Off-resonant image	9.21	39.35
On-resonant image	5.09	7.56

observed along the spectral dimension: one with only direct saturation and one with a defined CEST response.

Additionally, the SNR increase reported in the same previous work was 2.2 for the off-resonant image, whereas in this work it is 4.3. Possible explanation to the higher denoising effect achieved when applying PCA to k-space data is the connection between image space and k-space. Accordingly, each pixel in image space is related (by the discrete Fourier transform) to the sum of all the data points of k-space. Therefore, denoising k-space leads to a cumulative denoising effect of image space data that is higher than the direct PCA denoising of image space data.

#### 6.4.2 Wavelet denoising of image space data

Wavelet denoising was applied to images that were normalized to have a noise standard deviation (SD) of 1 by estimating the noise SD inside a noise ROI (in the FT-reconstructed image) and dividing the image (pixel-wise) by the estimated SD value. This was done since finding the SURE threshold demands a signal (image) with a noise SD of 1. On the contrary, the universal threshold can be calculated from a non-normalized image, but the SD of the noise is needed for its calculation. Therefore, the SD was calculated and was additionally used to normalize the image which made the thresholding procedure in both cases (SURE and universal) more uniform. MRI allows for direct estimation of the noise SD. When this kind of estimation is not possible, statistical methods in the wavelet domain can be used. For example in [109], the noise SD of seismic signals is estimated by  $\sigma = \text{median}(|w|)/0.6745$ , where  $w$  are the wavelet coefficients at the finest scale. Another test for estimating the noise SD in the images as described in [110] was done. Accordingly, the noise was treated as Rice

distributed with a low SNR (which makes it Rayleigh distributed) and the SD was estimated according to  $\sqrt{2/\pi} \cdot \overline{X}_{\text{noise}}$ , where  $\overline{X}_{\text{noise}}$  is the mean of the noise. However, this did not yield a correct image after the denoising process.

At first, wavelet denoising was applied to  $^{129}\text{Xe}$  MR images by performing one level decomposition and thresholding of the wavelet coefficients matrices of one image (at an off-resonant frequency) from a double phantom experiment. Two datasets were tested with a low and a higher initial SNR value (as shown in Table 6.2). In Fig. 6.5 a-b, an image before and after denoising from the higher SNR dataset is shown. The denoising effect is clearly visible, especially in the phantom inner compartment and outside to the phantom compartments. It appears as a more homogeneous distribution of pixel values. SNR was increased 1.5-fold by the wavelet denoising, values are provided in Table 6.2. Wavelet denoising did not perform better on the low (initial) SNR image than on the high SNR image. The values in Table 6.2 show roughly the same SNR increase for both SNR regimes. However, when the initial SNR is very low, the wavelet method failed in recovering the signal. This was tested by applying wavelet denoising on an image from the GVs dataset and trying to recover the phantom geometry, as appeared in Fig. 4.3. This test failed as the phantom geometry could not be identified after the wavelet denoising process. Thus, it is concluded that when the SNR is very low, averaging would be a better denoising method, but it is of course more time consuming.

For thresholding, the threshold value  $\lambda$  was determined by the universal threshold term and yielded a value of  $\lambda = 2.454$ . The SURE method of thresholding was also tested for the two datasets and was less efficient in terms of SNR increase (see Table 6.2). Obtaining  $\lambda$  according to the universal threshold term is independent of the coefficients value and it only depends on the image dimensions. Thus, the same threshold value for all three coefficients matrices (that store the difference information in the horizontal, vertical and diagonal directions) could be applied. On the contrary, the SURE method was done to each matrix of wavelet coefficients separately, this makes the SURE method adaptive to the data and led to the expectation of more efficient denoising. However, the universal method provided better results. Fig. 6.5c presents the plot that is needed for obtaining the SURE threshold value for one of the

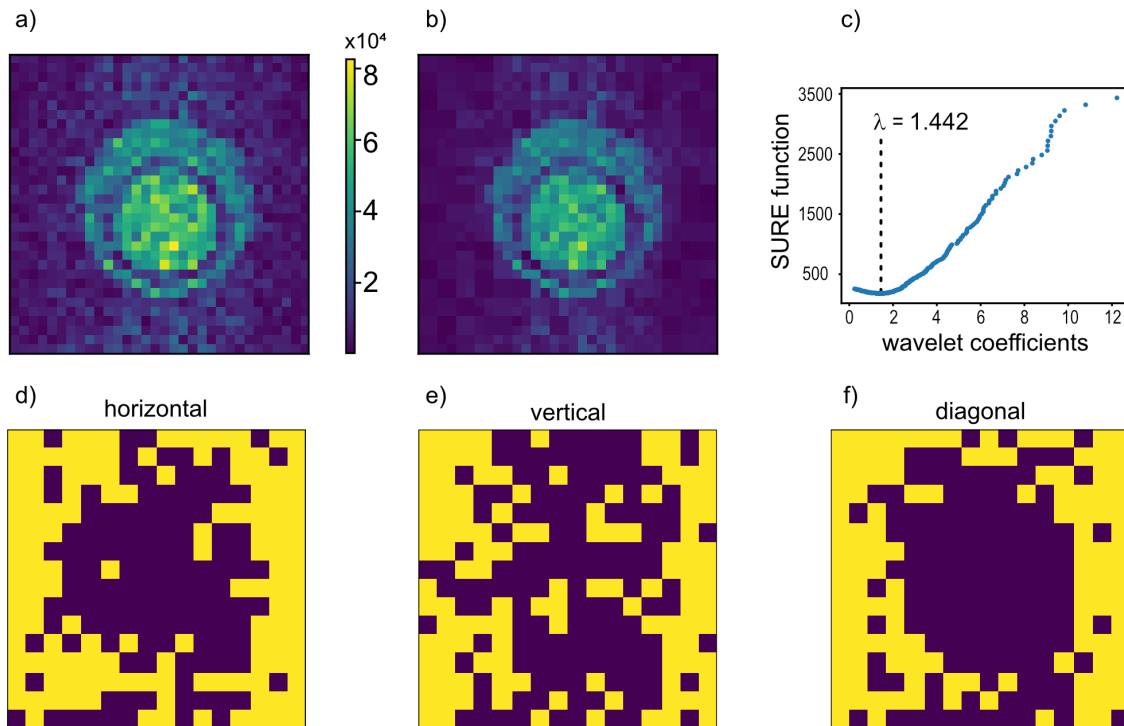


Figure 6.5: Single level wavelet denoising. a-b) Double phantom images before (a) and after (b) denoising. SNR values are provided in Table 6.2. c) Obtaining the SURE (Stein unbiased risk estimate) threshold for one of the wavelet coefficients matrices (of the horizontal direction). The same process is repeated to obtain the thresholds for the vertical and diagonal directions. d-f) Vanishing coefficients binary maps for each of the wavelet coefficients matrices, showing the scattering of the vanished (assigned to zero) coefficients (yellow) and of the coefficients with value greater than the threshold (purple).

Table 6.2: SNR comparison before and after wavelet denoising for two initial SNR levels and for two types of thresholds. Performed on double phantom images at an off-resonant saturation frequency. Wavelet denoising was applied using soft thresholding and the Haar wavelet function.

	Low initial SNR		High initial SNR	
	Before	After	Before	After
Universal threshold	6.82	9.79 (+44%)	10.15	15.88 (+56%)
SURE threshold	6.82	8.75 (+28%)	10.15	13.48 (+33%)

wavelet coefficients matrices (of the horizontal direction). It has the sorted coefficients value along the x-axis and their SURE function evaluations along the y-axis. The threshold is taken as the coefficient value at the minimum which is  $\lambda = 1.442$ . For the two other wavelet coefficients matrices the threshold values were  $\lambda = 1.426$ ,  $\lambda = 1.466$  for the vertical and diagonal directions, respectively. The higher value of the universal threshold resulted, in this case, with a more efficient denoising. Generally, however, increasing the threshold value only improves the denoising process up to a certain limit, further increasing  $\lambda$  beyond this limit would decrease the SNR or might lead to artefacts in the image [102]. This is the result of losing vital information when vanishing to many coefficients. Possible reason for the underperformance of SURE denoising is the image resolution of hyperpolarized xenon MRI. This resolution is relatively low ( $32 \times 32$  pixels) and yields a wavelet coefficients statistics of a somewhat low quality. Additionally, there are other reports with empirical data about the underperformance of SURE versus the universal threshold, e.g., [111].

The connection between the image noise level and the threshold value was investigated for the two thresholding methods by calculating the threshold for the datasets of low and higher SNR. The term for the universal threshold includes the SD of the noise in the image, therefore it is clear that a lower SNR image (higher SD) would have a higher threshold value. The SURE threshold was calculated and yielded roughly the same values for the two datasets of  $\lambda = 1.426$  and  $\lambda = 1.466$  for the low and high SNR images, respectively (these are maximal values out of the three thresholds obtained for each SNR regime). Thus, it seems that the SURE threshold, unlike the universal

threshold, is independent of the image noise level. However, to calculate the SURE threshold, the images had to be normalized to have a noise level of 1 and therefore a noisier image would probably have more vanishing coefficients for the same threshold value. Quantification of the number of vanished coefficients in each SNR regime will be done in the next paragraph and then a conclusion can be drawn.

Fig. 6.5 d-f show binary maps of vanishing coefficients for the wavelet coefficients matrices of the horizontal, vertical and diagonal directions. In yellow are the coefficients that were below the threshold value and were assigned to a value of zero (vanished). In purple are the coefficients that were above the threshold value and were not assigned to zero (rather "pulled down" in value toward zero according to the "soft" way of thresholding). The maps were plotted for the wavelet coefficients matrices of the image in Fig. 6.5a and the threshold value was set according to the universal threshold. The positions of the vanished coefficients correspond to areas in the image that are rich in noise. Vanishing of these wavelet coefficients is equivalent to averaging of their parent pixels, this is the wavelet way of achieving local averaging selectively (only where the coefficients vanish) and it is the denoising mechanism of the entire image. The proportions of vanished coefficients out of the total number of wavelet coefficients (which was  $16^2$  since the image resolution was  $32^2$  and one level decomposition was performed) in each of the maps shown in Fig. 6.5 d-f are 0.52, 0.47 and 0.48, respectively. The meaning of these proportion values is that about 50% of pixel pairs in each direction were averaged. Calculation of the same proportion values with the SURE threshold yielded 0.26, 0.25 and 0.18 for the low SNR image and 0.26, 0.22 and 0.29 for the higher SNR image. Coming back to the connection between the image noise level and the SURE threshold value, the calculated proportion values do not support the idea that a higher noise level leads to a higher number of vanishing coefficients. The proportions of the vanished coefficients are actually higher (when summed together) for the high SNR image.

In conclusion, the connection between the image noise level and the SURE threshold value is not as intuitive as one might expect and the two do not display direct proportionality. This direct proportionality, however, does hold between the universal threshold and the noise level.

Till this point only single level wavelet decomposition was performed. For multilevel denoising, the same procedure applied to a single level (decomposition and thresholding) was iteratively applied to a number of up to 5 levels (the image resolution was  $32^2$  which allows denoising of maximally 5 levels,  $32 = 2^5$ ). Fig. 6.6 a-b show the images before and after multilevel denoising with 3 levels (the choice for the number of levels is detailed in the next paragraph). For thresholding of each level, the universal threshold was used (with same value as for single level). Multilevel denoising provided 2.3-fold SNR increase relative to the original image. This denoising ability is meaningfully larger ( $> 50\%$ ) than the single level ability with the universal threshold. In the multilevel approach, additional noise can be removed by further decomposing the image (into coarser scales) and thresholding of more wavelet coefficients that correspond to noise [103].

The choice for the number of levels in multilevel denoising was done empirically by measuring the SNR in wavelet-denoised images which were decomposed using a different number of levels from 2 to 5. Fig. 6.6 c-d present the graphs of SNR vs. the number of levels for each of the universal and SURE thresholds. Whereas the universal threshold showed maximal SNR value with 3 levels, the SURE threshold showed maximal SNR with 4 levels. The optimal number of levels for each of the thresholds suggest that indeed more noise could be identified (and removed) in the additional levels beyond the single (first) level. However, using the maximal number of levels also didn't provide the optimal results since the highest (most coarse) levels are already "smooth" enough as a consequence of the image approximations that were made in the previous levels and they do not contain additional wavelet coefficients that correspond to noise [112]. Thresholding of coefficients in these coarse levels nevertheless only decreased the SNR. Multilevel denoising with the SURE threshold in 4 levels of the image in Fig. 6.6a resulted in a lower SNR increase (than with the universal threshold in 3 levels shown in Fig. 6.6b) of 1.5-fold (image not shown). Here, as in the single level, the adaptivity of the SURE threshold to the data led to the expectation of outperforming the universal threshold. However, this was not observed, presumably because of the aforementioned aspects for the single level denoising.

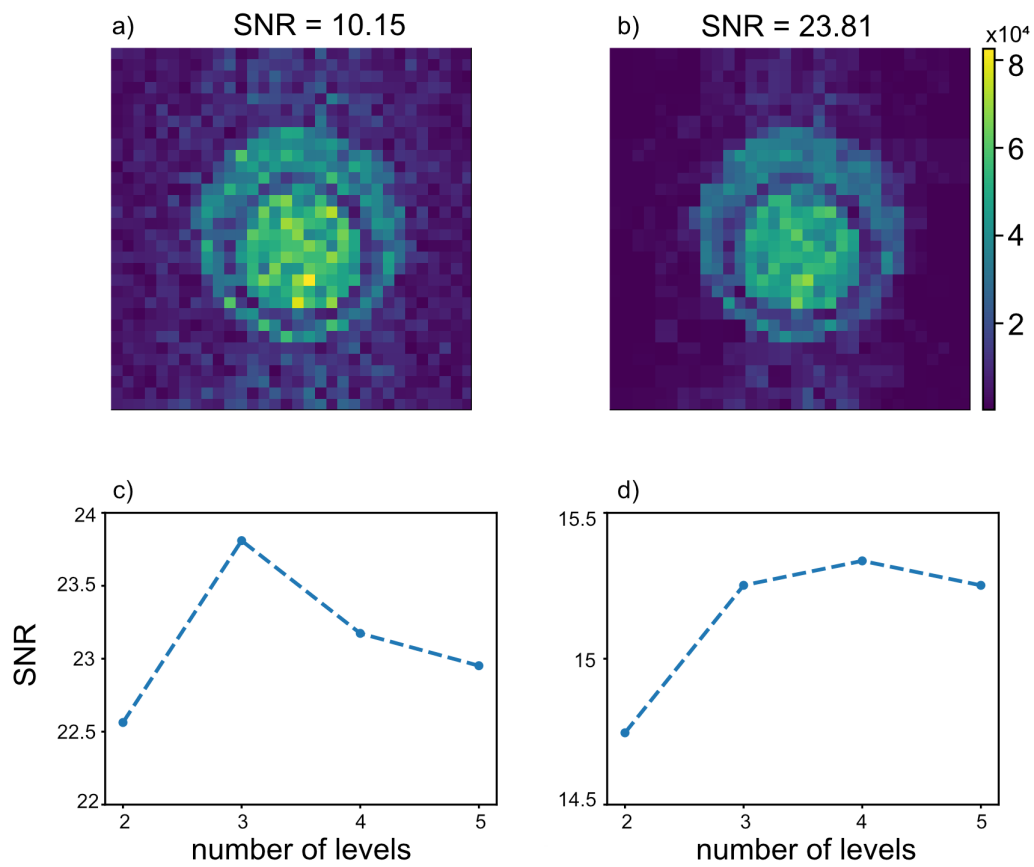


Figure 6.6: Multilevel wavelet denoising. a-b) Double phantom images before (a) and after (b) denoising of 3 levels using the universal threshold. c-d) Finding the optimal number of levels to denoise according to the criterion of maximal SNR when using the universal threshold (c) and the SURE threshold (d) in each level.

# Bibliography

- [1] F. Bloch. Nuclear induction. *Phys. Rev.*, 70:460–474, Oct 1946.
- [2] Claude Cohen-Tannoudji, Bernard Diu, and Franck Laloë. *Quantum mechanics; 1st ed.* Wiley, New York, NY, 1977. Trans. of : Mécanique quantique. Paris : Hermann, 1973.
- [3] W. Gerlach and O. Stern. Das magnetische moment des silberatoms. *Z. Physik*, 9:353–355, 1922.
- [4] M.H. Levitt. *Spin Dynamics: Basics of Nuclear Magnetic Resonance.* Wiley, 2001.
- [5] Thad G. Walker and William Happer. Spin-exchange optical pumping of noble-gas nuclei. *Rev. Mod. Phys.*, 69:629–642, Apr 1997.
- [6] Danila A. Barskiy, Aaron M. Coffey, Panayiotis Nikolaou, Dmitry M. Mikhaylov, Boyd M. Goodson, Rosa T. Branca, George J. Lu, Mikhail G. Shapiro, Ville-Veikko Telkki, Vladimir V. Zhivonitko, Igor V. Koptug, Oleg G. Salnikov, Kirill V. Kovtunov, Valerii I. Bukhtiyarov, Matthew S. Rosen, Michael J. Barlow, Shahideh Safavi, Ian P. Hall, Leif Schröder, and Eduard Y. Chekmenev. Cover picture: Nmr hyperpolarization techniques of gases (chem. eur. j. 4/2017). *Chemistry – A European Journal*, 23(4):722–722, 2017.
- [7] Leif Schröder, Thomas J. Lowery, Christian Hilty, David E. Wemmer, and Alexander Pines. Molecular imaging using a targeted magnetic resonance hyperpolarized biosensor. *Science*, 314(5798):446–449, 2006.

- [8] Harden M. McConnell. Reaction rates by nuclear magnetic resonance. *Journal of Chemical Physics*, 28:430–431, 1958.
- [9] Kunth Martin. *characterization and optimization of saturation transfer nmr with exchanging xenon in different host guest systems*. PhD thesis, Free University Berlin, Physics department, 2016.
- [10] Donald E. Woessner, Shanrong Zhang, Matthew E. Merritt, and A. Dean Sherry. Numerical solution of the bloch equations provides insights into the optimum design of paracest agents for mri. *Magnetic Resonance in Medicine*, 53(4):790–799, 2005.
- [11] Kenya Murase and Nobuyoshi Tanki. Numerical solutions to the time-dependent bloch equations revisited. *Magnetic Resonance Imaging*, 29(1):126–131, 2011.
- [12] Moritz Zaiss, Matthias Schnurr, and Peter Bachert. Analytical solution for the depolarization of hyperpolarized nuclei by chemical exchange saturation transfer between free and encapsulated xenon (hypercest). *The Journal of Chemical Physics*, 136(14):144106, 2012.
- [13] M. Kunth, C. Witte, and L. Schröder. Quantitative chemical exchange saturation transfer with hyperpolarized nuclei (qhyper-cest): Sensing xenon-host exchange dynamics and binding affinities by nmr. *The Journal of Chemical Physics*, 141(19):194202, 2014.
- [14] G. Varma, R. E. Lenkinski, and E. Vinogradov. Keyhole chemical exchange saturation transfer. *Magnetic Resonance in Medicine*, 68(4):1228–1233, 2012.
- [15] Xiaoping Hu and Todd Parrish. Reduction of field of view for dynamic imaging. *Magnetic Resonance in Medicine*, 31(6):691–694, 1994.
- [16] Michael Lustig, David Donoho, and John M. Pauly. Sparse mri: The application of compressed sensing for rapid mr imaging. *Magnetic Resonance in Medicine*, 58(6):1182–1195, 2007.

- [17] Frank R. Korosec, Richard Frayne, Thomas M. Grist, and Charles A. Mistretta. Time-resolved contrast-enhanced 3d mr angiography. *Magnetic Resonance in Medicine*, 36(3):345–351, 1996.
- [18] R. A. Jones, O. Haraldseth, T. B. Müller, P. A. Rinck, and A. N. Øksendal. K-space substitution: A novel dynamic imaging technique. *Magnetic Resonance in Medicine*, 29(6):830–834, 1993.
- [19] Klaas P. Pruessmann, Markus Weiger, Markus B. Scheidegger, and Peter Boesiger. Sense: Sensitivity encoding for fast mri. *Magnetic Resonance in Medicine*, 42(5):952–962, 1999.
- [20] Mark A. Griswold, Peter M. Jakob, Robin M. Heidemann, Mathias Nittka, Vladimir Jellus, Jianmin Wang, Berthold Kiefer, and Axel Haase. Generalized autocalibrating partially parallel acquisitions (grappa). *Magnetic Resonance in Medicine*, 47(6):1202–1210, 2002.
- [21] Manojkumar Saranathan, Dan W. Rettmann, Brian A. Hargreaves, Sharon E. Clarke, and Shreyas S. Vasanawala. Differential subsampling with cartesian ordering (disco): A high spatio-temporal resolution dixon imaging sequence for multiphasic contrast enhanced abdominal imaging. *Journal of Magnetic Resonance Imaging*, 35(6):1484–1492, 2012.
- [22] Richard Bitar, General Leung, Richard Perng, Sameh Tadros, Alan R. Moody, Josee Sarrazin, Caitlin McGregor, Monique Christakis, Sean Symons, Andrew Nelson, and Timothy P. Roberts. Mr pulse sequences: What every radiologist wants to know but is afraid to ask. *RadioGraphics*, 26(2):513–537, 2006. PMID: 16549614.
- [23] R. M. Henkelman, G. J. Stanisz, and S. J. Graham. Magnetization transfer in mri: a review. *NMR in Biomedicine*, 14(2):57–64, 2001.
- [24] K.M Ward, A.H Aletras, and R.S Balaban. A new class of contrast agents for mri based on proton chemical exchange dependent saturation transfer (cest). *Journal of Magnetic Resonance*, 143(1):79–87, 2000.

- [25] *Cardiovascular MR Manual*, chapter Image Space and k-Space. Springer International Publishing, 2015.
- [26] Mark J. Lowe and James A. Sorenson. Spatially filtering functional magnetic resonance imaging data. *Magnetic Resonance in Medicine*, 37(5):723–729, 1997.
- [27] Zhao, Mulkern, Tseng, Williamson, Patz, Kraft, Walsworth, Jolesz, and Albert. Gradient-echo imaging considerations for hyperpolarized  $^{129}\text{Xe}$  mr. *Journal of magnetic resonance. Series B*, 113 2:179–83, 1996.
- [28] Chang Min Hyun, Hwa Pyung Kim, Sung Min Lee, Sungchul Lee, and Jin Keun Seo. Deep learning for undersampled MRI reconstruction. *Physics in Medicine & Biology*, 63(13):135007, jun 2018.
- [29] Anagha Deshmane, Vikas Gulani, Mark A. Griswold, and Nicole Seiberlich. Parallel mr imaging. *Journal of Magnetic Resonance Imaging*, 36(1):55–72, 2012.
- [30] Jorge Chacon-Caldera, Adam Maunder, Madhwesha Rao, Graham Norquay, Oliver I. Rodgers, Matthew Clemence, Claudio Puddu, Lothar R. Schad, and Jim M. Wild. Dissolved hyperpolarized xenon-129 mri in human kidneys. *Magnetic Resonance in Medicine*, 83(1):262–270, 2020.
- [31] Matthew L. Zierhut, Yi-Fen Yen, Albert P. Chen, Robert Bok, Mark J. Albers, Vickie Zhang, Jim Tropp, Ilwoo Park, Daniel B. Vigneron, John Kurhanewicz, Ralph E. Hurd, and Sarah J. Nelson. Kinetic modeling of hyperpolarized  $^{13}\text{C}$ -pyruvate metabolism in normal rats and tramp mice. *Journal of Magnetic Resonance*, 202(1):85–92, 2010.
- [32] Shun Kishimoto, Jeffrey R Brender, Daniel R Crooks, Shingo Matsumoto, Tomohiro Seki, Nobu Oshima, Hellmut Merkle, Penghui Lin, Galen Reed, Albert P Chen, Jan Henrik Ardenkjaer-Larsen, Jeeva Munasinghe, Keita Saito, Kazutoshi Yamamoto, Peter L Choyke, James Mitchell, Andrew N Lane,

- Teresa WM Fan, W Marston Linehan, and Murali C Krishna. Imaging of glucose metabolism by  $^{13}\text{C}$ -mri distinguishes pancreatic cancer subtypes in mice. *eLife*, 8:e46312, aug 2019.
- [33] Sasan Partovi, Anja-Carina Schulte, Bjoern Jacobi, Markus Klarhöfer, Alan B. Lumsden, Matthias Loebe, Mark G. Davies, Georg P. Noon, Christof Karmolik, Lisa Zipp, Georg Bongartz, and Deniz Bilecen. Blood oxygenation level-dependent (bold) mri of human skeletal muscle at 1.5 and 3 t. *Journal of Magnetic Resonance Imaging*, 35(5):1227–1232, 2012.
- [34] R.D. Nowak. Wavelet-based rician noise removal for magnetic resonance imaging. *IEEE Transactions on Image Processing*, 8(10):1408–1419, 1999.
- [35] L. A. Shepp and B. F. Logan. The fourier reconstruction of a head section. *IEEE Transactions on Nuclear Science*, 21(3):21–43, 1974.
- [36] Schuenke Patrick. [github.com/schuenke/BMCTool](https://github.com/schuenke/BMCTool), 2021.
- [37] *Handbook of Fourier Analysis & Its Applications*, chapter Fourier Transforms in Probability, Random Variables and Stochastic Processes. Oxford Scholarship Online, 2020.
- [38] Peter J. Niedbalski, Matthew M. Willmering, Scott H. Robertson, Matthew S. Freeman, Wolfgang Loew, Randy O. Giaquinto, Christopher Ireland, Ronald G. Pratt, Charles L. Dumoulin, Jason C. Woods, and Zackary I. Cleveland. Mapping and correcting hyperpolarized magnetization decay with radial keyhole imaging. *Magnetic Resonance in Medicine*, 82(1):367–376, 2019.
- [39] Seong Dae Yun, Ralph Weidner, Peter H. Weiss, and N. Jon Shah. Evaluating the utility of epik in a finger tapping fmri experiment using bold detection and effective connectivity. *Scientific Reports*, 2019.
- [40] Dong Liu, Xiaoyan Sun, Feng Wu, Shipeng Li, and Ya-Qin Zhang. Image compression with edge-based inpainting. *IEEE Transactions on Circuits and Systems for Video Technology*, 17(10):1273–1287, 2007.

- [41] Nasir Ahmed. How i came up with the discrete cosine transform. *Digital Signal Processing*, 1(1):4–5, 1991.
- [42] Felicitas Pfeifer. Distribution, formation and regulation of gas vesicles. *Nature reviews. Microbiology*, 10(10):705—715, October 2012.
- [43] A E Walsby. Gas vesicles. *Microbiological Reviews*, 58(1):94–144, 1994.
- [44] Arash Farhadi, Gabrielle Ho, Martin Kunth, Bill Ling, Anupama Lakshmanan, George J Lu, Raymond W. Bourdeau, Leif Schröder, and Mikhail G. Shapiro. Recombinantly expressed gas vesicles as nanoscale contrast agents for ultrasound and hyperpolarized mri. *AIChE Journal*, 64(8):2927–2933, 2018.
- [45] Martin Kunth, George J. Lu, Christopher Witte, Mikhail G. Shapiro, and Leif Schröder. Protein nanostructures produce self-adjusting hyperpolarized magnetic resonance imaging contrast through physical gas partitioning. *ACS Nano*, 12(11):10939–10948, 2018. PMID: 30204404.
- [46] George Lu, Arash Farhadi, Jerzy Szablowski, Audrey Lee-Gosselin, Samuel Barnes, Anupama Lakshmanan, Raymond Bourdeau, and Mikhail Shapiro. Acoustically modulated magnetic resonance imaging of gas-filled protein nanostructures. *Nature Materials*, 17, 05 2018.
- [47] Matthias Schnurr, Karl Sydow, Honor May Rose, Margitta Dathe, and Leif Schröder. Brain endothelial cell targeting via a peptide-functionalized liposomal carrier for xenon hyper-cest mri. *Advanced Healthcare Materials*, 4(1):40–45, 2015.
- [48] Martin Kunth and Leif Schröder. Binding site exchange kinetics revealed through efficient spin–spin dephasing of hyperpolarized  $^{129}\text{Xe}$ . *Chem. Sci.*, 12:158–169, 2021.
- [49] HáKon Gudbjartsson and Samuel Patz. The rician distribution of noisy mri data. *Magnetic Resonance in Medicine*, 34(6):910–914, 1995.

- [50] Martin Kunth, Christopher Witte, Andreas Hennig, and Leif Schröder. Identification, classification, and signal amplification capabilities of high-turnover gas binding hosts in ultra-sensitive nmr. *Chem. Sci.*, 6:6069–6075, 2015.
- [51] Matthias Schnurr, Roymon Joseph, Alissa Naugolny-Keisar, Dana Kaizerman-Kane, Nils Bogdanoff, Patrick Schuenke, Yoram Cohen, and Leif Schröder. High exchange rate complexes of 129xe with water-soluble pillar[5]arenes for adjustable magnetization transfer mri. *ChemPhysChem*, 20(2):246–251, 2019.
- [52] Shu-Yuan Yeh and Richard E. Peterson. Solubility of carbon dioxide, krypton, and xenon in aqueous solution. *Journal of Pharmaceutical Sciences*, 53(7):822–824, 1964.
- [53] Werner Nau and Jyotirmayee Mohanty. Taming fluorescent dyes with cucurbituril. *International Journal of Photoenergy*, 7, 01 2005.
- [54] Debapratim Das, Khaleel I. Assaf, and Werner M. Nau. Applications of cucurbiturils in medicinal chemistry and chemical biology. *Frontiers in Chemistry*, 7:619, 2019.
- [55] Frank Biedermann and Werner M. Nau. Noncovalent chirality sensing ensembles for the detection and reaction monitoring of amino acids, peptides, proteins, and aromatic drugs. *Angewandte Chemie International Edition*, 53(22):5694–5699, 2014.
- [56] Mara Florea and Werner M. Nau. Strong binding of hydrocarbons to cucurbituril probed by fluorescent dye displacement: A supramolecular gas-sensing ensemble. *Angewandte Chemie International Edition*, 50(40):9338–9342, 2011.
- [57] María del Pozo, Elías Blanco, Enrique Fatás, Pedro Hernández, and Carmen Quintana. New supramolecular interactions for electrochemical sensors development: different cucurbit[8]uril sensing platform designs. *Analyst*, 137:4302–4308, 2012.

- [58] Khaleel I. Assaf and Werner M. Nau. Cucurbiturils: from synthesis to high-affinity binding and catalysis. *Chem. Soc. Rev.*, 44:394–418, 2015.
- [59] Clancy Carlton Slack. *Be Our Guest: 129Xe Detection in Macrocycles and Oriented Environments*. PhD thesis, UNIVERSITY OF CALIFORNIA, BERKELEY, Chemistry department, 2016.
- [60] César Márquez, Robert R. Hudgins, and Werner M. Nau. Mechanism of host-guest complexation by cucurbituril. *Journal of the American Chemical Society*, 126(18):5806–5816, 2004. PMID: 15125673.
- [61] Matthias Schnurr, Jagoda Sloniec-Myszk, Jörg Döpfert, Leif Schröder, and Andreas Hennig. Supramolecular assays for mapping enzyme activity by displacement-triggered change in hyperpolarized 129xe magnetization transfer nmr spectroscopy. *Angewandte Chemie International Edition*, 54(45):13444–13447, 2015.
- [62] Andreas Hennig, Hüseyin Bakirci, and Werner M. Nau. Label-free continuous enzyme assays with macrocycle-fluorescent dye complexes. *Nature Methods*, 4:629–632, 2007.
- [63] Mikhail V. Rekharsky, Young Ho Ko, N. Selvapalam, Kimoon Kim, and Yoshihisa Inoue. Complexation thermodynamics of cucurbit[6]uril with aliphatic alcohols, amines, and diamines. *Supramolecular Chemistry*, 19(1-2):39–46, 2007.
- [64] Francis Hane, Tao Li, Peter Smylie, Raiili Pellizzari, Jennifer Plata, Brenton Deboef, and Mercy Albert. In vivo detection of cucurbit[6]uril, a hyperpolarized xenon contrast agent for a xenon magnetic resonance imaging biosensor. *Scientific Reports*, 7:41027, 01 2017.
- [65] Werner M. Nau, Garima Ghale, Andreas Hennig, Hüseyin Bakirci, and David M. Bailey. Substrate-selective supramolecular tandem assays: Monitoring enzyme inhibition of arginase and diamine oxidase by fluorescent dye displacement from calixarene and cucurbituril macrocycles. *Journal of the American Chemical Society*, 131(32):11558–11570, 2009. PMID: 19627092.

- [66] Jyotirmayee Mohanty and Werner M. Nau. Ultrastable rhodamine with cucurbituril. *Angewandte Chemie International Edition*, 44(24):3750–3754, 2005.
- [67] Hongyuan Zhang, Lele Liu, Chao Gao, Ruyi Sun, and Qiaochun Wang. Enhancing photostability of cyanine dye by cucurbituril encapsulation. *Dyes and Pigments*, 94(2):266–270, 2012.
- [68] Sharmistha Dutta Choudhury, Jyotirmayee Mohanty, Hari P. Upadhyaya, Achikanath C. Bhasikuttan, and Haridas Pal. Photophysical studies on the noncovalent interaction of thioflavin t with cucurbit[n]uril macrocycles. *The Journal of Physical Chemistry B*, 113(7):1891–1898, 2009. PMID: 19175303.
- [69] Suma S. Thomas, Hao Tang, and Cornelia Bohne. Noninnocent role of na<sup>+</sup> ions in the binding of the n-phenyl-2-naphthylammonium cation as a ditopic guest with cucurbit[7]uril. *Journal of the American Chemical Society*, 141(24):9645–9654, 2019. PMID: 31131599.
- [70] Winston Ong and Angel E. Kaifer. Salt effects on the apparent stability of the cucurbit[7]uril-methyl viologen inclusion complex. *The Journal of Organic Chemistry*, 69(4):1383–1385, 2004. PMID: 14961699.
- [71] Xinhao Shi, Wei Gu, Cuiling Zhang, Longyun Zhao, Li Li, Weidong Peng, and Yuezhong Xian. Construction of a graphene/au-nanoparticles/cucurbit[7]uril-based sensor for pb<sup>2+</sup> sensing. *Chemistry – A European Journal*, 22(16):5643–5648, 2016.
- [72] Ronit Shusterman-Krush, Laura Grimm, Liat Avram, Frank Biedermann, and Amnon Bar-Shir. Elucidating dissociation activation energies in host–guest assemblies featuring fast exchange dynamics. *Chem. Sci.*, 12:865–871, 2021.
- [73] Hao Tang, Denis Fuentealba, Young Ho Ko, Narayanan Selvapalam, Kimoon Kim, and Cornelia Bohne. Guest binding dynamics with cucurbit[7]uril in the presence of cations. *Journal of the American Chemical Society*, 133(50):20623–20633, 2011. PMID: 22073977.

- [74] Zsombor Miskolczy, Mónika Megyesi, László Biczók, Amrutha Prabodh, and Frank Biedermann. Kinetics and mechanism of cation-induced guest release from cucurbit[7]uril. *Chemistry – A European Journal*, 26(33):7433–7441, 2020.
- [75] Hans-Jürgen Buschmann, Ernst Cleve, Klaus Jansen, Andreas Wego, and Eckhard Schollmeyer. The determination of complex stabilities between different cyclodextrins and dibenzo-18-crown-6, cucurbit[6]uril, decamethylcucurbit[5]uril, cucurbit[5]uril, p-tert-butylcalix[4]arene and p-tert-butylcalix[6]arene in aqueous solutions using a spectrophotometric method. *Materials Science and Engineering: C*, 14(1):35–39, 2001.
- [76] Jabadurai Jayapaul and Leif Schröder. Molecular sensing with host systems for hyperpolarized  $^{129}\text{Xe}$ . *Molecules*, 25(20), 2020.
- [77] Martin Kunth, Christopher Witte, and Leif Schröder. Mapping of absolute host concentration and exchange kinetics of xenon hyper-contrast mri agents. *Pharmaceuticals*, 14(2), 2021.
- [78] Ashley E. Truxal, Liping Cao, Lyle Isaacs, David E. Wemmer, and Alexander Pines. Directly functionalized cucurbit[7]uril as a biosensor for the selective detection of protein interactions by  $^{129}\text{Xe}$  hypercontrast nmr. *Chemistry - A European Journal*, 25(24):6108–6112, 2019.
- [79] Gaspard Huber, François-Xavier Legrand, Véronique Lewin, Delphine Baumann, Marie-Pierre Heck, and Patrick Berthault. Interaction of xenon with cucurbit[5]uril in water. *ChemPhysChem*, 12(6):1053–1055, 2011.
- [80] Jörg Döpfert, Christopher Witte, and Leif Schröder. Fast gradient-encoded contrast spectroscopy of hyperpolarized xenon. *ChemPhysChem*, 15(2):261–264, 2014.
- [81] Jean-Nicolas Dumez. Spatial encoding and spatial selection methods in high-resolution nmr spectroscopy. *Progress in Nuclear Magnetic Resonance Spectroscopy*, 109:101–134, 2018.

- [82] Xiang Xu, Jae-Seung Lee, and Alexej Jerschow. Ultrafast scanning of exchangeable sites by nmr spectroscopy. *Angewandte Chemie International Edition*, 52(32):8281–8284, 2013.
- [83] Jörg Döpfert, Christopher Witte, and Leif Schröder. Slice-selective gradient-encoded cest spectroscopy for monitoring dynamic parameters and high-throughput sample characterization. *Journal of Magnetic Resonance*, 237:34–39, 2013.
- [84] Jörg Döpfert, Moritz Zaiss, Christopher Witte, and Leif Schröder. Ultrafast cest imaging. *Journal of magnetic resonance (San Diego, Calif. : 1997)*, 243:47–53, June 2014.
- [85] Céline Boutin, Estelle Léonce, Thierry Brotin, Alexej Jerschow, and Patrick Berthault. Ultrafast z-spectroscopy for <sup>129</sup>Xe nmr-based sensors. *The Journal of Physical Chemistry Letters*, 4(23):4172–4176, 2013.
- [86] Anupama Lakshmanan, George J Lu, Arash Farhadi, Suchita P Nety, Martin Kunth, Audrey Lee-Gosselin, David Maresca, Raymond W Bourdeau, Melissa Yin, Judy Yan, Christopher Witte, Dina Malounda, F Stuart Foster, Leif Schröder, and Mikhail G Shapiro. Preparation of biogenic gas vesicle nanostructures for use as contrast agents for ultrasound and mri. *Nature protocols*, 12(10):2050—2080, October 2017.
- [87] Mengxiao Liu, Yaewon Kim, and Christian Hilty. Characterization of chemical exchange using relaxation dispersion of hyperpolarized nuclear spins. *Analytical Chemistry*, 89(17):9154–9158, 2017. PMID: 28714674.
- [88] C. Witte, M. Kunth, F. Rossella, and L. Schröder. Observing and preventing rubidium runaway in a direct-infusion xenon-spin hyperpolarizer optimized for high-resolution hyper-cest (chemical exchange saturation transfer using hyperpolarized nuclei) nmr. *The Journal of Chemical Physics*, 140(8):084203, 2014.
- [89] E. R. McVeigh, R. M. Henkelman, and M. J. Bronskill. Noise and filtration in magnetic resonance imaging. *Medical Physics*, 12(5):586–591, 1985.

- [90] Ching-Nien Chen and D I. Hoult. *Biomedical Magnetic Resonance Technology*. Bristol: Institute of Physics Pub, 1995., 1995.
- [91] Sven Junge. *Cryogenic and Superconducting Coils for MRI Corrections were made to this article on 31st May 2012*. American Cancer Society, 2012.
- [92] Linwei Fan, Fan Zhang, Hui Fan, and Caiming Zhang. Brief review of image denoising techniques. *Visual Computing for Industry, Biomedicine, and Art*, 2(1), 07 2019.
- [93] Roger A. Horn and Charles R. Johnson. *Matrix Analysis*. Cambridge University Press, 1990.
- [94] I.T. Jolliffe. *Principal Component Analysis*. Springer Verlag, 1986.
- [95] J.N. Franklin. *Matrix Theory*. Dover Books on Mathematics. Dover Publications, 2012.
- [96] Alfred Haar. Zur theorie der orthogonalen funktionensysteme. *Mathematische Annalen*, 69:331–371, 1910.
- [97] Stphane Mallat. *A Wavelet Tour of Signal Processing, Third Edition: The Sparse Way*. Academic Press, Inc., USA, 3rd edition, 2008.
- [98] David Taubman and Michael Marcellin. *JPEG2000 Image Compression Fundamentals, Standards and Practice*. Springer Publishing Company, Incorporated, 2013.
- [99] Michael Lustig, David Donoho, and John M. Pauly. Sparse mri: The application of compressed sensing for rapid mr imaging. *Magnetic Resonance in Medicine*, 58(6):1182–1195, 2007.
- [100] David L Donoho and Iain M Johnstone. Ideal spatial adaptation by wavelet shrinkage. *Biometrika*, 81(3):425–455, 09 1994.

- [101] David L. Donoho and Iain M. Johnstone. Adapting to unknown smoothness via wavelet shrinkage. *Journal of the American Statistical Association*, 90(432):1200–1224, 1995.
- [102] Raghuram Rangarajan, Ramji Venkataramanan, and Siddharth Shah. Image denoising using wavelets. *wavelets & time frequency.*, 2002.
- [103] ASHISH KHARE and UMA SHANKER TIWARY. Soft-thresholding for denoising of medical images — a multiresolution approach. *International Journal of Wavelets, Multiresolution and Information Processing*, 03(04):477–496, 2005.
- [104] Charles M. Stein. Estimation of the Mean of a Multivariate Normal Distribution. *The Annals of Statistics*, 9(6):1135 – 1151, 1981.
- [105] Lee et al. Pywavelets: A python package for wavelet analysis. *Journal of Open Source Software*, 4(36):1237, 2019.
- [106] Jörg Döpfert, Christopher Witte, Martin Kunth, and Leif Schröder. Sensitivity enhancement of (hyper-)cestr image series by exploiting redundancies in the spectral domain. *Contrast Media & Molecular Imaging*, 9(1):100–107, 2014.
- [107] Mark D. Does, Jonas Lynge Olesen, Kevin D. Harkins, Teresa Serradas-Duarte, Daniel F. Gochberg, Sune N. Jespersen, and Noam Shemesh. Evaluation of principal component analysis image denoising on multi-exponential mri relaxometry. *Magnetic Resonance in Medicine*, 81(6):3503–3514, 2019.
- [108] Raymond B. Cattell. The scree test for the number of factors. *Multivariate Behavioral Research*, 1(2):245–276, 1966. PMID: 26828106.
- [109] R Mortezaejad and A Gholami. Optimization of wavelet- and curvelet-based denoising algorithms by multivariate SURE and GCV. *Journal of Geophysics and Engineering*, 13(3):378–390, 05 2016.
- [110] Xiaofeng Yang and Baowei Fei. A wavelet multiscale denoising algorithm for magnetic resonance (MR) images. *Measurement Science and Technology*, 22(2):025803, jan 2011.

- [111] Angkoon Phinyomark, Chusak Limsakul, and Pornchai Phukpattaranont. A comparative study of wavelet denoising for multifunction myoelectric control. In *2009 International Conference on Computer and Automation Engineering*, pages 21–25, 2009.
- [112] Yansun Xu, J.B. Weaver, D.M. Healy, and Jian Lu. Wavelet transform domain filters: a spatially selective noise filtration technique. *IEEE Transactions on Image Processing*, 3(6):747–758, 1994.

# Declaration

## Declaration of authorship

Name: Morik

First name: Hen-Amit

I declare to the Freie Universität Berlin that I have completed the submitted dissertation independently and without the use of sources and aids other than those indicated. The present thesis is free of plagiarism. I have marked as such all statements that are taken literally or in content from other writings. This dissertation has not been submitted in the same or similar form in any previous doctoral procedure. I agree to have my thesis examined by a plagiarism examination software.

Date: \_\_\_\_\_ Signature: \_\_\_\_\_

# Publications

## Papers under revision

1. Hen-Amit Morik, Patrick Schuenkea and Leif Schröder. Accelerated CEST Spectroscopy of Competitive Host-Guest Interactions using Spatial Parallelization with a Combined Approach of Variable Flip Angle, Keyhole and Averaging (CAVKA). *Physical Chemistry Chemical Physics (PCCP)* - under revision (2022).

## Conference contributions

1. Hen-Amit Morik and Leif Schröder. Keyhole imaging with hyperpolarized  $^{129}\text{Xe}$ . Minerva-Gentner Simposia, 18-19.02.2019, Weizmann Institute, Israel. Poster presentation and a flesh talk presentation.
2. Hen-Amit Morik, Patrik Schuenke and Leif Schröder. Combining the keyhole approach with variable flip angle excitation for MRI of hyperpolarized nuclei. ENC, 8-12.04.2019, Asilomar, California, USA. Poster presentation.
3. Hen-Amit Morik, Patrik Schuenke and Leif Schröder. Combined approach of variable flip angle, keyhole and averaging (CAVKA) for accelerating the acquisition of a low SNR imaging series. ISMRM, 8-12.08.2020, virtual conference. Video presentation.